Live imaging of autoimmune responses in distinct milieus of the central nervous system

Dissertation
for the award of the degree
"Doctor rerum naturalium"
Division of Mathematics and Natural Sciences
of the Georg-August-Universität Göttingen

in the doctoral programme „Molecular Physiology of the Brain“ (GGNB5)
of the Georg-August University School of Science (GAUSS)

submitted by

Corinna Schlosser

from Fulda

Göttingen, 2013

Members of the Thesis Committee

- Prof. Dr. Wolfgang Brück, Institute for Neuropathology, University Medical Centre Göttingen
- Dr. Till Marquardt, Developmental Neurobiology Laboratory, European Neuroscience Institute, Göttingen (ENI-G)
- Prof. Dr. Fred S. Wouters, Department of Neuro- and Sensory Physiology, Centre II Physiology and Pathophysiology, University Medical Centre, Göttingen
- Prof. Dr. Alexander Flügel, Department of Neuroimmunology, Institute for Multiple Sclerosis Research, University Medical Centre, Göttingen

Members of the Examination Board

Reviewer:	Prof. Dr. Wolfgang Brück, Institute for Neuropathology, University Medical Centre Göttingen
Second reviewer:	Dr. Till Marquardt, Developmental Neurobiology Laboratory, European Neuroscience Institute, Göttingen (ENI-G)
Third reviewer:	Prof. Dr. Fred S. Wouters, Department of Neuro- and Sensory Physiology, Centre II Physiology and Pathophysiology, University Medical Centre, Göttingen

Additional members of the Examination Board:

- Prof. Dr. Alexander Flügel, Department of Neuroimmunology, Institute for Multiple Sclerosis Research, University Medical Centre, Göttingen
- Prof. Dr. Mikael Simons, Cellular Neuroscience, Max Planck Institute for Experimental Medicine and Department of Neurology, University Medical Centre, Göttingen
- Prof. Dr. Hannelore Ehrenreich, Department of Clinical Neuroscience, Max Planck Institute for Experimental Medicine, Göttingen

Date of oral examination:

Table of contents

Abbreviations

aEAE	Active experimental autoimmune encephalomyelitis
APC	Antigen presenting cell
BALT	Bronchus-associated lymphoid tissue
BBB	Blood-brain barrier
βSyn	β-synuclein$_{93-111}$ peptide
BWL	Body weight loss
CCL5	Chemokine (C-C motif) ligand 5 (also: Regulated on activation, normal T cell expressed and secreted, RANTES)
CCL19	Chemokine (C-C motif) ligand 19
CCL20	Chemokine (C-C motif) ligand 20
CCR5	Chemokine (C-C motif) receptor 5
CCR6	Chemokine (C-C motif) receptor 6
CCR7	Chemokine (C-C motif) receptor 7
CFA	Complete Freund's adjuvant
CNS	Central nervous system
ConA	Concanavalin A
CXCL9	Chemokine (C-X-C motif) ligand 9
CXCL10	Chemokine (C-X-C motif) ligand 10
CXCL11	Chemokine (C-X-C motif) ligand 11
CXCL12	Chemokine (C-X-C motif) ligand 12
CXCR3	Chemokine (C-X-C motif) receptor 3

CXCR4	Chemokine (C-X-C motif) receptor 4
DMSO	Dimethyl sulfoxide
DNA	Deoxyribonucleic acid
EDTA	Ethylenediaminetetraacetic acid
FACS	Fluorescence-activated cell sorting
FBS	Foetal bovine serum
GFP	Green fluorescent protein
GM	Grey matter
HLA	Human leukocyte antigen
iCa^{2+}	Intracellular Calcium ion
ICAM-1	Intracellular adhesion molecule 1 (also: Cluster of differentiation 54, CD54)
I_{CRAC}	Calcium release-activated calcium ion channel
IFN-γ	Interferon γ
IL-17	Interleukin 17
IL-2R	Interleukin 2 receptor
i.p.	Intraperitoneal
IP3	inositol 1,4,5-trisphosphate
i.v.	Intravenous
LFA-1	Lymphocyte function-associated antigen 1
MAG	Myelin-associated glycoprotein
MBP	Myelin basic protein
MESV	Murine embryonic stem cell virus
MHC	Major histocompatibility complex

MOG	Myelin oligodendrocyte glycoprotein
MRI	Magnetic resonance imaging
MS	Multiple sclerosis
NFAT	Nuclear factor of T cell activation
NS	Nervous system
OVA	Ovalbumin
OX40	Tumor necrosis factor receptor superfamily, member 4 (also: Cluster of differentiation 134, CD134)
PBMC	Peripheral blood mononuclear cells
PCR	Polymerase chain reaction
PFA	Paraformaldehyde
PLC-γ	Phospholipase C-γ
PLP	Proteolipid protein
PP MS	Primary progressive MS
p.t.	Post transfer
ptEAE	Passive-transfer experimental autoimmune encephalomyelitis
QRT-PCR	Quantitative real-time PCR
RM	Re-stimulation medium
RNA	Ribonucleic acid
RR MS	Relapsing-remitting MS
RS	Rat serum
SC	Spinal cord
SP MS	Secondary progressive MS

TAG-1	Transient axonal glycoprotein 1
TCGM	T cell growth medium
TCM	T cell medium
TCR	T cell receptor
TNF-α	Tumor necrosis factor α
2P-LSM	Two-photon laser scanning microscopy
VCAM-1	Vascular cell adhesion molecule-1
VLA-4	Very late antigen-4 (also: Integrin alpha4beta1)
WM	White matter
YFP	Yellow fluorescent protein

Abstract

Multiple sclerosis (MS) is the most common inflammatory disease of the central nervous system (CNS). Even though it is considered to be a classical demyelinating disease, an increasing body of evidence also demonstrates the early presence of inflammatory lesions in the grey matter. In experimental autoimmune encephalomyelitis (EAE), the animal paradigm of MS, preferential involvement of grey matter is rarely reported, hindering the study of this important aspect of the disease.

In this thesis, green fluorescent protein (GFP)-transduced effector T cells reactive either against a myelin antigen, i.e. the myelin basic protein ($T_{MBP\text{-}GFP}$) or against a neuronal antigen, i.e. the β-synuclein ($T_{\beta\text{-}Syn\text{-}GFP}$) were used to induce EAE by passive transfer in recipient Lewis rats. The aim was to elucidate the homing behaviour of encephalitogenic effector T cells into the distinct milieus of the CNS. Both of these T cell lines had a similar phenotype *in vitro* and similar pathogenic potential *in vivo*. However, they displayed a completely different infiltration pattern in the CNS tissue: whereas the $T_{MBP\text{-}GFP}$ cells were distributed mainly in the white matter, the $T_{\beta\text{-}Syn\text{-}GFP}$ cells were mostly located in the grey matter of the brain and spinal cord (SC), mimicking the cortical pathology of MS. This divergent infiltration pattern was not due to tissue-intrinsic properties such as apoptosis rate or chemokine expression in the different CNS compartments. Neither did cell-specific properties such as chemokine/integrin expression profile, cytokine level or T cell homing during the preclinical phase play any role. By using two–photon laser scanning microscopy it was possible to visualize in real time the entry and the distribution of $T_{MBP\text{-}GFP}$ cells and $T_{\beta\text{-}Syn\text{-}GFP}$ cells in the meningeal compartments of brain and SC, thus providing indirect evidence that the antigen availability in the target tissue determines the level of activation and therefore the pattern of tissue invasion. Finally, direct activation of T_{MBP} cells in the white matter and of $T_{\beta\text{-}Syn}$ cells in the grey matter of the CNS parenchyma was demonstrated *in situ* by using a genetically encoded NFAT (nuclear factor of T cell activation) biosensor further confirming that the antigen-dependent activation of encephalitogenic T cells is the key factor that determines the homing of these cells into the target tissue.

1. Introduction

1.1 The central nervous system: an immune privileged organ?

For a long time the central nervous system (CNS) was thought to be an immune privileged tissue due to its molecular and cellular protection by the blood-brain barrier (BBB), the lack of lymphatic vessels and classical antigen presenting cells (APCs) within the tissue and a limited expression of constitutive MHC I and II molecules on CNS parenchymal cells (Engelhardt and Ransohoff, 2005). Today it is known that under physiological conditions the CNS is under immune surveillance. Beside resident microglia within the CNS parenchyma, peripheral immune cells assess the milieu in specialized compartments of brain and spinal cord (SC) outside the parenchyma (Ousman and Kubes, 2012). Moreover it is known that there is an immune cell subset that is able to express and carry specific molecular keys in response to pathological conditions, like multiple sclerosis (chapter 1.2) or its model experimental autoimmune encephalomyelitis (chapter 1.3), which enables specialized leukocytes to overcome the BBB and to infiltrate massively into the CNS (Engelhardt and Ransohoff, 2005).

1.1.1 Meninges and the blood-CNS barriers

The mammalian CNS is covered by three connective tissue membranes, named the meninges. Under the outermost meningeal layer, the dura mater, the adherent arachnoidea forms trabeculae which reach through the subarachnoidal space to the pia mater, the deepest layer of the meninges, which is adherent to the parenchymal basal membrane (fig. 1.1). Furthermore, the basement membrane and astrocytic end feet, together form the glia limitans, another border to the brain parenchyma (Ransohoff and Engelhardt, 2012). The arachnoid mater and the pia mater together are called leptomeninges. The leptomeninges contain the subarachnoidal space filled with the cerebrospinal fluid (CSF) and blood vessels that are build up by highly specialized endothelial cells, which are stably interconnected by tight junctions (fig. 1.1 and 1.2) (Engelhardt and Ransohoff, 2012). The pia mater encloses pre- and post-capillary venules reaching down deeper into the brain parenchyma (fig. 1.1). Here, the parenchyma is segregated from the brain by the glia limitans establishing the deeper perivascular space, which is called Virchow-Robin space (fig. 1.1 and 1.2) (Gerhardt and Betsholtz, 2003; Bechmann et al., 2007; Engelhardt and Ransohoff, 2012).

As described above, the CNS is structurally separated from peripheral milieu by a diffusion barrier formed by tightly connected endothelial cells and the glia limitans, which together build up the BBB. Another protective barrier of the CNS, the blood-cerebrospinal fluid barrier (BCSFB), established by choroid plexus epithelial cells, is localized in the ventricular system of the brain. Here, tight junctions between these epithelial cells form a diffusion barrier (Engelhardt and Ransohoff, 2012). Together those barriers maintain a stable environment and homeostasis for the neurons and only selective transporters and ion channels mediate a blood-brain concentration gradient and supply CNS cells with required metabolites (Pardridge, 2003). Besides inhibiting uncontrolled trans-cellular molecular diffusion, the BBB establishes an interface between the CNS and the immune system.

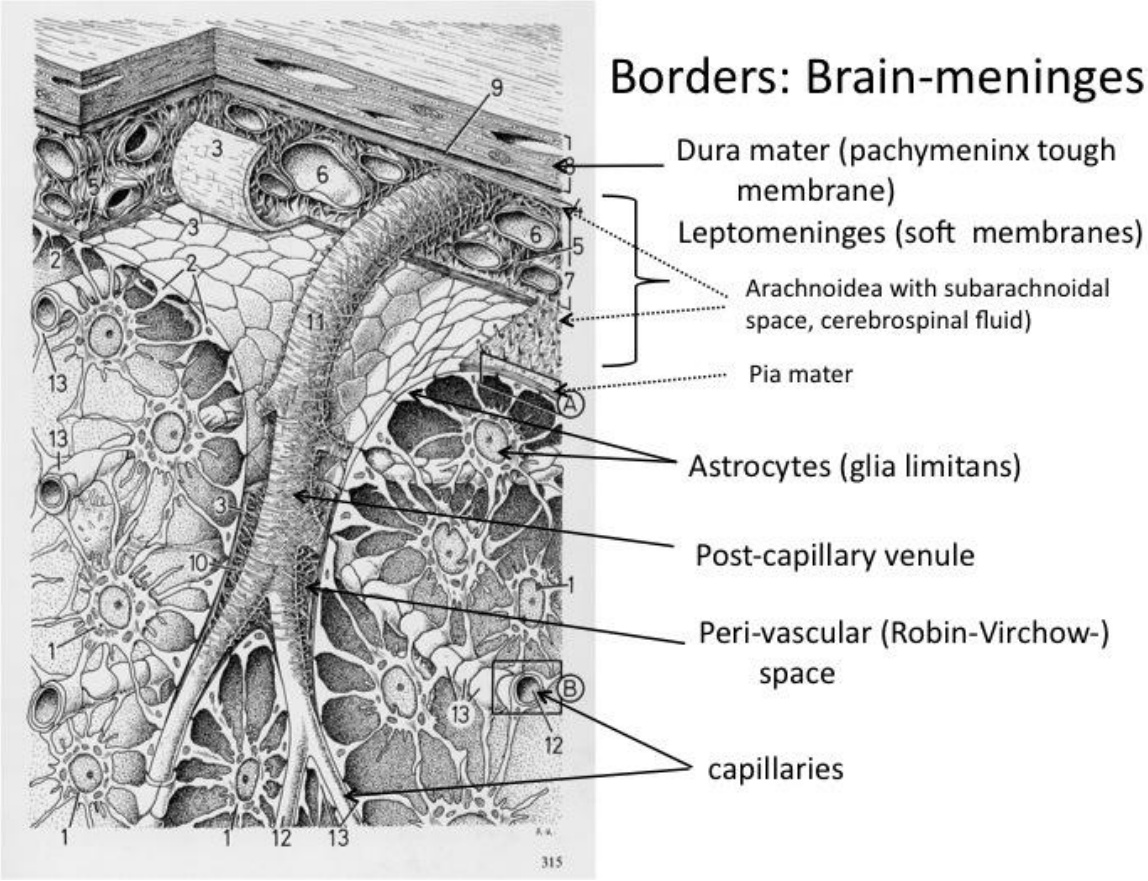

Figure 1.1 Schematic representation of the different anatomical levels from the meniges to brain or SC parenchyma. Under the dura mater and the arachnoidea, superficial leptomeningeal blood vessels lying on the surface of the brain and SC are directly surrounded by the CSF-filled subarachnoidal space. In contrast to deeper vessels, these vessels are not enveloped directly by the astrocytic end feet. Underneath, the subarachnoidal space is sealed by the pia mater and the glia limitans. Post-capillary venules and capillaries reach down into the brain parenchyma. Adapted from (Owens et al., 2008).

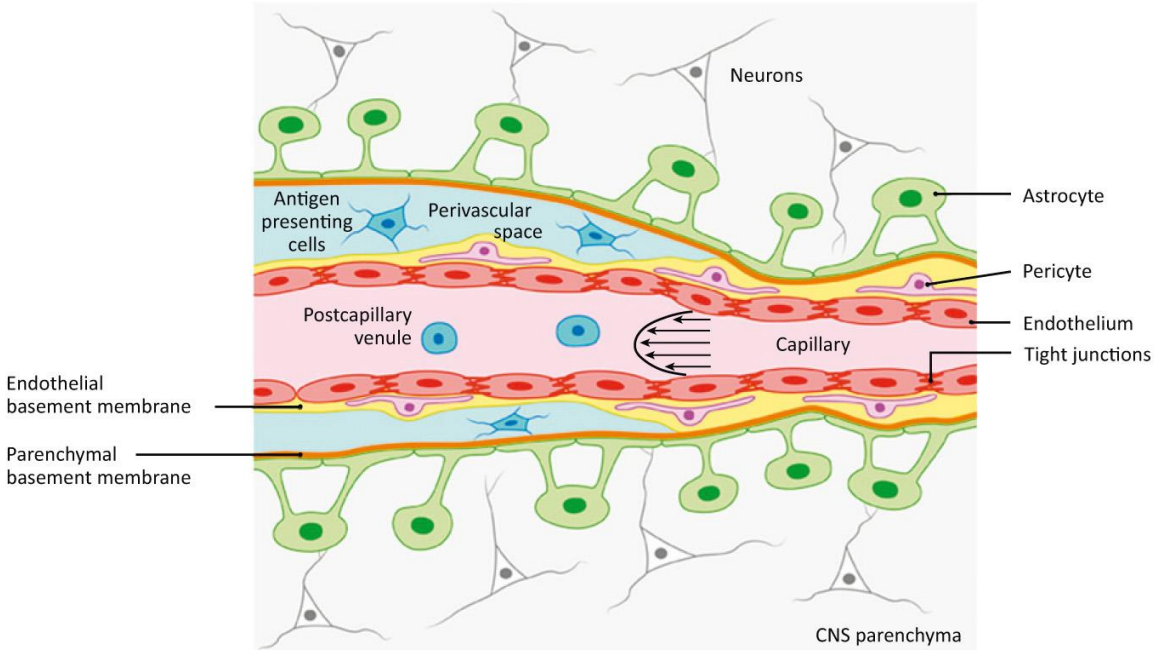

Figure 1.2 Anatomy of the blood-brain barrier. Post-capillary venules and capillaries reach down into the parenchyma of the brain and SC. Their highly specialized endothelial cells (red) show a low pinocytic activity and are connected by tight junctions. The endothelial cells produce an endothelial basement membrane (yellow), which contains pericytes (pink). The basement membrane of postcapillary venules is surrounded by the perivascular space containing cerebrospinal fluid and phagocytes that are supposed to be antigen presenting cells (blue). The capillary basement membrane is directly associated with the glia limitans perivascularis composed of astrocytic end feet (green) and the parenchymal basement membrane (orange). Together, these described structures protect the underlying parenchymal neurons (grey). Modified from (Engelhardt and Ransohoff, 2012).

1.2 Multiple sclerosis

1.2.1 Multiple sclerosis: a short introduction

Multiple sclerosis (MS) is the most common inflammatory disease of the central nervous system. The detailed pathomechanisms underlying MS are unknown, but the body of evidence strongly supports the hypothesis that MS is an autoimmune T cell-mediated disease (chapter 1.2.5, 1.3.1 and 1.3.2). As the name of the disease indicates, multiple focal inflammatory infiltrates and demyelinating plaques can be found in the CNS of MS patients. These lesions are located in the brain, especially in the periventricular white matter (WM) (classically described MS lesions), cerebellum, brainstem and optic nerve (Pierson et al., 2012). Additionally, many patients develop lesions in the spinal cord (Thorpe et al., 1996; Nociti et al., 2005). Today it is known that the grey matter is involved in lesion formation as well and plays an important role in the progression of disability (see chapter 1.2.4). The clinical

symptoms of a patient depend on the affected CNS areas. At disease onset symptoms like impaired vision, due to optic neuritis, and deficits in sensation are present. Later in the disease course sensory impairment is accompanied by paresis and paralysis, ataxia, fatigue, spasticity, cognitive impairment and incontinence (Baranzini et al., 2009).

1.2.2 Epidemiology and clinical phenotypes

The worldwide prevalence of MS can only be estimated and might be in a range between 1.1 and 2.5 million cases. Geographically, areas with the highest frequency for MS are Western and Northern Europe, Canada, Russia, Israel, northern parts of the US, New Zealand and South and East Australia (Pugliatti et al., 2002; Barnett et al., 2009). People living near the equator are less affected (Compston and Coles, 2008). MS typically occurs in early adulthood and affects more often women than men.

The disease course is very heterogeneous. Classically, MS is classified into 3 subtypes: Relapsing-remitting (RR), secondary progressive (SP) and primary progressive (PP). 80-90 % of patients start with a RR disease course, which is characterized by the recovery of physiological functions between the relapses (Bielekova and Martin, 2004; Miller, 2004). CNS lesions of these patients are often characterized by disturbance of the BBB, local oedema and demyelination (Miller et al., 1998). Over time (sometimes several years) most RR MS patients develop a SP disease. In this phase the recovery from symptoms decreases and patients retain progressive neurological deficits. Only 10-20 % of patients start with a PP disease course without acute relapses. These patients show less inflammation in the CNS and more severe axonal loss at earlier time points in the disease (Bashir and Whitaker, 1999; Leray et al., 2010).

1.2.3 Histopathology

The disease course of MS is variable in individuals. Moreover, MS lesions show a wide range of histopathological features in different patients. The analysis of active demyelinating lesions reveals reduced density of myelinated fibres and irregular ensheathment of axons. Four basic pathologic types of active WM demyelinating lesions in MS subtypes were described (Lucchinetti et al., 2000). All four lesion types show inflammatory infiltrates of T cells and macrophages. Furthermore, in the type I lesion activated macrophages and microglia were found to be associated with degenerating myelin (Lucchinetti et al., 2000). Here, the toxic products of these activated cells might cause myelin destruction (Lassmann et al., 2001). The

type II lesion is very similar to lesion type I but additionally shows deposits of antibodies and active complement which may mediate demyelination. In type III lesions distal oligodendrogliopathy might lead to demyelination and in lesion type IV demyelination may take place as a reaction to primary oligodendrocyte damage (Lucchinetti et al., 2000).

1.2.4 Cortical lesions in MS

1.2.4.1 Cortical lesions in MS: an introduction

For a long time MS was described as a disease which is primarily affecting the white matter of the central nervous system. The role of cortical grey matter lesions in the disease pathology was not in the focus of MS research. A disadvantage in former days was that the conventional histological methods and later the classical magnetic resonance imaging (MRI) technique did hardly allow the visualization of cortical lesions.

Today, cortical grey matter lesions in MS are becoming an important field of research again. Improved pathological investigative procedures and MRI techniques, like high field MRI, allow to detect lesions in the grey matter of the brain and SC during *in* and *ex vivo* studies (Kidd et al., 1999; Bozzali et al., 2002). These studies show that cortical demyelinating lesions are all but rare. Additionally, the correlation of medical imaging methods and clinical parameters showed that grey matter lesions are related to the disabilities in MS patients and important indicators for the prognosis of disease development (Rovaris et al., 2006; Fisniku et al., 2008).

Today the pathological classification of cortical lesions as defined by Peterson et al. is widely accepted (Peterson et al., 2001). Cortical demyelinating lesions can be divided in 4 pathological lesion types.

1. The type I lesion is named **leucocortical lesion**. It extends from deeper cortical grey matter layers into white matter regions. The superficial cortical layers are not involved.
2. The type II lesion is called **intracortical lesion**. These lesions are small in size and they are limited in their expansion. They can only be found within the cortex and they are often in close proximity to blood vessels. The superficial cortex and the white matter are not involved.
3. Type III lesions reach from the pial surface into the more superficial cortical layers. These lesions can spread to the cortical layer 4.

4. Type IV lesions extend through the whole cortical layers, but do not involve subcortical white matter areas.
   Type III and IV lesions are also called **sub-pial lesions**.

Cortical damage can be found in the early disease and in further progressed stages.

1.2.4.2 Cortical demyelination in early MS

It is largely accepted that cortical lesions can be secondary to white matter damage due to retrograde degeneration (Simon et al., 2000; Cifelli et al., 2002). However, recently MRI and histological studies have challenged this classical view proposing that the cerebral cortex may represent an onset/early target of the disease process at least in a part of MS patients (Popescu and Lucchinetti, 2012). By using the latest MRI techniques it was shown that cortical lesions are present in 64 % of patients with RR MS and 70 % of patient with SP MS, but also in 37 % of patients with clinical isolated syndrome (Calabrese et al., 2007). Moreover, some MS patients exhibited cortical lesions and atrophy months/years before the MRI evidence of inflammatory lesions in the WM (Calabrese and Gallo, 2009). Also histopathological data evidence that early cortical demyelination and BBB damage can occur before the appearance of WM pathology or in no anatomical association with WM lesions (Bø et al., 2007; Lucchinetti et al., 2011; Popescu et al., 2011). These cortical lesions detected in 40 % of patients in early-stage MS showed, beside a reduction of oligodendrocyte density, a high level of inflammation that argues against a primary degenerative process at least in this early disease state (Lucchinetti et al., 2011). Myelin-laden macrophages and lymphocytes (mainly T cells), also a typical sign of active demyelinating WM lesions, can be found in affected areas (Lucchinetti et al., 2011; Popescu et al., 2011). These cells are often in close proximity to neurons and their processes indicating that these cells might directly promote neuronal damage (Lucchinetti et al., 2011; Popescu et al., 2011). Several examined cortical lesions from biopsies of early MS patients show neuritic swelling as a sign for acute neuronal damage (Lucchinetti et al., 2011). In early MS cortical demyelinated plaques were spatially associated with meningeal inflammation. This was shown especially for the sub-pial lesion type (Lucchinetti et al., 2011).

1.2.4.3 Cortical demyelination in chronic MS

Neuropathological studies focusing on PP and SP MS patients show that cortical demyelinating lesions are numerous and wide spread events (Bø et al., 2003b; Kutzelnigg et al., 2005). Similar to cortical lesions in early MS these lesions were predominantly detected at the depth of the cerebral sulci. The affected areas are the cingulate gyrus, the frontal temporal insular and cerebellar cortices as well as the hippocampi. The paracentral lobule and the occipital lobes of the brain are less often affected (Huitinga et al., 2001; Bø et al., 2003b; Kutzelnigg et al., 2005; Geurts et al., 2007; Gilmore et al., 2009; Papadopoulos et al., 2009) (Choi et al., 2012).

The pathological features of the cortical lesions of chronic MS patients are well-defined and consist of oligodendrocyte and neural damage, as well as loss of these cells (Peterson et al., 2001; Bø et al., 2003a; 2003b; Wegner et al., 2006; Choi et al., 2012). Interestingly, cortical demyelinating lesions of progressive MS patients are generally less inflammatory than white matter lesions and grey matter lesions of early MS patients. Compared with previously mentioned lesions they show a very limited number of lymphocytes and macrophages. Furthermore, there is a lack of complement and immunoglobulin deposition (Peterson et al., 2001; Bø et al., 2003a; 2003b). Ramified microglia cells can be detected in close proximity to neurons (Peterson et al., 2001; Bø et al., 2003a; 2003b). In contrast to the cortical lesions, the meninges of further progressed MS patients show inflammatory infiltrates. These infiltrates are associated with sub-pial lesions (Serafini et al., 2004; Magliozzi et al., 2007; Choi et al., 2012).

1.2.5 MS etiopathogenesis: the autoimmune hypothesis

The described diversity in disease course, lesion localisation and symptoms as well as immunopathological appearance of these lesions may contribute to the fact that the cause of MS and the pathomechanisms are still under discussion. However, even if the formal proof is still lacking there are several lines of evidence that support the hypothesis that MS is an autoimmune T cell-mediated disease with secondary demyelination and tissue damage.

As described in chapters 1.2.3 and 1.2.4, recent MS lesions, both in grey and white matter, are characterized by a massive infiltration of immune cells (mainly T cells) and monocytes/macrophages. It seems reasonable to assume that an immune reaction against CNS antigens can play a major role.Epidemiological studies emphasized the role of a genetic component by showing a significant increase of disease frequency in the relatives of affected

individuals (Dyment et al., 2006; Hemminki et al., 2009). Genome-wide association studies (GWAS) demonstrated that variations in the human leukocyte antigen (HLA) alleles are the main risk factor associated with the susceptibility to MS (International Multiple Sclerosis Genetics Consortium et al., 2007). In addition to the HLA locus, other susceptibility loci have been identified: among these loci, immunologically relevant genes, in particular T helper cell differentiation genes, are over-represented (International Multiple Sclerosis Genetics Consortium et al., 2011). In humans potential auto-reactive $CD4^+$ T cells are known to be part of the normal T cell repertoire (Martin et al., 1992; O'Connor et al., 2001). When these cells by still unknown means become activated in the peripheral lymph nodes, for example by a cross reaction with foreign antigens such as viral peptides (molecular mimicry), they can clonally expand, circulate through the body and accumulate in the CNS (Hemmer et al., 2002). These cells may be pathogenic as shown by experiments with non-human primates (Meinl et al., 1997) and with "humanized" transgenic mice (Madsen et al., 1999). Finally, immunotherapy targeted to T cells as well as to other immune cells (i.e. VLA-4 or CD52 monoclonal antibodies) had significant effects on MS patients (Hohlfeld and Wekerle, 2004). Taken together, it appears that the human immune repertoire contains myelin-reactive T cells that can undergo clonal expansion and have encephalitogenic potential. These findings however do not clarify the specific contribution of these myelin-specific T cells to the pathogenesis of the disease. Our knowledge regarding this point is based on fundamental observations made in animal models of experimental autoimmune encephalomyelitis (EAE).

1.3 Experimental autoimmune encephalomyelitis

1.3.1 The history of experimental autoimmune encephalomyelitis

The concept of MS being an autoimmune disease is strongly based on the animal paradigm of MS, the experimental autoimmune encephalomyelitis (EAE) (Freund and McDermott, 1942; Ben-Nun et al., 1981; Gold et al., 2006; Owens, 2006). In 1928 the first indication that an immune reaction against CNS components leads to brain inflammation was presented by Rivers who investigated epidemics of paralysis in people after vaccination against rabies (Remlinger, 1928; Baxter, 2007). In 1933/35 experimental animals were actively immunized with brain tissue to analyse the ascending paralysis previously seen in vaccinated people in more detail (Schwentker and Rivers, 1934; Rivers and Schwentker, 1935). It was discovered that the immunisation leads to the induction of inflammatory demyelinating lesions in the CNS. These findings together with the development of completes Freund`s adjuvant (CFA),

an emulsion consisting of lyophilised *Mycobacterium tuberculosis* and paraffin oil used to boost immune responses in the recipient animal, led to the development of the animal model EAE (in this form called active EAE: aEAE)(Freund and McDermott, 1942).

Today it is known that EAE can be induced in a variety of animals (rabbits, rodents, monkeys etc.) by active immunisation with myelin antigens and CFA (Olitzky and Yager, 1949; Lipton and Freund, 1952; Genain et al., 1995). The course of disease and the severity of symptoms are species- and strain-dependent. The classical antigen shown to evoke EAE was myelin basic protein (MBP). Furthermore, other myelin antigens like myelin oligodendrocyte glycoprotein (MOG), proteolipid protein (PLP), and non-myelin antigens (for example S-100β, a glia-specific protein expressed primarily in astrocytes) induce EAE as well (Linington et al., 1988; Piddlesden et al., 1993; Kojima et al., 1994; Kaye et al., 2000).

The direct link that EAE is mediated by immune cells came from a study in which lymph node cells of immunized animals were used to transfer EAE to other animals (Paterson, 1960). Another striking finding was that brain-specific $CD4^+$ T cells are able to mediate EAE in healthy animals. In detail, lymphocytes from immunized animals were cultured under conditions favouring the CD4 T cell type. After purification the activated MBP-specific $CD4^+$ T cells were passively transferred into healthy syngeneic recipient animals, which developed a classical EAE after a defined time interval after transfer (Ben-Nun et al., 1981). The newly developed procedure was named passive transfer EAE (ptEAE). In early studies of EAE the general view was that T_H1 cells, characterized by the production of IFN-γ, are the main players in EAE (Baron et al., 1993; Segal and Shevach, 1996; Liblau et al, 1995). Later the IL-17-producing T cell population, named T_H17 cells, were recognized to be important in the induction of EAE as well (Cua et al., 2003; Langrish et al., 2005; Zepp et al., 2011).

1.3.2 Passive transfer experimental autoimmune encephalomyelitis in the Lewis rat

In the ptEAE model in Lewis rats, encephalitogenic MBP-specific T_H1/T_H17 T cells, which are able to infiltrate the CNS, are used to induce the disease (Wekerle, 2008). A big advantage of this approach is, that antigen-specific T cells can be generated *in vitro* and retrovirally engineered to express fluorescent proteins like green-fluorescent protein (GFP) (Flügel et al., 1999). After stable integration of the GFP expression cassette into the genome, the protein is continuously expressed without interfering with T cell function (Flügel et al., 2007). The persistent labelling of these T cells ($T_{MBP\text{-}GFP}$) allows their tracking and their functional characterization in the different compartments during all the disease phases (Flügel et al., 1999). Due to the recent introduction of the two-photon laser scanning microscopy (2P-LSM)

technique into the immunological field, the fluorescently labelled encephalitogenic T cells can be also visualized and tracked in microanatomical environments, like the leptomeningeal areas of the CNS.

1.3.3 Two-photon laser scanning microscopy: A tool to study T cell motility behaviour *in situ*

To visualize and analyse the motility behaviour of effector $T_{MBP\text{-}GFP}$ cells within the meninges or the SC in real-time the technique of 2P-LSM has been used previously (Kawakami et al., 2005a; Bartholomäus et al., 2009). 2P-LSM can be used to scan meningeal CNS tissue in all spatial directions. The generated Z-stack can be used to generate 3-dimensional pictures. If scanning of Z-stacks is performed over time 4-dimensional movies can be generated. Compared with conventional linear microscopy the main advantage of 2P-LSM is that a long-waved laser in near-infrared range (700-980 nm) can be used. The usage of this long-waved laser allows a deeper penetration into the CNS tissue due to reduced scattering of the beam. Moreover, the lower energetic light of this laser induces lower phototoxic damage to the tissue compared to short wave length lasers (Helmchen and Denk, 2005). Therefore, this technique allows the imaging of pathophysiological processes in living animals over extended time periods without interfering with endogenous processes. As well known, due to the inversed correlation between wavelength and its energy, waves of long wavelength have lower energy. Therefore, to reach the energetic level necessary to excite the common fluorophores the two-photon effect is used. This effect that is generated by femtosecond-pulsed lasers takes place when two (or more) photons arriving almost simultaneously at the focal point combine their energy to excite the fluorophore (Denk et al., 1990; Helmchen and Denk, 2005). The excitation of the fluorescent molecules is limited to the meeting point of the two photons, which also defines the area of emission. Hence, there is no emission from other areas and tissue layers beside the focal point of excitation (see fig. 1.3). Of consequence tissue-damage is extremely reduced.

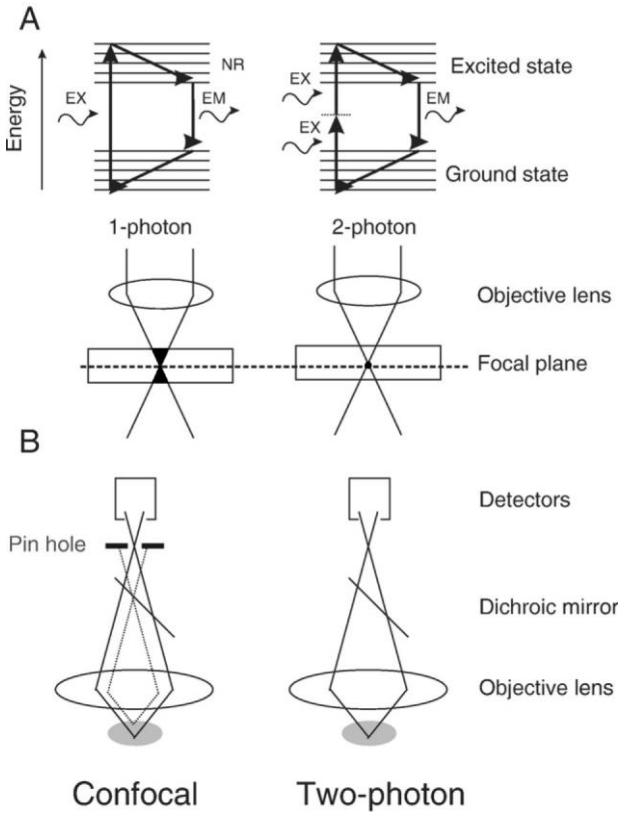

Figure 1.3 Comparison of conventional confocal (left side) and two-photon laser scanning microscopy (2P-LSM) (right side). (A), top row: The upper panel shows the single photon excitation of a confocal microscope on the left side. Here, a fluorochrome is excited by an energy-rich (low wave-length) single photon. Thereby an electron transitions to an excited state from which it subsequently relaxes to energetic ground level. Thereby a part of the energy disperses and the other is converted in emitting fluorescence of higher wave-length light. On the right side, two photons with half of the energy and twice of the wave-length combine their energy by simultaneous absorption to excite an electron of a fluorochrome. (A), bottom row: During confocal microscopy tissue outside the focus point is also exposed to the high energetic light (black triangles). During 2P-LSM, the two- photon effect occurs only at the focus point at the focus plane (black circle). (B) During confocal microscopy the emitted light generated outside the focus point has to be blocked by a pinhole to detect only the light from the focus point. In 2P-LSM the light is only emitted at the focus point. A pinhole is not needed for detection. Adapted from (Flügel et al., 2007).

1.3.4 Passive transfer experimental autoimmune encephalomyelitis in the Lewis rat: The invasion steps of MPB-specific effector T cells from the periphery into the SC.

By combining *in vivo* imaging with *ex vivo* quantification and functional characterization the fate of the transferred $T_{MBP\text{-}GFP}$ cells was followed during all the disease phases (Flügel et al., 2001; Bartholomäus et al., 2009; Odoardi et al., 2012).

Preclinical phase

Just after transfer and independently from the state of the BBB the injected $T_{MBP\text{-}GFP}$ cells do not enter directly the CNS but they undergo a complex migratory tour through the periphery. Few minutes after injection effector T cells disappear from the blood circulation and enter the lung. From here T cells move to the bronchus-associated lymphoid tissue (BALT) and to the lung-draining mediastinal lymph nodes. Afterwards they re-enter the blood circulation and travel to the spleen (72-84 h after transfer) before they invade the SC (approximately 3 days after transfer) shortly before the onset of clinical symptoms. Already in the lung, $T_{MBP\text{-}GFP}$ cells drastically change their gene-expression profile: they down-regulate their activation and proliferation program and up-regulate locomotion and cell adhesion molecules. Moreover, they acquire the capacity to respond to inflammatory chemokines like CXCL9, 10 and 11. This acquired migratory phenotype allows them to overcome the BBB (Flügel et al., 2001; Odoardi et al., 2012).

Clinical phase

2P-LSM allowed visualizing the step of invasion of effector T cells in the target organ, the CNS (Bartholomäus et al., 2009). Due to the fact that inflammation in EAE mainly affects the SC most studies examine this part of the CNS and not the brain. It is extensively described that in order to get to the site of inflammation successive interactions of specific adhesion and/or signalling molecules on leukocytes and blood vessel endothelial cells are essential. First of all interactions between selectins (on endothelial cells) and their ligands (on leukocytes) allow leukocytes to adhere to the inflamed endothelium despite the blood flow. Moreover, integrins (like very late antigen-4, VLA-4 also known as α4β1) might be involved in this process. As a consequence of these interactions leukocytes start to roll on the vessel endothelium. Leukocyte arrest during rolling is rapidly triggered by chemokines, which activate integrins (VLA-4 or lymphocyte function-associated antigen-1 (LFA-1, also called αLβ2-integrin)) on the surface of leukocytes and thereby mediate their binding to their ligands, such as intracellular adhesion molecule-1 (ICAM-1) and vascular cell adhesion molecule-1 (VCAM-1), expressed by endothelial cells (Ley et al., 2007). Considered these well-described extravasation steps, it was surprising for Bartholomäus and colleagues to observe that the majority of effector $T_{MBP\text{-}GFP}$ cells (around 80 %) in the leptomeningeal vessels of the SC were not rolling but crawling on the intraluminal surface and this mainly against the blood flow (Bartholomäus et al., 2009). The crawling was specific of the SC vessels, it was VLA-4-mediated and it was required for the next extravasation step. Blocking

of VLA-4 via monoclonal antibody treatment abolished both crawling and the transmigration of $T_{MBP\text{-}GFP}$ cells. The integrin LFA-1 was less important for the crawling process. Interestingly, also CNS-ignorant effector T cells reactive against ovalbumin ($T_{OVA\text{-}GFP}$ cells) crawled on the leptomeningeal surface. However, in contrast to $T_{MBP\text{-}GFP}$ cells the crawling duration of $T_{OVA\text{-}GFP}$ cells (i.e. the time these cells spent in crawling) was shorter (12 min against 15 minutes) and the percentage of crawling cells was lower (50 %). Moreover, very few $T_{OVA\text{-}GFP}$ cells were able to enter the SC (Bartholomäus et al., 2009).

After diapedesis, $T_{MBP\text{-}GFP}$ cells transmigrated into the leptomeningeal area (fig. 1.4) where they started to monitor the abluminal vascular surface and, thereafter, the leptomeningeal space (fig. 1.4). Here, encephalitogenic T cells formed first short-lasting and later, with increase of inflammation, more long-lasting contacts with perivascular and meningeal phagocytes (fig. 1.4), which potentially can present their specific antigen. After the recognition of the antigen, the T cells became re-activated. Consequently, they up-regulated pro-inflammatory cytokines (IFN-γ, IL-17, TNF-α, IL-2) and surface activation markers (OX40, IL-2R) (Bartholomäus et al., 2009). In this re-activated state $T_{MBP\text{-}GFP}$ cells were able to induce further inflammation and penetrated deep into the SC parenchyma, first entering the white matter and then the grey matter, reaching a more or less equal distribution within these two SC compartments. This process coincided with the onset of clinical symptoms.

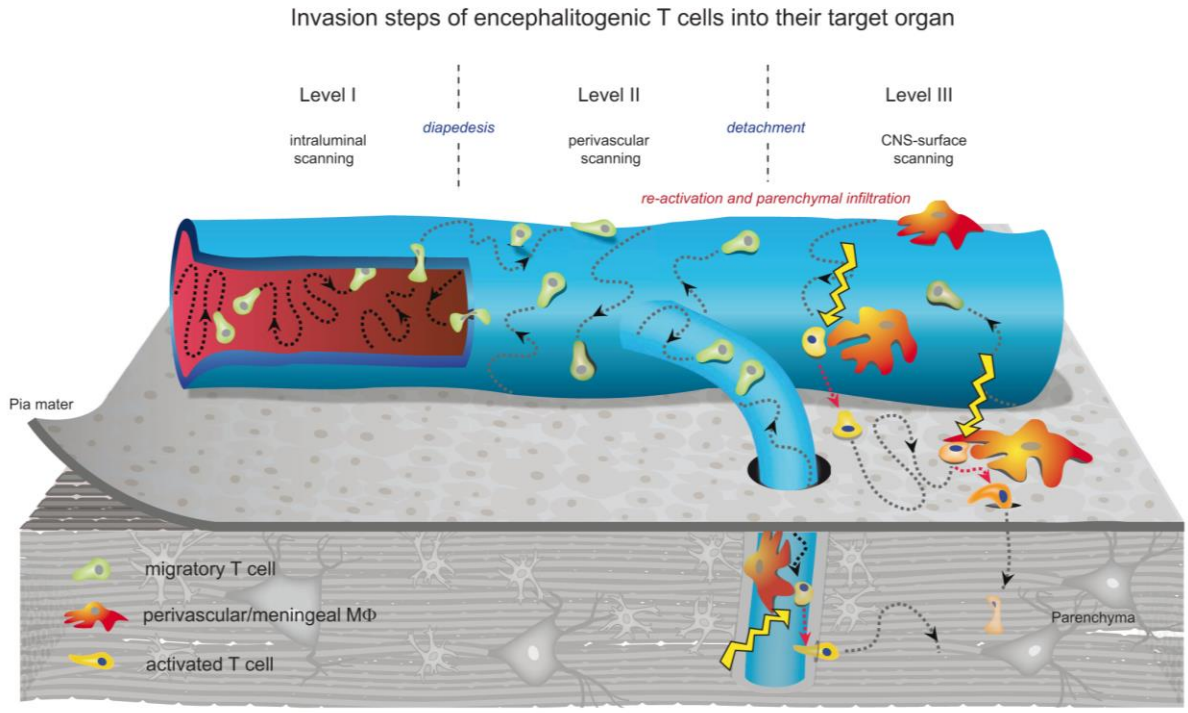

Figure 1.4 Illustration of the different invasion steps of MPB-specific effector T cells into the SC parenchyma. At Level I $T_{MBP\text{-}GFP}$ cells have reached the SC leptomeningel vessels. Here the $T_{MBP\text{-}GFP}$ cells scan the vessel surface and crawl intraluminally. After diapendesis into the leptomeningeal area $T_{MBP\text{-}GFP}$ cells start to scan the perivascular surface at Level II. Later $T_{MBP\text{-}GFP}$ cells detach from the abluminal vessel wall and start to scan the leptomeningeal area at Level III. During this process they get into contact with local antigen-presenting cells, which re-activate the $T_{MBP\text{-}GFP}$ cells and promote the invasion deeper into the SC tissue. Adapted from (Bartholomäus et al., 2009).

1.3.5 T cell activation and the calcium-calcineurin-NFAT pathway

The activation of $CD4^+$ CNS antigen-specific T cells in the meningeal environment is essential for the invasion into the CNS parenchyma during the inflammatory processes (Flügel et al., 1999; Kawakami et al., 2004; Bartholomäus et al., 2009). Activation of a matured CD4 T cell occurs when APCs display the cognate antigen on their MHC class II molecules to the T cell (Goverman, 2009; Call, 2011). The T cell recognizes the presented antigen with its appropriate T cell receptor (TCR). Besides the described molecules, a set of co-stimulatory molecules and adhesion molecules are necessary for the full activation of a T cell (reviewed in Grakoui et al., 1999; Sharpe and Freeman, 2002; Huppa and Davis, 2003). After the binding and interaction of T cell receptor with the cognate antigen and appropriate ligands on APCs, the propagation of the T cell activation signal is carried out by specific intracellular signalling cascades. One important intracellular T cell activation cascade is the calcium-calcineurin-NFAT (nuclear factor of T cell activation) pathway (fig. 1.5). Briefly, after the binding of the cognate Ag presented on an MHC molecule to the TCR, an intracellular signalling pathway is initiated (for more details see fig. 1.5) which leads to the activation of the phosphatase calcineurin, the main modulator of NFAT. Once activated, calcineurin binds to the regulatory domain of NFAT and dephosphorylates its serine residues (Macian, 2005). The dephosphorylated NFAT is able to translocate into the cell nucleus and to induce gene transcription by binding to specific DNA regulatory regions of NFAT target genes via a DNA binding motif within its REL-homology domain (Macian, 2005). NFAT and its transcription-factor partners, which are also activated by TCR or co-stimulator binding, interact with one another mediating specific gene expression and thereby typical functional changes in activated T cells, like the expression of cytokines. The translocation of NFAT into the nucleus is an early event of T cell activation. The nuclear activity of NFAT is terminated by re-phosphorylation of the protein by export kinases leading to the nuclear export of NFAT (fig. 1.5) (Macian, 2005).

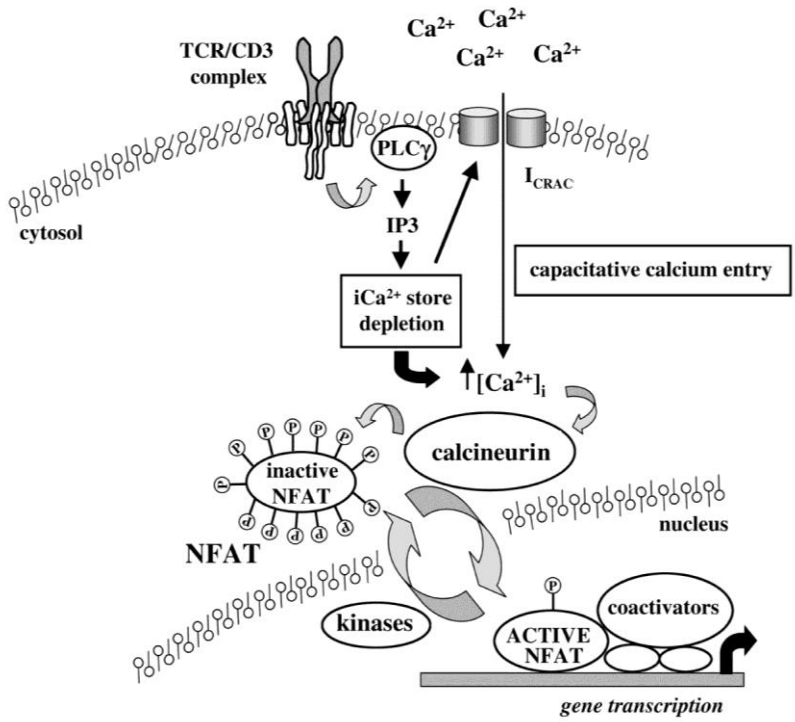

Figure 1.5 The calcium-calcineurin-NFAT pathway. Ligation of the TCR triggers the activation of the NFAT pathway. First the receptor-associated tyrosine kinase activates PLC-γ. This enzyme catalyses the synthesis of IP3. IP3 binds to its receptor at iCa^{2+} stores and causes the depletion of Ca^{2+}. Further elevation of the intracellular Ca^{2+} level is mediated by the opening of I_{CRAC} in the plasma membrane. The increase of intracellular Ca^{2+} leads to the activation of calcineurin, which dephosphorylates the NFAT protein and thereby induces its nuclear translocation. In the nucleus NFAT and co-activators mediate specific gene expression. Ca^{2+}, calcium ion; iCa^{2+}, intracellular calcium ion; I_{CRAC}, Ion channel calcium-release-activated calcium ion channel; IP3, inositol-1,4,5-triphosphate; NFAT, nuclear factor of T cell activation; PLC-γ, phospholipase C-γ; TCR, T cell receptor. Modified from (Cope, 2002).

1.3.6 Disease course of ptEAE in Lewis rats

Compared to MS EAE is less heterogeneous in its clinical presentation. The previously described classical Lewis rat EAE (chapter 1.3.2 and following chapters) induced by passive transfer of $T_{MBP\text{-}GFP}$ cells starts with an asymptomatic phase. After this symptom-free preclinical phase animals develop a rapid progressing monophasic flaccid paralysis starting around 3 days after transfer of encephalitogenic T cells (fig. 1.6). The first clinical sign of disease is the loss of body weight. Afterwards animals develop a flaccid tail and gait disturbances caused by beginning weakness of the hind limbs. At the peak of the disease, 4-5 days after T cells transfer, the animals show a complete hind limb paralysis and bladder dysfunction. Afterwards the animals recover completely from the disease (fig. 1.6).

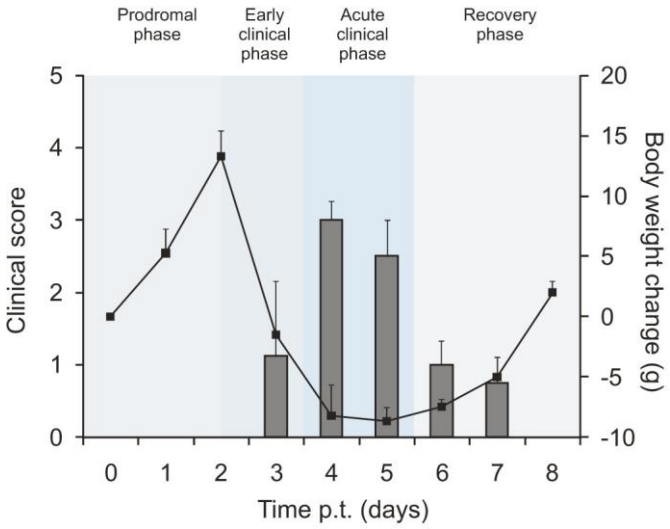

Figure 1.6 The monophasic disease course of ptEAE in Lewis rats. Shown are the different phases of EAE. The disease is starting with a prodromal or symptom-free preclinical phase. In the early clinical phase the animal is losing body weight and shows the first symptoms of disease. During the acute clinical phase the disease maximum is reached. The last phase is characterized by the recovery of the animals. Clinical score system: 0, no sign of disease; 1, tail paralysis; 2, gait disturbance; 3, hind limb paralysis; 4, tetraparesis and 5, moribund. Adapted from (Bartholomäus et al., 2009).

The clinical presentation reflects indirectly the inflammatory area, in which T_{MBP} cells have infiltrated. The paralysis in the rat ptEAE model is mainly caused by injury from infiltrating immune cells into the SC (Pender et al., 1995).

1.3.7 Myelin basic protein: the classical antigen of EAE

In the described rat ptEAE model (see above), T cells reactive against MBP are used to induce the disease. MBP is one of the major myelin proteins in the CNS. Evidence that MBP is important for the compaction of myelin comes from a naturally occurring *shiverer* mouse mutant, in which a large part of the MBP gene is deleted. As a consequence the *shiverer* mutant lacks most compact myelin in the CNS (Roach et al., 1985). Beside its importance for the adhesion of the cytosolic surface of multilayered compact myelin, MBP is described to interact with actin, tubulin, Ca^{2+}-calmodulin, and clathrin, as well as negatively charged lipids (Boggs, 2006). The latter allows MBP to bind to the cytosolic surface of the oligodendrocyte membrane (fig. 1.7). In the rat the pathogenic role of T cells reactive against MBP is well established. In human multiple sclerosis, demyelination of neuronal fibres may occur as a consequence of an autoimmune attack, directed against myelin antigens like MBP. However

the definition of a single protein, which is the target of the immune response is still elusive (Hemmer et al., 2002) .

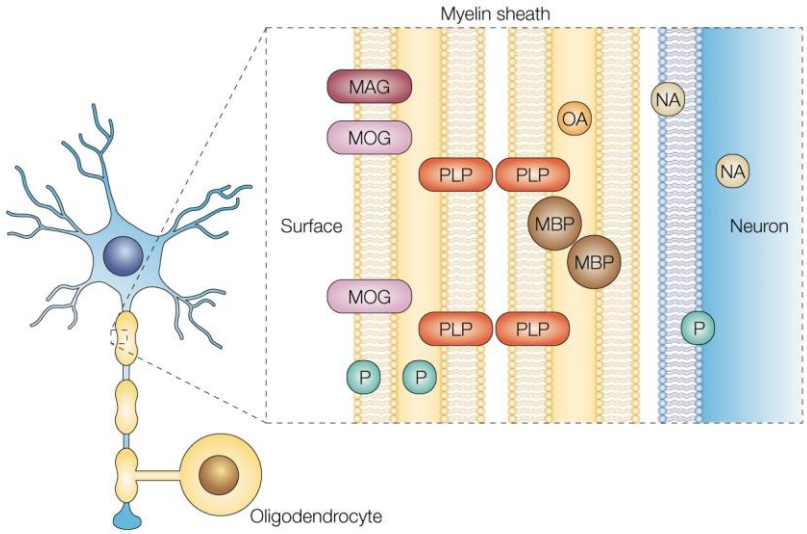

Figure 1.7 Myelinated neuron of the central nervous system and its proteins. The neuronal axons (blue) of the central nervous system are isolated by myelin sheaths formed by oligodendrocytes (yellow). The magnification shows the plasma membrane of oligodendrocytes wrapped around the axon and the localization of myelin proteins within the lipid bilayer. Some myelin and neuronal proteins are potential antigens of the autoimmune attack in CNS diseases like MS. Proteins, exogenously introduced into CNS structures by pathogens might also mediate autoimmunity. Myelin antigens like MBP are used to induce experimental autoimmune encephalomyelitis, the classical animal model for multiple sclerosis. MAG, myelin-associated glycoprotein; MBP, myelin basic protein; MOG, myelin oligodendrocyte glycoprotein; NA, antigen resident in neurons; OA, antigen resident in oligodendrocytes; P, proteins encoded by foreign DNA; PLP, proteolipid protein; Modified from (Hemmer et al., 2002).

1.3.8 Limited diversity of EAE models

Whereas the majority of MS patients develop inflammatory lesions in the supratentorial area, in rodent EAE models the lesions are generally localized in the SC (Pender et al., 1995). The factors determining the topography and the dynamics of inflammatory lesions in the different CNS compartments are still not clarified.

Genetic factors could play a role considered that cortical demyelination can be modelled in certain rat strains by immunization with MOG protein without further treatment (Storch et al., 2006). Cell-intrinsic properties have been implicated in the disease phenotype. It was shown that the ratio between T_H1 and T_H17 cells influences whether these cells infiltrate the brain or the SC. MOG peptide-specific T cells infiltrate and inflame brain parenchyma only when

T_H17 cells outnumber T_H1 cells; if the immune response is driven by T_H1 cells, classical SC infiltrates are observed (Stromnes et al., 2008). Moreover, it has been proposed that differential chemokine receptor or integrin expression might guide the effector T cells in different CNS compartments. T_H17 but not T_H1 cells were able to infiltrate the uninflamed choroid plexus via the CCR6-CCL20 axis in a mouse EAE model (Reboldi et al., 2009). Moreover, T_H17 cells but not T_H1 cells entered the supraspinal area in an LFA-1-dependent manner. Blockage of α4-integrin on T_H17 cells prevented the α4-dependent entry into the SC favouring brain infiltration and thereby inducing an ataxic syndrome in mice (Rothhammer et al., 2011).

Apart from effector T cell-intrinsic properties the differential lesion localization in the CNS compartments may also be due to different tissue responsiveness to certain cytokines. In mouse EAE it was suggested that IFN-γ receptor signalling of SC-resident cells is crucial for the induction of inflammation. In contrast, this signal inhibits cerebellar and brain stem inflammation (Wensky et al., 2005; Lees et al., 2008). Finally, other tissue-intrinsic properties like adhesion molecule expression, laminin composition of the basement membrane, local chemokine milieu or endothelia junction structure and function can play a role (Engelhardt and Sorokin, 2009).

1.3.9 Cortical lesions in rodent EAE models

Due to the fact that in the majority of rodent EAE models T cell infiltration mainly affects the SC, the possibilities to study the pathogenesis of cortical lesions are limited. In particular there is a lack of models mimicking cortical MS lesions. Supratentorial demyelination resembling the one observed in MS patients has been described in a marmoset model (Pomeroy et al., 2005; Merkler et al., 2006a). Due to the difficulties in animal husbandry this model cannot be widely used. Another model, which might reflect some features of cortical MS lesions, is the rat focal cortical EAE (Merkler et al., 2006b). Here, a stereotactic injection of the pro-inflammatory cytokines tumor necrosis factor-α (TNF-α) and IFN-γ directly into the cortex of MOG pre-immunized Lewis rats evokes sub-pial and also some intracortical, vessel-associated demyelinating lesions associated with inflammatory infiltrates and complement deposition. (Merkler et al., 2006b).

Cortical infiltration has also been induced in aEAE and ptEAE by using neuronal antigens like contactin-2/TAG-1 and β-synuclein. Contactin-2/TAG-1 has emerged as a potential autoantigen recognized both by autoantibodies and T_H1/T_H17 cells by a proteomic approach on human brain tissue (Derfuss et al., 2009). It is expressed by different neuronal cell

populations and is localized at the juxtaparanodal region of myelinated axons. Transfer of TAG-1-specific T cells in Lewis rats induced very mild clinical symptoms mainly characterized by weight loss and transient loss of the tail tone. Histopathology studies showed mainly white matter and limited grey matter inflammation both in brain and SC largely restricted to the perivascular area (Derfuss et al., 2009).
Cortical inflammation was also described after active immunisation with β-synuclein peptides or passive transfer of T cells reactive against these peptides as detailed in the next paragraph.

1.3.10 The β-synuclein protein - a potential antigen of MS

The synuclein family comprises the three small, soluble proteins α-, β- and γ-synuclein (George, 2002). All synucleins are expressed in vertebrates, predominantly in neural tissue. The cellular functions of the synucleins are unknown. They might play a role in the regulation of membrane stability and turnover (Colley et al., 1997; Abeliovich et al., 2000; Murphy et al., 2000). The most well-known member of the synuclein family is α-synuclein. Under normal conditions α-synuclein is expressed in neurons whereas aggregated forms of the protein can also be found in somal inclusions of nigral dopaminergic neurons, called Lewy bodies, which are characteristic of sporadic and inherited forms of Parkinson`s disease (Mouradian, 2002). Interestingly, the α-synuclein level is elevated in the cerebrospinal fluid of MS and neuromyelitis optica patients. Therefore it might be an indicator for the extent of neuronal damage in these inflammatory demyelinating diseases (Wang et al., 2012).

The β-synuclein protein is expressed predominantly in the CNS. It is the most conserved protein of the synuclein family. For example rodent β-synuclein is very similar to the one expressed in humans (it is to 97.8 % identical)(Lavedan, 1998). It is built up by 134 amino acids and highly expressed in the grey matter. In the human CNS the expression of β-synuclein is starting during the development and maturation of the substantia nigra (Galvin et al., 2001). In the adult human CNS, β-synuclein expression expands to cortical regions as well as the thalamus, hippocampus, caudate nucleus and in the amygdala (Lavedan, 1998; Giasson et al., 2001). In cerebellum and SC the expression is more limited compared to cerebral tissue (Giasson et al., 2001). In rat and mouse nervous system it is expressed in the spinal cord, cerebellum and brain. More specifically, in rat brain it is expressed in the cortex, striatum, thalamus, olfactory bulb, hippocampus and less abundantly in the brain stem (Jakes et al., 1994; Iwai et al., 1995; Murphy et al., 2000; Giasson et al., 2001). Furthermore, the protein can be detected in the dorsal root ganglion perikarya and their axons. Contrary to

described dorsal root ganglion neurons, it is postulated that motor neurons lack the expression of β-synuclein, at least in humans and rodents (Giasson et al., 2001). A closer look at the CNS neuropil shows the predominantly synaptic distribution of β-synuclein, especially in the presynaptic nerve terminal, as a soluble protein (Maroteaux et al., 1988; Maroteaux and Scheller, 1991; Jakes et al., 1994; Iwai et al., 1995; Withers et al., 1997; Murphy et al., 2000). The physiological function of β-synuclein is unknown, but there are indications that it is involved in membrane-associated processes and might play a role in synaptic transmission (Jenco et al., 1998).There are indications from the rat animal models that the neuronal β-synuclein might play a role in the autoimmune disease MS. Mor and Cohen selected peptides which were predicted to fit into the binding motive of the Lewis rat MHC class II I-A molecule RT1.B1. The chosen peptides were of various functions (for example surface receptors, structural or synaptic proteins) and, moreover, associated with neurodegeneration. By analysing the potential of these peptides to act as self-antigen and to induce CNS disease it was shown that only one of the 70 tested peptides was able to induce an EAE-like phenotype (Mor et al., 2003; Mor and Cohen, 2006). The immunisation with the non-myelin β-synuclein$_{93\text{-}111}$ peptide and passive transfer of β-synuclein$_{93\text{-}111}$ peptide-activated T cells in Lewis rats induced the classical monophasic disease with moderate paresis of the hind limbs (Mor et al., 2003; Mor and Cohen, 2006). The mild EAE symptoms could be aggravated by pre-treatment with cyclophosphamide or radiation (Mor et al., 2003; Mor and Cohen, 2006). In a study of the Ben-Nun working group, the pre-treatment with cyclophosphamide or radiation was mandatory to induce EAE-like symptoms in Lewis rats (Kela-Madar et al., 2009). Moreover, in all three studies β-synuclein peptide (including at least the amino acids 92-110)-specific T cell clones were generated. The clones were pathogenic and caused mild clinical EAE symptoms (Mor et al., 2003; Kela-Madar et al., 2009). In the study of Mor in 2003 perivascular and parenchymal mononuclear cell infiltrates were found in SC and the cerebral cortex (Mor et al., 2003). Other possible underlying pathomechanisms of β-synuclein-induced EAE were not further analysed in these studies. Overall, these studies link neuronal antigens to EAE and give hints about a possible Ag, which might be involved in primary anti-neuronal immune reactions and neuronal damage within some MS patients.

1.4 Aims of the project

In this thesis my aim was to investigate the mechanisms responsible for the homing behaviour of effector T cells in the different CNS compartments. For this purpose GFP-transduced effector T cells reactive against myelin basic protein ($T_{MBP\text{-}GFP}$) that are known to home preferentially in the SC were established *in vitro* and tested *in vivo* for their pathogenic potential by passive transfer in Lewis rats. The distribution of these cells in the periphery and in the different CNS compartments (brain and SC meninges, brain and SC parenchyma) was investigated by using histology and flow cytometry. The expression of cytokines and chemokine receptors that may be responsible for the different homing behaviour was evaluated by quantitative real-time PCR during the EAE course. In order to characterize the invasion pattern and the motility behaviour of these effector T cells in the target tissues two-photon microscopy was performed on SC and brain meninges. The activation level of $T_{MBP\text{-}GFP}$ cells in the CNS parenchyma was evaluated by using a genetically encoded NFAT biosensor. Finally, in order to investigate if antigen specificity can play a role in determining the distribution of the inflammatory lesions, fluorescently labelled effector T cells reactive against the neuronal antigen β-synuclein ($T_{\beta Syn\text{-}GFP}$) were established and compared *in vitro* and *in vivo* with $T_{MBP\text{-}GFP}$ cells.

2. Materials and Methods

2.1 Materials

2.1.1 Proteins

Albumin from chicken egg white (OVA)	Sigma Aldrich
β-synuclein$_{93-111}$ peptide (βSyn) from rat	Peptide synthesis service, Biochemical Institute, Charité Berlin
CCL5 (recombinant Cotton Rat)	R&D Systems
CCL19 (recombinant Mouse)	R&D Systems
CCL20 (recombinant Rat)	R&D Systems
CXCL11 (recombinant Murine)	PeproTech
CXCL12 (recombinant Rat)	PeproTech
Myelin basic protein (MBP) from guinea pig	in-house production

2.1.2 Antibodies

Primary Antibodies

Mouse anti-rat CD4 Domain 1 monoclonal antibody IgG1	AbD Serotec
Mouse anti-rat CD8α monoclonal antibody IgG1	AbD Serotec
Mouse anti-rat CD25 monoclonal antibody IgG1 (IL-2R alpha chain)	AbD Serotec
Mouse anti-rat CD134 monoclonal antibody IgG2b (OX40)	AbD Serotec

Mouse anti-rat TCR alpha/beta monoclonal antibody IgG1	AbD Serotec

Secondary Antibodies

Goat anti-mouse IgG (H+L) antibody (allophycocyanin (APC) – conjugated)	Jackson ImmunoResearch Laboratories

2.1.3 Media and buffers

ACK buffer	- 0.15 mol/L NH_4Cl (Roth) - 1 mmol/L $KHCO_3$ (Roth) - 0.1 mmol/L Na_2×EDTA (Roth) - adjusted to pH 7.2 – 7.4 with HCl (Roth)
Blocking buffer	- 1x PBS (in-house production) - 5 % rat serum (in-house production)
Decalcification buffer	- 14 % ethylenediaminetetraacetic acid tetrasodium salt hydrate (Sigma) - 86 % 1x PBS (in-house production) - adjusted to pH to 7,4 with glacial acetic acid (Roth)
Eagles HEPES (EH) medium	- 188.3 g/10L DMEM powder (Invitrogen) - HEPES 1M (Roth)
Freezing medium day 2	- 80 % heat-inactivated horse serum (Biochrom AG) - 10 % TCM (in-house production) - 10 % DMSO (Roth)
Freezing medium day 6/7	- 50 % heat-inactivated horse serum

	(Biochrom AG) - 40 % TCM (in-house production) - 10 % DMSO (Roth)
Isotonic Percoll	- 9x Vol Percoll (GE Healthcare) - 1x Vol. 10x PBS (in-house production)
Lymohocyte seperation medium LSM 1077	PAA
Percoll Underlay	- 7 mL Isotonic Percoll - 3.9 mL 1x PBS (in-house production)
Perm/Wash Buffer	BD Biosciences
Phosphor buffered salt solution (PBS, 10x)	- 8.10 mM Na_2HPO_4 (Roth) - 1.47 mM NaH_2PO_4 (Roth) - 137 mM NaCl (Roth) - 2.68 mM KCl (Roth) - adjusted to pH 7.2
Re-stimulation medium (RM)	- TCM (in-house production) - 1 % rat serum (in-house production)
T cell growth medium (TCGM)	- TCM (in-house production) - 10 % heat-inactivated horse serum (Biochrom AG) - 10 % conditioned medium from splenocytes treated with the mitogen Concanavalin A (ConA supernatant) (in-house production)
T cell medium (TCM)	- DMEM (Invitrogen) - 10 ml non-essential amino acids (Invitrogen) - 10 ml penicillin / streptomycin (Invitrogen)

	- 10 ml sodium pyruvate (Invitrogen) - 10 ml L-glutamine (PAN Biotech GmbH) - 10 ml L-asparagine monohydrate (Sigma Aldrich) - 4 µl 2-β-mercaptoethanol (13.6 mol/L) (Invitrogen) - per litre
Thawing medium	- 90 % EH medium (in-house production) - 10 % heat-inactivated foetal bovine serum (Biochrom AG)

2.1.4 Procedure Kits

qPCR Master Mix	Eurogentec
RevertAid™ First Strand cDNA Synthesis Kit	Thermo Scientific
RNeasy® Micro Kit	Qiagen
RNeasy® Mini Kit	Qiagen
RNase-Free DNase Set	Qiagen

2.1.5 Chemicals / Sera / Solvents etc.

Acetic acid (glacial)	Roth
Agarose Low Melt	Roth
Beads (BD CaliBRITE™)	BD Bioscience
β-mercaptoethanol	Roth

Chloroform	Roth
Collagenase	Sigma Aldrich
Concanavalin A	Roth
Concanavalin A supernatant	In-house production
Dextran tetramethylrhodamine (2.000.000 MW)	Invitrogen
Dextran Texas Red® (3.000 MW, 70.000 MW)	Invitrogen
Diethyl ether	Roth
Dimethyl sulfoxide (DMSO)	Roth
Distilled water DNase/RNase-free	Invitrogen
DMEM powder	Invitrogen
D(+)-Sucrose	Roth
Ethanol	Roth
Foetal bovine serum	Biochrom AG
Glycogen	Sigma
G418-Sulphate	Invitrogen
HEPES	Invitrogen
Horse serum	Biochrom AG
Hydrochloric acid (HCl)	Roth
Incomplete Freund's Adjuvant	Difco Laboratories
Isoflurane	Abbott
Isotone sodium chloride solution (NaCl 0.9 %)	Braun
Ketamine (10 %)	Medistar Arzneimittelvertrieb GmbH

M. Tuberculosis H37Ra	Difco Laboratories
OptiPrep	Axis-Shield
Paraformaldehyde (PFA)	Roth
Puromycin	Roth
QIAzol® Lysis Reagent	Qiagen
Sodium chloride	Gibco
Thymidine, (methyl-3H)	Hartmann Analytic
Tissue Tek O.C.T Compound	Sakura Finetek
Trypan blue solution (0.4 %)	Sigma Aldrich
Trypsin EDTA (10-fold)	PAA
Xylariem	Ecuphar
2-propanol	Roth
4`,6-diamidino-2-phenylindole	Sigma Aldrich

2.1.6 Materials

Base Molds (24 mm x 24 mm)	Thermo Scientific
Catheter Vasofix Safety	Braun
Cell strainer	DB Falcon
Cover Glasses (24 mm x 60 mm)	Geyer
FACS Tubes	BD Falcon
Flat Deck Thermo-Fast detection plates	Thermo Scientific
Fluoromount-G	SouthernBiotech
HTS Transwell®-96 Well Permeable Supports	Corning

(5.0 µm Pore Size Polycarbonate Membrane)	
Microtome blades	Leica
Nunclon™Surface 96 well dish	Nunc
Perfusor FM	BBraun
Petri Dish (94 mm x 16 mm)	Greiner
PP tubes sterile (15 ml / 50 ml)	Greiner
Prophyclean dental drill tip	EVE
Sieve (metal)	UMG Werkstatt
SuperFrost Plus microscope slides	Thermo Scientific
Syringe needles (Sterican, different sizes)	Braun
Syringes (1 ml, 5 ml, 10 ml, 20 ml)	Omnifix
Tissue Culture Dish (60 mm x 15 mm, Cell+)	Sarstedt
Tissue Culture Dish (100 mm x 20 mm, Cell+)	Sarstedt
Tuberculin syringe	BD Falcon

2.1.7 Instruments and equipment

Advanced single animal pressure-controlled ventilator	Harvard Apparatus
AxioCam HSM	Carl Zeiss AG
Axio Observer	Carl Zeiss AG
Balance BL3100	Satorius

Balance CP124S	Satorius
BD FACS Aria	BD Biosciences
BD FACS Calibur	BD Biosciences
β-Counter	Perkin Elmer
Centrifuge 5415R	Eppendorf
Centrifuge 5810R	Eppendorf
Cryostat CM3050 S	Leica Biosystems
Heating pad	Telemeter Electronic GmbH
Heraeus Multifuge 1-SR	Thermo Scientific
Illuminator HXP 120 C	Carl Zeiss AG
Incubator Hera Cell 240	Thermo Scientific
Isoflurane vaporizer	Uno Roestvaststaal BV
Laminar Flow Hera Safe	Heraeus
Laser Scanning Microscope 710	Carl Zeiss AG
McIlwain Tissue Chopper	Mickle Laboratory Engineering Company
Neubauer counting chamber	Optic Labor
OHMEDA 5250RGM	GE Healthcare
Perfusion pump	Ismatec SA
pH meter	inoLab
Shandon Cytospin 4	Thermo Electron Corporation
StepOnePlus Real-Time PCR System	Applied Biosystems
Thermo-controller	TC-1, elektronische Werkstatt, UMG
Vortex-Genie	Scientific Industries

10 W Ti: Sapphire chameleon laser	Coherent Inc.

2.1.8 Computer programs

Animal Monitor software 7.3x	Volker Staiger MPI of Neurobiology
Axiovision 4	Carl Zeiss AG
BD FACS Diva Software V 6.1.3	BD Bioscience
CellQuest Pro	BD Bioscience
FlowJo V10	Tree Star, Inc.
Graph Pad PRISM	Graphpad Software, Inc.
Office 2010	Microsoft
Photoshop CS 5	Adobe Systems, Inc.
Primer Express 3.0	Invitrogen
StepOne™ Software v2.0	Applied Biosystems
Zen 2009 software	Carl Zeiss AG

2.2 Methods

2.2.1 Animals

For all experiments Lewis rats on a LEW/Crl background (*Rattus norvegicus*) were used. The animals were bred and kept at the animal facility of the university medical centre Göttingen or obtained from Janvier (Le Genest St Isle, France). All experiments were approved by the appropriate committee in Braunschweig, Germany.

2.2.2 Active EAE / Immunization

Active EAE was induced by immunization of 8 to 10 week old female rats subcutaneously (into the base of the tail and into the hind limb popliteal cavity) with 150 µl guinea pig MBP protein (1 mg/ml) or β-synuclein$_{93-111}$ peptide (βSyn) (amino acid sequence: LKPEEVAQEAAEEPLIEPL) (0.8 mg/ml) emulsified in an equal volume of complete Freund`s adjuvant containing *Mycobacterium tuberculosis* (2 mg/ml). The emulsion was prepared with the help of tuberculin glass syringes and a custom-made homogenizer. MBP was isolated from guinea pig brain as described in literature (Eylar et al., 1974). Briefly, guinea pig brain homogenates were freed of lipids via methanol/chloroform, followed by acidic extraction, neutralization, ammonium sulphate and acetone precipitation. Animals were sacrificed for primary T cell culture (see chapter 2.2.3.2.) or kept for the analysis of clinical disease progression. In the latter case the body weight of the animals was determined over the whole experimental period and animals were observed for disease symptoms and behavioural abnormalities. Clinical signs of classical EAE were assessed according to the following score system: 0, no sign of disease; 0.5, loss of tail tonus; 1, tail paralysis; 2, gait disturbance; 3, hind limb paralysis; 4, tetraparesis and 5, moribund. Animals were sacrificed when reaching a score of 4.5. Animals immunized with βSyn were moreover examined for uncommon disease signs like front limb weakness/paralysis, ataxia or hemiparesis.

2.2.3 Primary T cell culture

2.2.3.1 Culture of packaging cells

GP+E86 packaging cells, producing a replication-deficient GFP or NFAT yellow fluorescent protein (YFP) retrovirus, were used to transduce T cells. The retroviral vector pMSCV used for the gene transfer is derived from the murine embryonic stem cell virus (MESV) and

promotes the transfer of a resistance to the neomycin derivative G418 in combination with the GFP sequence (Odoardi et al., 2012). Moreover, the same vector was used to transfer a puromycin resistance together with the NFAT regulatory subunit and YFP sequence (Flügel et al., 1999; Lodygin et al., in press).

Before co-culturing with primary T cells, packaging cells were cultured in selection medium (T cell medium (TCM) containing 10 % of foetal bovine serum (FBS) and G418 (0.4 mg/ml) or puromycin (2 μg/ml) depending on the resistance of the cells) in 10 ml cell culture dishes. The cells were kept under 5 % CO_2 humidified atmosphere in an incubator at 37 °C. During cell culture the adhesive packaging cells form monolayers. Upon reaching a confluence of 70-80 % the packaging cell lines were splitted. For that purpose the cells were washed once with 1x PBS and then incubated for 3-5 min with the endopeptidase trypsin (10x stock solution diluted 1:10 with PBS). After detachment of the cells from the cell dish the digestion process by trypsin was stopped by adding medium containing 10 % FBS. The desired amount of cells was taken and centrifuged to remove trypsin residues. After a centrifugation for 8 min with 1200 rpm at 4 °C the supernatant was discarded and the pellet was resolved in TCM containing 10 % of FBS and 0.1 mg/ml G418 or 2 μg/ml puromycin according to cell line. Before co-culturing with primary T cells, the packaging cells were cultured for 2 days without any specific selection agent until a confluence of 70 % was reached. For cryo-conservation and thawing of packaging cells the same media and protocols as described for T cell culture were used (see below 2.2.3.2.).

2.2.3.2 Primary rat T cell culture

T cells retrovirally engineered to express fluorescent proteins and reactive against MBP or β-synuclein peptide$_{93\text{-}111}$ (T_{MBP} or $T_{\beta Syn}$) were generated as reported (Flügel et al., 1999). The primary T cell culture work described here was performed under a laminar flow. The cells were kept under 10 % CO_2 humidified atmosphere at 37 °C.

For establishing antigen-specific $CD4^+$ T cell lines, cells of the draining lymph nodes (popliteal, inguinal and paraaortal LNs) of immunized animals (see chapter 2.2.2.) were isolated in the preclinical phase of the disease at day 10 after immunization with MBP or at day 10-12 after immunization with βSyn. The isolated LNs were minced under and separated through a metal mesh. The cell suspension then was centrifuged (1200 rpm, 8 min, 4 °C) and the cell pellet was washed once with Eagles HEPES (EH) medium. Subsequently,

lymphocytes were adjusted to 2 x 10^6 per ml and co-cultured with 1.5 x 10^5 per ml packaging cells. The cells were kept in a total volume of 100 µl re-stimulation medium (RM) in U-bottom 96-well plates containing 10 µg/ml of MBP or 8µg/ml of βSyn.

Two days after the start of the primary cell culture, T cell growth medium (TCGM) was added (50 µl per well). TCGM contains the supernatant of murine splenocytes stimulated with the mitogen Concanvalin A (ConA supernatant). ConA supernatant contains the growth factor IL-2 which induces the proliferation of T cells in culture. At day 3 or 4 of primary cell culture 50 µl of medium per well were removed and cells were transferred into flat bottom 96-well plates. After the transfer 100 µl fresh TCGM containing G418 (0.4 mg/ml) or puromycin (1 µg/ml) were added per well. Negative selection with G418 or puromycin was maintained for 10 days.

The first stimulation of T cells was performed 7 days after start of the culture. Firstly, 100 µl medium per well were removed and subsequently 1.4 x 10^6 irradiated thymocytes in 100 µl RM were added per well in the presence of the βSyn peptide (8 µg/ml) or the MBP protein (10 µg/ml). The irradiation dose for the thymocytes (that were used as APCs) was 30 gray (Gy).

Two days after re-stimulation 50 µl TCGM were added in each well to propagate T cell proliferation. Three to four days after re-stimulation the T cell wells with the best viral transduction rate (measured by GFP or YFP fluorescence intensity and the best growth capacity of the cells) were chosen and pooled into 60 mm dishes.

2.2.3.3 Re-stimulation of T cells

In the further propagation cycles T cells were re-stimulated in 60 mm dishes in a weekly rhythm. For this purpose 3.5 x 10^6 resting T cells were co-cultured with 70 x 10^6 irradiated thymocytes (30 Gy) per dish in RM containing the appropriate concentration of the antigen (10 µg/ml for MBP and 8 µg/ml for βSyn). At day 2 after re-stimulation TCGM was added to the T cell culture to promote further proliferation. To maintain optimal density T cells were transferred into 10 cm culture dishes and splitted further when necessary. MBP-specific T cell lines expressing GFP were called $T_{MBP\text{-}GFP}$ cells and βSyn-specific T cell clones expressing GFP were named $T_{\beta Syn\text{-}GFP}$ cells in short. MBP- or βSyn-specific T cells expressing NFAT and YFP were named $T_{MBP\text{-}NFAT\text{-}YFP}$ or $T_{\beta Syn\text{-}NFAT\text{-}YFP}$.

2.2.3.4 Cryo-conservation of T cells

For cryo-conservation 10-30 x 10^6 T cells were re-suspended in 1 ml freezing medium 2 or 6 days after exposure to the cognate antigen and aliquoted in cryotubes. The tubes were transferred to precooled (4 °C) cryo-conservation freezing containers and subsequently frozen at -80 °C. For long-term storage T cells were transferred into liquid nitrogen.

2.2.3.5 Thawing of cryo-conserved T cells

In order to thaw cryo-conserved T cells, the cells were taken out of the liquid nitrogen and the freezing tubes were directly incubated in a 37 °C water bath. The cell suspension was then diluted 1:10 in thawing medium (containing 10 % FBS in EH) and washed once. The cells were then either immediately transferred in Lewis rat (when frozen on day 2) or cultured in TCGM medium for further propagation (when frozen on day 4-6).

2.2.3.6 Characterization of established primary T cell lines

Each established T cell line was characterized for phenotype and antigen specificity *in vitro*. Afterwards the pathogenicity of these lines was tested by transfer into Lewis rats (see chapter 2.2.4).

2.2.3.6.1 Characterization of T cell line phenotype by staining of surface markers

$T_{MBP\text{-}GFP}$ and $T_{\beta Syn\text{-}GFP}$ cells were analysed for the expression of the cell surface markers TCR, CD4, CD8, and the activation markers OX40 and IL-2R on day 2 or on day 7 after stimulation with the cognate antigen.

First, cells were transferred into 96- well plates with V shaped well bottom and subsequently the plates were centrifuged. Every centrifugation step in this chapter is performed at 4 °C for 3 min with 1.200 rpm. The supernatant was discarded and the cell pellets were washed once with 1x PBS and once with 1x PBS containing 5 % rat serum (RS). The supernatant was then removed and the T cells were stained with mouse anti-rat CD4, CD8, IL-2R, OX40, TCR primary antibody (1 µg in 100 µl each) in 1x PBS containing 5 % RS. As a control for cross-reactivity of the secondary antibody T cells in one well were incubated without the primary antibody. After an incubation of 30 min on ice, the cell pellets were washed twice. Afterwards, cell bound primary antibodies were detected with an APC-conjugated goat anti-mouse IgG secondary antibody (1 µg in 250 µl) in 1x PBS containing 5 % RS. After an

incubation time of 45 min on ice cells were washed once with 1 x PBS containing 5 % RS and once with 1x PBS. Subsequently, cells were pelleted by centrifugation and the supernatant was discarded. The T cell pellets were then re-suspended in 1x PBS and analysed using a BD FACS Calibur flow cytometer. The instrument is equipped with a 488 nm and a 635 nm laser for the detection of the GFP and the APC signal respectively. Data were analysed by using FlowJo V10 software.

2.2.3.6.2 Characterisation of T cell line specificity via proliferation assay

Each established T cell line was tested *in vitro* for antigen specificity by ^{3}H-thymidine proliferation assay. First, MBP- or βSyn-specific T cells were re-stimulated in 96-well flat bottom plates. For this purpose, 5 x 10^4 day 6 or day 7 T cells were seeded with 1 x 10^6 irradiated thymocytes (30 Gy) and 10 µg/ml or 8 µg/ml of the cognate antigen MBP or β-synuclein, in 100 µl RM per well. As a positive control, T cells were incubated with thymocytes and 1.25 µg/ml of ConA. T cells incubated with thymocytes and the chicken egg protein ovalbumin (OVA) (10 µg/ml) or without any antigen were used as negative controls. All of these T cell-antigen combinations were plated at least in triplicates. T cells were incubated at 37 °C and 10 % CO_2 humidified air in an incubator. 1.5-2 days after stimulation 20 µl (37 MBq/ml) of radioactive methyl-^{3}H-thymidine was added to each well. The cells were further incubated for 10-12 h before harvesting them on a filter membrane. The amount of radioactivity was then measured by a beta-counter and expressed as counts per minute (cpm).

2.2.4 Passive transfer EAE

Passive transfer EAE (ptEAE) was induced by rats' tail vein injection of 5 x 10^6 activated, encephalitogenic T cell blasts (day 2 after stimulation) in 1 ml of EH medium. The body weight of the animals was determined over the whole experimental period and animals were observed for disease symptoms and behavioural abnormalities. Clinical signs of classical EAE were measured by daily scoring of the animals as previously described (chapter 2.2.2). Animals were additionally examined for uncommon disease signs like front limb weakness/paralysis, ataxia or hemiparesis. Animals showing uncommon EAE signs were photographed and filmed to document their symptoms.

2.2.5 Animal preparation and organ processing

Rats were sacrificed at time points of interest after induction of ptEAE by CO_2 inhalation. The animal abdomen and chest were cut open from the ventral body side. Blood was collected directly from the heart of the animal with the help of a syringe prefilled with 300 µl 80 mM ethylenediaminetetraacetic acid (EDTA) and kept at RT until further processing. Afterwards, the lung and spleen were isolated. The animal was then inverted in order to access the dorsal side of the body. The skin above the vertebral column and the skull was removed. Subsequently, the vertebral column was dissected and cut open from the ventral side. The exposed spinal cord (SC) was removed from the column and cut into small pieces. With the help of fine forceps the meninges were stripped off and kept separately from the SC tissue. The skull of the animal was cut stepwise from the occipital bone in rostral direction until the frontal bone was reached. Afterwards, the skull was removed from the brain using strong forceps. Finally, the brain was detached from residual bone of the skull and the cerebellum was cut off. Both brain hemispheres were separated and the meninges were stripped from the brain parenchyma. All dissected organs were kept in EH medium on ice.
In order to measure the number of infiltrated T cells in organs of interest, the different tissues were first weighed and then further processed as described below.

Spleen. A single cell suspension was prepared by mashing the organ through a metal grid in EH medium. After centrifugation with 1200 rpm for 8 min at 4 °C the splenocytic cell pellet was dissolved and incubated for 3 min in 4 ml of ACK buffer on ice in order to lyse the erythrocytes. After dilution of the lysate with 45 ml of ice-cold 1x PBS the sample was pelleted by 8 min of centrifugation with 1200 rpm at 4 °C. The cell pellet was re-suspended in 20 ml TCM and plated in 10 cm cell culture dishes to allow attachment of the macrophages to the dish bottom. Subsequently, the cells were incubated at 37 °C and 10 % CO_2 humidified air in an incubator. After 1 h of incubation, the remaining non-adherent cells (including the T cells) were collected and centrifuged with 1200 rpm for 8 min at 4 °C. The cell pellet was re-suspended in 5 ml of EH medium for further analysis.

Blood. The EDTA-containing blood sample was diluted with an equal amount of 1x PBS (at RT). Afterwards, the blood mixture was gently stacked above a layer of 2 ml lymphocyte separation medium “LSM 1077” (RT) in a 50 ml falcon tube. In order to separate the lymphocytes from other blood components, the blood sample was centrifuged with 2000 rpm for 30 min at RT with minimal acceleration. Subsequently, the lymphocyte interphase was

collected and transferred into a new falcon tube. After washing with 1x PBS, the cells were re-suspended in 1 ml EH medium.

Lung. The lung was mashed extensively with a tissue chopper and subsequently incubated with 300 µl of 0.3 % collagenase and 150 µl of 1x PBS for 1 h at 37 °C under constant shaking. Subsequently, the lung tissue was forced through a metal grid and the cell suspension was collected in a falcon tube containing 10 ml EH medium. After centrifugation with 1200 rpm for 8 min at 4 °C the cell pellet was re-suspended in 1 ml EH medium.

CNS meninges and parenchyma. The parenchyma and meninges of the CNS were kept separately, mashed through a metal grid and suspended in 25 ml of cold EH medium. For gene expression analysis by quantitative real-time polymerase chain reaction (QRT-PCR) (see chapter 2.2.6) on total CNS tissue, a part of the cell suspension was separated, centrifuged and the pellet was re-suspended and stored in Qiazol reagent at -80 °C. The other part of the cell suspension was collected in a 50 ml falcon tube and mixed with 10 ml of Isotonic Percoll (Isopercoll). Afterwards, 10 ml of Underlay Percoll were gently pipetted under the cell suspension/Isopercoll layer and afterwards the tubes were centrifuged with 2780 rpm for 30 min at RT with minimal acceleration/deceleration. The interphase of the sample was collected with a syringe and transferred to a fresh 50 ml falcon tube. The tube was filled up to 50 ml with 1x PBS in order to wash the cells and to dilute the remaining Percoll solution. After centrifugation for 8 min with 1200 rpm at 4 °C the supernatant was discarded and the lymphocyte-containing pellet was re-suspended in 1 ml EH medium for further analysis.
If the lymphocytes from CNS parenchyma or meninges were destined to be further analysed in a cell migration assay, an OptiPrep gradient instead of a Percoll gradient was used to extract the lymphocytes. The different CNS compartments were mashed through a metal grid as described before. In the case of the meninges, the obtained cell suspension (10 ml in EH medium) was mixed with 2.3 ml OptiPrep solution in a 15 ml falcon. The parenchymal cells however, were solved in 20 ml EH medium and the suspension was added to 4.6 ml OptiPrep in a 50 ml falcon tube. Both solutions were mixed shortly. Subsequently, meningeal and parenchymal cell suspensions were centrifuged with 750 rpm for 30 min at RT with minimal acceleration/deceleration. After centrifugation the supernatant was discarded and the pellet was washed and solved in 1x PBS. Afterwards, the cell suspension was centrifuged for 8 min with 1200 rpm at 4 °C and the remaining supernatant was discarded. The cell pellet was re-suspended in 1 ml EH medium and used for T cell transmigration assays (see chapter 2.2.7).

After organ-dependent lymphocyte enrichment, the resulting cell suspensions were used for quantitative analysis of infiltrated $T_{MBP\text{-}GFP}$ or $T_{\beta Syn\text{-}GFP}$ cells. Alternatively, effector T cells were sorted by FACS for gene expression profile studies.

For the quantitative analysis of infiltrated $T_{MBP\text{-}GFP}$ or $T_{\beta Syn\text{-}GFP}$ cells during EAE, a defined volume of the cell suspension of blood, lung, spleen and CNS was mixed with a defined number of BD Calibrite 3 APC beads. These cell-bead samples were analysed via BD FACS Calibur. The T cell number in every analysed sample was calculated by multiplying the number of detected cells with the ratio of supplemented beads to detected beads. To calculate the total number of T_{GFP} cells in the entire cell suspension, the number of T cells in the analysed sample was multiplied with the ratio of the total suspension volume to sample volume. For further calculation of the number of GFP-positive T cells per organ, the calculated total number of T cells was normalized to the weight of the corresponding organ or to the blood volume.

For *ex vivo* analysis of gene expression at single cell level, $T_{MBP\text{-}GFP}$ or $T_{\beta Syn\text{-}GFP}$ cells from different organs of EAE-affected animals were purified as described above. After the final centrifugation step the T cell pellet was re-suspended in 500 µl EH medium, containing 25 µl of 80 mM EDTA. The cell suspension was then filtered through a Cell Strainer mesh. Afterwards, GFP-positive T cells were sorted using a BD FACS Aria. After sorting, the GFP-positive T cells were re-analysed for purity: only samples with ≥ 90 % purity were used for gene expression analysis. The sorted GFP-positive MBP- or βSyn-specific T cells were then pelleted by centrifugation (8 min, 1200 rpm, 4 °C) and re-suspended in 75 µl or 350 µl of β-mercaptoethanol-RLT lysis buffer mixture, depending on the absolute number of sorted cells (see chapter 2.2.6.2. for further details).

2.2.6 Quantitative real-time polymerase chain reaction (QRT-PCR)

In order to analyse the expression level of specific genes of interest in total CNS tissue or in single T cells via QRT-PCR, the ribonucleic acid (RNA) was extracted from tissue samples and transcribed into complementary deoxyribonucleic acid (cDNA) as described below.

2.2.6.1 Isolation of RNA using Quiazol® Lysis Reagent

Due to the sensitive nature of RNA the whole RNA extraction procedure was performed on ice. Homogenized tissue samples of brain meninges, SC meninges, brain or SC, were centrifuged and re-suspended in 1 ml Quiazol Reagent by repetitive pipetting, which induced cell lysis. Subsequently, the samples were stored at -80 °C or directly centrifuged at 12.000 x g for 10 min at 4 °C to remove the insoluble material from the homogenate. The pellet contained cell membrane debris and high molecular weight DNA. The supernatant, which contained the RNA, was transferred to a fresh tube. After this the samples were incubated for 10 min at RT to allow the complete dissociation of nucleoprotein complexes. Subsequently, 0.2 ml of chloroform were added and samples were mixed by hand for 15 sec and again incubated 10 min at RT. Afterwards, the samples were centrifuged at 4 °C and 12.000 x g for 15 min. Following centrifugation the samples were separated into a lower phenol-chloroform phase, an interphase, and an upper aqueous phase which contained the RNA. After the transfer of the upper phase into a fresh tube, the RNA was precipitated by mixing the sample with 0.5 ml isopropanol and 1 µl glycogen. After an incubation time of 15 min at RT the samples were centrifuged at 4 °C for 10 min at 12000 x g. The RNA precipitate formed a gel-like pellet on the bottom of the tube so that the supernatant could be easily removed. In order to dissolve the precipitated RNA, the pellet was washed once with 1 ml of 70 % ethanol. The sample was mixed by vortexing and centrifuged at 7.400 x g for 5 min at 4 °C. In a final step the RNA pellet was air-dryed for 5 min and dissolved in 11 µl of RNase-free water. The RNA was stored for shorter periods at -20 °C and for longer periods at -80 °C.

2.2.6.2 Isolation of RNA using RNeasy® Micro or RNeasy® Mini Kit

RNA extraction from sorted $T_{MBP\text{-}GFP}$ or $T_{\beta Syn\text{-}GFP}$ cells was performed using the Qiagen RNeasy ®Mini or RNeasy® Micro Kit following the manufacturer's instructions. The RNeasy Micro Kit was used for 10 x 10 up to 5 x 10^5 sorted cells and the RNeasy® Mini Kit for more than 5 x 10^5 sorted cells. As described above (see chapter 2.2.5), the sorted cells were pelleted and dissolved in 75 or 350 µl of β-mercaptoethanol RLT lysis buffer depending on cell count. The samples were stored at -80 °C or directly mixed by vortexing for 1 min at RT. Afterwards, 1 volume (75 or 350 µl) of 70 % ethanol was added and the solution was mixed by repetitive pipetting to homogenize the lysate. Subsequently, the samples were applied to an RNeasy micro or mini column placed in a collection tube and centrifuged at RT for 15 sec at 11000 x g. The RNeasy column silica-membrane removes most of the DNA of the samples.

The flow-through of the columns was discarded and 350 µl of RW1 Buffer were pipetted onto the columns. Following centrifugation at RT for 15 sec at 11000 x g the flow-through was again discarded. For the preparation of the DNase incubation mix, 10 µl DNase stock solution (RNase-Free DNase Set) were added to 70 µl of RDD Buffer (RNase-Free DNase Set) per sample and inverted gently by hand. In order to completely remove remaining DNA in the samples, 80 µl of DNase incubation mix were added to each sample column and incubated for 15 min at RT. Afterwards, 350 µl RW1 buffer were added to the sample columns and centrifuged at RT and 11000 x g for 15 sec to wash the columns. After discarding the flow-through the columns were put in fresh collection tubes, 500 µl RPE 1 Buffer were added to the columns and samples were centrifuged for 15 sec at 11000 x g at RT to wash the columns. The flow-through was discarded. Following the RNeasy® Mini Kit protocol a second washing step with RPE 1 Buffer was performed (see first RPE 1 Buffer washing step). When using the RNeasy® Micro Kit 500 µl of 80 % ethanol were pipetted onto the columns. Independent of the kit used, columns were centrifuged for 2 min at 11000 x g at RT, the flow-through was discarded and the columns were put into fresh collection tubes. Following another round of centrifugation, to dry the silica-gel membrane, columns were again transferred to fresh collection tubes. Subsequently, 14 µl RNase-free water were pipetted directly onto the RNeasy silica-gel membrane to elute the RNA. Columns were centrifuged at RT and 11000 x g for 1 min. The elution step was repeated once with the flow-through from the first elution round to increase RNA yield. The RNA was frozen at 20 °C for short periods or -80 °C for longer periods of storage or directly used for cDNA synthesis.

2.2.6.3 Reverse Transcription: cDNA synthesis using the RevertAid™ First Strand cDNA Synthesis Kit

The synthesis of cDNA from RNA was performed with the help of the Fermentas RevertAid™ First Strand cDNA Synthesis Kit following the manufacturer's instructions. For the cDNA synthesis random hexamer primers were used. These primers non-specifically bind to RNA templates and therefore can be used to synthesize cDNA from all possible RNA templates. First all required components of the Kit were thawed, mixed and centrifuged.

Thereafter, 11 µl of sample RNA were pipetted into an RNase-free tube together with 1 µl of random hexamer primers, gently mixed and briefly centrifuged. The RNA-primer mix was then incubated at 65 °C for 5 min and subsequently chilled on ice for 1-2 min. This step denatures the RNA and allows the binding of the primers to the single strands. Afterwards, the RNA-primer mix was centrifuged and placed back on ice. During the RNA-primer mix

incubation the following components were combined: Per RNA sample 4 µl 5x Reaction Buffer, 1 µl RiboLock™ RNase Inhibitor, 2 µl 10mM dNTP Mix and 1 µl RevertAid™ M-MuLV Reverse Transcriptase. This master mix was carefully mixed and 8 µl per sample were transferred to 0.5 ml RNase-free tubes. The RNA-primer mix was added to the 0.5 ml tubes containing the reverse transcriptase mix. The following cDNA synthesis reaction steps were performed using the Eppendorf Mastercycler EP Gradient. First, samples were incubated at 25 °C for 5 min. Thereafter, cDNA synthesis was promoted by 60 min incubation at 42 °C. Finally, the cDNA synthesis was stopped by heat inactivation of the enzyme at 70 °C for 5 min. The cDNA was stored ad -20 °C or directly used for quantitative real-time PCR.

2.2.6.4 Relative quantification of cytokine and chemokine expression via quantitative real-time PCR

Quantitative real-time PCR was used to determine the relative expression level of cytokines, cytokine receptors, chemokines or their receptors and adhesion molecules in total tissues or in single T_{MBP} or $T_{\beta Syn}$ cells during the different EAE phases.

The following rat-specific forward and reverse primers for IFN-γ, IL-17, CCL5, CCR5, CCR6, CCR7, CXCL9, CXCL10, CXCL11, CXCL12, CXCR3, CXCR4, LFA-1 VLA-4 and the house- keeping gene β-actin were designed for use with fluorescently tagged (fluorophore: Fam, quencher: Tamra) probes specific for each gene:

β-actin primer sequences:

Forward primer: 5'- GTA CAA CCT CCT TGC AGC TCC T -3'
Reverse primer: 5'- TTG TCG ACG ACG AGC GC -3'
Probe: 5'-Fam- CGC CAC CAG TTC GCC ATG GAT -Tamra-3'

CCL5 primer sequences:

Forward primer: 5'- CCA CCT TGC AGT CGT CTT TGT C -3'
Reverse primer: 5'- GAT GTA TTC TTG AAC CCA CTT CTT CTC -3'
Probe: 5'-Fam- AGG AAC CGC CAA GTG TGT TGT GCC AAC -Tamra-3'

CCR5 primer sequences:

Forward primer: 5'- GTT CTC CTG TGG ACC GGG TAT AG -3'
Reverse primer: 5'- ATT GTC AAA CGC TTC TGC AAA C -3'

Probe: 5’-Fam- AGC TTA CAC GAT CAG GAT TGA CTT GC -Tamra-3’

CCR6 primer sequences:

Forward primer: 5’- GGC CGG AAC ATT ATT GGA AA -3’
Reverse primer: 5’- TTC CAG AGA CCG AGC CAT G -3’
Probe: 5’-Fam- TGA ATT TCA CCG AGG CCA ACT ACG GA-Tamra-

CCR7 primer sequences:

Forward primer: 5’- GTG TAG TCC ACG GTG GTG TTC TC-3’
Reverse primer: 5’- CTG GTC ATT TCC AGG TGT GCT -3’
Probe: 5’-Fam- CCG ATG TAG TCG TCT GTG A -Tamra-3’

CXCL9 primer sequences:

Forward primer: 5’- TTG CCC CAA GCC CTA ACT G -3’
Reverse primer: 5’- ACC CTT GCT GAA TCT GGG TCT AG -3’
Probe: 5’-Fam- CAT CGC TAC ACT GAA GAA CGG AGA TC -Tamra-3’

CXCL10 primer sequences:

Forward primer: 5’- CGT GCT GCT GAG TCT GAG T -3’
Reverse primer: 5’- GTC TCA GCG GCT GTT CAT -3’
Probe: 5’-Fam- CTC AAG GGA TCC CTC TCG CAA GAA C -Tamra-3’

CXCL11 primer sequences:

Forward primer: 5’- GGT TCC AGG CTT CGT TAT GTT C -3’
Reverse primer: 5’- ACC TTC CTT GAT TGC TGC CAT T -3’
Probe: 5’-Fam- CTG TCT TTG CAT CGA CCG CGG AGT -Tamra-3’

CXCL12 primer sequences:

Forward primer: 5’- GTC AAA CAT CTG AAA ATC CTC AAC AC -3’
Reverse primer: 5’- GGT CAA TGC ACA CTT GTC TGT TGT -3’
Probe: 5’-Fam- ACT GTG CCC TTC AGA TTG TTG CAA GGC T -Tamra-3’

CXCR3 primer sequences:

Forward primer: 5’- AGC AGC CAA GCC ATG TAC CTT -3’
Reverse primer: 5’- TAG GGA GAT GTG CTG TTT TCC A -3’
Probe: 5’-Fam- AGG TCA GTG AAC GTC AAG TGC TAG ATG -Tamra-3’

CXCR4 primer sequences:

Forward primer: 5’- GGA GGT CAT CAA GCA AGG ATG T -3’
Reverse primer: 5’- GGG TTC AGG CAA CAG TGG AA -3’
Probe: 5’-Fam- TTC GAG AGC GTC GTG CAC AAG TGG -Tamra-3’

IFN-γ primer sequences:

Forward primer: 5’- AAC AGT AAA GCA AAA AAG GAT GCA TT -3’
Reverse primer: 5’- TTC ATT GAC AGC TTT GTG CTG G -3’
Probe: 5’-Fam- CGC CAA GTT CGA GGT GAA CAA CCC -Tamra-3’

IL-17 primer sequences:

Forward primer: 5’- GAG TCC CCG GAG AAT TCC AT -3’
Reverse primer: 5’- GAG TAC CGC TGC CTT CAC TGT -3’
Probe: 5’-Fam- ATG TGC CTG ATG CTG TT -Tamra-3’

LFA-1 primer sequences:

Forward primer: 5’- CTG CTA CTC ATC CTA GCT GGA CTA CTC -3’
Reverse primer: 5’- GCA GTT GCT GAC TTT GTA CTT GGT -3’
Probe: 5’-Fam- TCC TGG GAT CTG CCC TGT CC - Tamra-3’

VLA-4 primer sequences:

Forward primer: 5’- GAA GGA AGA GTG TTC GTG TCA ATC A -3’
Reverse primer: 5’- CGA CGA GCA CTC TTT TCC ATT -3’
Probe: 5’-Fam- TCT GGC ATG GGA GCT GTG ATG GTT -Tamra-3’

The primermixes for every primer pair were prepared for each gene of interest separately (table 1) and subsequently combined with a commercially available ready-to-use qPCR mastermix (qPCR Mastermix, Eurogentec) as illustrated in table 2.2.1.

Table 2.2.1 Composition of primermixes

CCL5/CCR 5/ CCR6/CXCL9/CXCL10/ CXCL11/ CXCL12/ CXCR3/ CXCR4/ IFN-γ / IL-2R / LFA-1/ VLA-4	**Concentration (mM)**
Fwd. primer	300
Rev. primer	300
Fam- Tamra probe	100

β-actin / IL-17	**Concentration (mM)**
Fwd. primer	300
Rev. primer	900
Fam- Tamra probe	100

CCR7	**Concentration (mM)**
Fwd. primer	900
Rev. primer	900
Fam- Tamra probe	100

Table 2.2.2 Reaction batch per well for QRT-PCR

Reagent	Volume
qPCR mastermix	12.5 µl
Primermix	5 µl
cDNA template (1:20 diluted with Aqua dest.)	7.5 µl
Total volume	25 µl

For QRT-PCR analysis, cDNA samples were combined with previously prepared master mixes in 96-well Flat Deck Thermo-Fast detection plates (see table 2.2.2).
The expression of the housekeeping gene, cytokines and chemokines, chemokine receptors and adhesion molecules in the samples of interest were analysed in duplicates using the StepOne^{TM} Software v2.0 and the StepOnePlus Real-Time PCR System (Applied Biosystems).

Table 2.2.3 QRT-PCR cycling conditions

Temperature	Time	Number of cycles
50°C	2 min	1x
95°C	10 min	1x
95°C	15 s	40 x
60°C	1 min	

The Delta-delta Ct method was used for quantification. β-actin was used as house-keeping gene.

2.2.7 T cell chemotactic assay

Directional migration of effector $T_{MBP\text{-}GFP}$ or $T_{\beta Syn\text{-}GFP}$ cells was analysed using a HTS Transwell-96 Well plate (5.0 µm Pore Size Polycarbonate Membrane). T cells were isolated *ex vivo* from blood of Lewis rat one day after T cell transfer (preclinical phase) or from the meninges and the parenchyma of the brain and SC at the peak of disease. T cell enrichment was performed as described before (see chapter 2.2.5). Afterwards, 75 µl of cell suspension in RM were pipetted in the upper chambers of the transwell plate. CCL5, CCL19, CCL20,

CXCL11 and CXCL12 (0.1 ng/ml) were diluted in 235 µl RM and added to the lower chamber. Every sample was tested for every chemokine in duplicate. For normalisation of chemokinetic T cell movement, duplicated wells containing RM without chemokines were used. In order to measure the T cell concentration in the original sample (input), a small portion of the cell suspension was kept on ice for final analysis. The transwell plate was incubated at 37 °C for 5 h under 10 % CO_2 humidified atmosphere in the incubator. The number of effector T cells that had migrated through the membrane was counted by flow cytometry as described above (see chapter 2.2.5) and quantified as a percentage of the input. The migration index was calculated as the ratio of the percentage of input from non-treated to the percentage of input of chemokine-treated migrated T cells.

2.2.8 Apoptosis detection assay

In order to detect the percentage of apoptotic effector T cells in *ex vivo* samples, active Caspase-3 staining was performed according to the following protocol. 100 µl of CNS cell suspension (see chapter 2.2.5) were plated in 96-well V-bottom plates in duplicates. Cells were then fixed by incubating them in 100 µl of 2 % ice-cold PFA for 20 min on ice. After two steps of washing (one with 1x PBS and one with 1x BD Perm/Wash Buffer containing 5 % RS) the cells were permeabilized for 30 min on ice in 1x BD Perm/Wash Buffer containing 5 % of rat serum. Afterwards the samples were centrifuged and the pellet was re-suspended in 100 µl of 1:500 diluted rabbit anti-rat active Caspase-3 primary antibody in 1x BD Perm/Wash Buffer containing 5 % of rat serum. 100 µl of rabbit IgG diluted 1:500 in 1x BD Perm/Wash Buffer containing 5 % of rat serum was used as negative control. Samples were then incubated for 45 min on ice, and then washed two times with 1x BD Perm/Wash Buffer containing 5 % of rat serum. For detection of the primary antibody, samples were incubated for 30 min on ice with a secondary APC-conjugated goat anti-rabbit IgG antibody (dilution of 1:250 in 1x BD Perm/Wash Buffer containing 5 % of rat serum). Subsequently, the cells were washed two times with 1x BD Perm/Wash Buffer containing 5 % of RS and once with 1x PBS and then re-suspended in 1x PBS. The samples were acquired using BD FACS Calibur. Analysis of the percentage of active Caspase-3-positive T cells was performed by using the FlowJo V10 software. To ensure that the active Caspase-3 staining worked properly, apoptosis was induced in cultured $T_{MBP\text{-}GFP}$ or $T_{\beta Syn\text{-}GFP}$ cells by adding the protein synthesis inhibitor puromycin in a concentration of 1 µg/ml. T cells were incubated for 0 (control), 6, 12 and 24 h at 37 °C and 10 % CO_2 humidified air in an incubator. After incubation, the T cells were fixed with 2 % ice-cold PFA for 20 min and stained for FACS analysis according

to the protocol described above. 24 h after apoptosis induction 45-65 % of cultured T cells were detected as active-Caspase 3-positive (data not shown). Therefore the staining method was classified as a sensitive and specific way to label and detect apoptotic cells.

2.2.9 Histology

For the analysis of the invasion pattern of $T_{MBP\text{-}GFP}$ and $T_{\beta Syn\text{-}GFP}$ cells or $T_{MBP\text{-}NAFT\text{-}YFP}$ and $T_{\beta Syn\text{-}NFAT\text{-}YFP}$ cells into the CNS, animals were sacrificed at either onset or peak of the disease and perfused for histology.

2.2.9.1 CNS tissue fixation and processing

Animals were sacrificed by CO_2 inhalation and afterwards fixed dorsally on a polystyrene plate for dissection. The abdomen was opened up with scissors and the peritoneum was cut to access the thorax of the animal without damaging inner organs. Subsequently, the thorax was opened to expose the heart. The apex of the left ventricle was cut and a hollow needle was inserted into the heart and clamped to prevent displacement during procedure. The right atrium was cut to intercept the blood circulation and the blood of the animal was washed out by a constant flow of filtered 1x PBS (4 °C) pumped into the left ventricle of the heart. Afterwards, the animal was fixed by perfusion with ice-cold 4 % paraformaldehyde (PFA). Then the animal was opened up from the dorsal side and the entire vertebral column was removed. Subsequently, the whole skull of the animal was removed from the skin and connective tissue and the lower jaw was cut off. The vertebral column and the skull were then incubated for 48 h in 4 % paraformaldehyde for post-fixation and afterwards transferred to decalcification solution containing the calcium chelator EDTA. The chelator binds calcium ions of the calcium phosphate within the bone and thereby softens its structure. The decalcification solution was renewed weekly. After 2-3 weeks of incubation at 4 °C, the bone was soft enough for cryo-sectioning. At this time point, the tissue was transferred to 30 % sucrose solution and stored at least for 72 h for dehydration. Thereafter, the tissue was embedded in Tissue TeK cryo matrix for cryo-sectioning.

2.2.9.2 Cryo-sectioning

Histological cryo-sectioning was performed with a Leica CM3050 S Cryostat with a chamber temperature of -24 °C. The embedded, decalcified vertebral column was cut transversely into

14 µm thick sections, whereas the decalcified skull was cut into 14 µm thick coronal sections. Brain and SC slices were immediately transferred to Superfrost glass slides and dried at 37 °C on a heating plate. After drying the sections were stored at -20 °C or directly used for staining or embedded for histological analysis.

2.2.9.3 Staining of cell nuclei and embedding

The brain and SC sections were re-hydrated with 1x PBS and afterwards post-fixed with 4 % PFA (4 °C) for 10 minutes. Afterwards the sections were washed with 1x PBS, embedded in FlouromountG and covered by coverslips. Cultured $T_{MBP\text{-}NFAT\text{-}YFP}$ or $T_{\beta Syn\text{-}NFAT\text{-}YFP}$ cells were spun onto glass slides with the help of a cytospin centrifuge. Brain and SC sections of $T_{MBP\text{-}NFAT\text{-}YFP}$ or $T_{\beta Syn\text{-}NFAT\text{-}YFP}$ animals or the cultured cells themselves were stained with 4`,6-diamidino-2-phenylindole (DAPI) after rehydration, post-fixation and washing of the material with 1x PBS, to visualize the nuclei of the cells. Firstly, sections were incubated for 10 min with 1 µg/ml DAPI in 1x PBS at RT. Afterwards, glass slides with the tissue sections or cultured cells were washed extensively with 1x PBS and covered as described before.

2.2.10 Labelling of leptomeningeal APCs by intrathecal injection

The intrathecal injection of Dextran Texas Red was performed in order to stain meningeal phagocytes in the leptomeningeal area of brain and SC. For each rat 0.7 µl of 3.000 MW Dextran Texas Red were dissolved in 20 µl NaCl and carefully drawn up into a tuberculin syringe (with a 27 gauge needle). The animals were anaesthetized by intraperitoneal (i.p.) injection of 1 µl/g body weight Ketamine/Xylariem solution (mixture 1:1.5). The animals were fixated in a stereotactical device and the syringe containing the dextran was placed into a stereotactical holder at 90 degree to the body surface. The injection of the dye was performed into the cisterna magna between the occipital bone and the atlas at a depth of 3.5 mm. The dye was injected in two steps of 10 µl each with an interval of 1 min between single injections. Afterwards, the needle was left in its position for additional 5 min to ensure that the injected liquid was taken up by the liquor. Subsequently, the needle was gently removed and the animal was put into a separate cage until complete recovery. Moreover, during this time the animal was kept warm.

2.2.11 Intravital live imaging with the two-photon laser scanning microscope

Two-photon laser scanning microscopy (2P-LSM) was used for imaging $T_{MBP\text{-}GFP}$ or $T_{\beta Syn\text{-}GFP}$ motility patterns within CNS meningeal compartments in living animals. In order to access the dorsal spinal cord meninges the well-established "open spine window" procedure was performed as previously described (Bartholomäus et al., 2009). This preparation gives equivalent results to the "closed SC" preparation (Bartholomäus et al., 2009). To access the parietal cortex meninges however, thinned skull as well as open skull window preparations were established and compared.

2.2.11.1 Animal preparation for intravital live imaging

Animals were initially anaesthetised with a mixture of 1:1.5 Ketamine/Xylariem injected subcutaneously or intraperitoneally. Afterwards, animals were tracheally intubated and ventilated with 1.5-2 % isoflurane. If necessary an additional intramuscular injection of 1:1.5 mixture of Ketamine/Xylariem was applied. The body temperature of the animal was measured with the help of a rectal probe and kept at a constant physiological level via a custom-made heating plate installed into the imaging stage. Electrocardiogram (ECG) was registered by epicutaneous electrodes during the entire imaging session. The animal was hydrated with saline via an intravenous catheter, which was additionally used for the injection of Dextran Texas Red to label the meningeal vessels during imaging. Depending on the site of investigation (spinal cord or brain) different surgical procedures were used to expose the tissue of interest.

For imaging of the SC the dorsal fur was shaven and the underlying skin was disinfected with 70 % ethanol. Subsequently, a midline skin incision of 2-3 cm above the end the thoracic and the beginning of lumbar vertebral column was performed. The paravertebral musculature was detached from the spine and the animal was stereotactically fixed onto the imaging stage. Afterwards, an agarose ring was applied above the vertebral body at the level where the laminectomy should be performed to keep the saline solution on top of the meningeal tissue during the imaging session. In order to get access to the SC, a vertebral window was generated by a laminectomy at the level Th12 / L1. Afterwards the dura mater was carefully removed with fine forceps and the agar ring was filled with saline. Finally, the imaging stage was positioned under the 2P-LSM equipped with a 20x water immersion objective (numerical aperture: 0.95).

For imaging the brain meninges, the scalp of the animal was disinfected with 70 % ethanol. Afterwards, a midline scalp incision was performed extending from the neck region between the ears to the frontal portion of the head where the eyes are located. The animal was then stereotactically fixed onto a custom-made imaging stage. The connective tissue attached to the skull was carefully removed with a cotton bud. Subsequently, a high-speed micro-drill with a prophyclean dental drill tip was used to thin a circular area of the skull between the coronal, transverse and sagittal suture with medium drilling speed (see fig. 2.1). To avoid friction-induced heating of the skull and underlying tissues, short periods of drilling were followed by resting intervals. During these intervals saline solution was applied to additionally cool-down and clean the drilling surface. Moreover, during the thinning of the skull the applied pressure to the bone had to be minimised to avoid pushing the skull against the brain surface. However, due to the fact that a certain pressure is needed for successful thinning of the skull, it was helpful to keep the thinned region as small as possible. For imaging through the thinned skull window it is important that a uniform thickness of the skull is achieved. Irregular thickness may cause significant spherical aberration. The consequence is a reduced two-photon excitation and optical distortion of underlying structures (Helm et al., 2009). After the flattening of the skull the imaging area was cleaned carefully with saline and an agarose ring was created to keep saline within the imaging area.

For imaging through an open skull window, thinning of the skull was performed as described above. However, the outermost ring-like border of the thinned region was continuously thinned until the flattened skull area detached from the skull. Subsequently, the flattened bone fragment was carefully removed with fine forceps while keeping contact to the underlying dura mater at a minimum. Similar to the thinned skull preparation an agarose ring was created around the imaging field. Afterwards, the dura mater was covered with saline and the fixed animal was positioned under the 2P-LSM. Both the preparations could be performed in around 30 minutes.

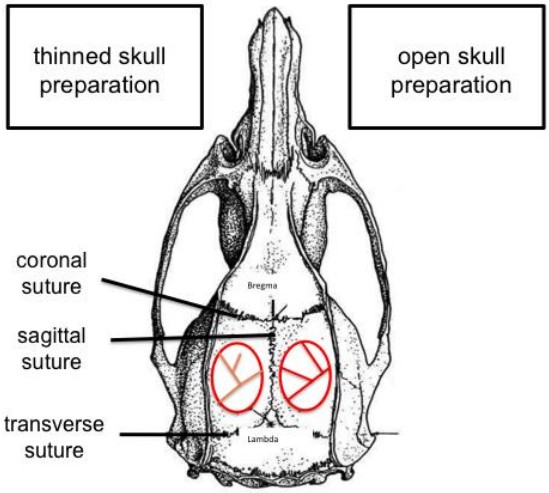

Figure 2.1 Skull preparation for intravital live imaging. The picture shows the areas at which the skull windows were established (between the coronal, transverse and sagittal sutures). For the thinned skull window, the skull was thinned and the imaging of the cortical meninges was performed through the bone. For the open skull window the bone was completely removed at the indicated area. The dura mater was left intact. To compare both skull windows the preparations were performed on the same animal at both sides of the sagittal suture. Adapted from (Paxinos and Watson, 2007).

2.2.11.2 Two-photon laser scanning microscopy

Two photon laser scanning microscopy was performed using a Zeiss Laser Scanning Microscope 710 combined with a Coherent 10 W Ti:Sapphire chameleon laser. Blood vessels were labelled by injection of 2000000 MW dextran tetramethylrhodamine. Meningeal phagocytes were labelled by intrathecal injection of 3000 MW Dextran Texas Red (see chapter 2.2.10). For the excitation of fluorophores a pulsed laser adjusted to a wavelength of 880 nm was used. The emitted fluorescence was detected by non-descanned detectors equipped with 525 ± 50 and 630 ± 69 nm band-pass filters. In general, imaging of the parietal cortex (open skull window) and of the dorsal SC meninges was performed with 28 % or 22 % of the laser power, respectively. For imaging of deeper brain parenchyma or for the acquisition of 3D tile scans overview images, a laser intensity of 50-60 % or 40 % was used, respectively. For 3D time-lapse movies, scanning intervals of 32 sec and 58 cycles were used. After completion of the imaging session the animals were sacrificed. The brain and SC tissue were used for further histological analysis.

2.2.11.3 Analysis of time-lapse videos, single Z-stacks and overview pictures generated by TPM

Acquired 3D time-lapse videos were analysed with the help of the Imaris 7.1.1 software. In a first step, the automatic cell tracking function was used. Afterwards, the automatically generated T cell tracks were evaluated and corrected manually. The number of intraluminally rolling or crawling cells was counted manually. Subsequently, the percentage of rolling and crawling cells was calculated. The track properties of intraluminal and extravasated crawling T cells were exported to Microsoft Excel 2010 for further analysis. For the analysis of motile extravasated cells, tracks with a duration lower than 8 min and stationary cells were excluded. The generation of graphs and statistical tests was performed using Graphpad 5.0.4 software. Statistical analysis was performed using the two-tailed t-test (Mann-Whitney test) or one-way ANOVA (Kurskal-Wallis) test with confidence intervals of *P < 0.05, **P < 0.01, ***P < 0.001, ****P < 0.

Single z-stacks or overview image files acquired with the TPM were exported as maximum intensity projections in TIF format by using the Zen 2009 software. The TIF files were loaded in Adobe Photoshop CS5 software and the images were corrected in tones and contrast for the different channels using the curve function. Moreover, three dimensional z-stacks or overviews of the imaging field were exported into Imaris 7.1.1 software to construct three-dimensional pictures of the imaging area and to analyse imaging- or T cell-infiltration depth.

2.2.12 Fluorescence Microscopy

In order to visualize and subsequently analyse the invasion pattern of $T_{MBP\text{-}GFP}$ or $T_{\beta Syn\text{-}GFP}$ cells into the CNS, animals were sacrificed at onset and peak of EAE and prepared for histological analysis (see chapter 2.2.9). Overview pictures of brain and SC were acquired by a Zeiss Axio Observer Fluorescence Microscope equipped with a Zeiss Plan Apochromat 10x Air Objective (with a numerical aperture of 0.45). The light source was an HXP 120C metal halide lamp. Fluorescence emission was detected using a Zeiss AxioCam HSM. An excitation at 470 nm and emission at 509 nm was used for the detection of the green fluorescent $T_{MBP\text{-}GFP}$ or $T_{\beta Syn\text{-}GFP}$ cells. For the red channel, excitation and emission were 558 nm and 583 nm, respectively. The exposure time was 600-700 ms for each channel. Overviews were acquired with the help of the Zeiss Axiovsion V 4.8 software and the MosaiX and focus correction function, which allow the automatic construction of an overview on the basis of single pictures and pre-defined focus points. The resulting overview pictures were exported as TIF

files, loaded into Adobe Photoshop CS5 software and corrected in tones and contrast for the different channels using the curves function. For the analysis of translocation events of DAPI-stained $T_{MBP\text{-}NFAT\text{-}YFP}$ or $T_{\beta Syn\text{-}NFAT\text{-}YFP}$ cells at different time points during EAE in brain and SC sections, fluorescence emission was detected through a Zeiss Plan Apochromat 40x water emulsion objective (with a numerical aperture of 0.95). Fluorescence within the yellow spectrum was acquired with excitation at 514 nm, emission at 527 nm and an exposure time of 600-700 ms. The blue DAPI signal was acquired by 350 nm excitation and detected at 470 nm with an exposure time of 10 ms. The analysed areas of brain and SC were acquired with the help of the Zeiss Axiovision V 4.8 software and the MosaiX and z-stack function. These functions allow scanning of the tissue pseudoconfocally in the z-axis. Single z-stacks were then "stitched" together automatically. Each plane of the acquired z-stack of a mosaic was then analysed for translocation events. T cells with nuclear or cytosolic NFAT reporter were counted manually and the percentage of translocation events was calculated.

3. Results

3.1 Disease course of aEAE induced with the WM antigen MBP or the GM antigen βSyn.

In order to compare the pathogenic potential of the myelin antigen myelin basic protein (MBP) and the neuronal antigen β-Synclein$_{93\text{-}111}$ peptide (βSyn) in inducing EAE, Lewis rats were actively immunized. As expected, animals immunized with MBP showed the classical disease progression. The disease started at day 9 post immunization with loss of body weight (BWL) and flaccid paralysis of the tail tip. At the peak of the disease (day 12 after immunization) the animals' hind limbs were paralysed and the front limbs were weak. Three days after the peak animals recovered from the symptoms (fig. 3.1 A). βSyn-induced aEAE started with a delay compared to MBP-induced aEAE at day 12 post immunization. The animals showed the same EAE symptoms as described for MBP-induced aEAE. However, the disease was in average less severe: even if a part of the animals exhibited complete hind limb paralysis and weakness of front limbs two days after disease onset, the most of them showed only tail paralysis. The animals had recovered completely three days after the peak of disease (fig. 3.1 B). No uncommon EAE symptoms were observed.

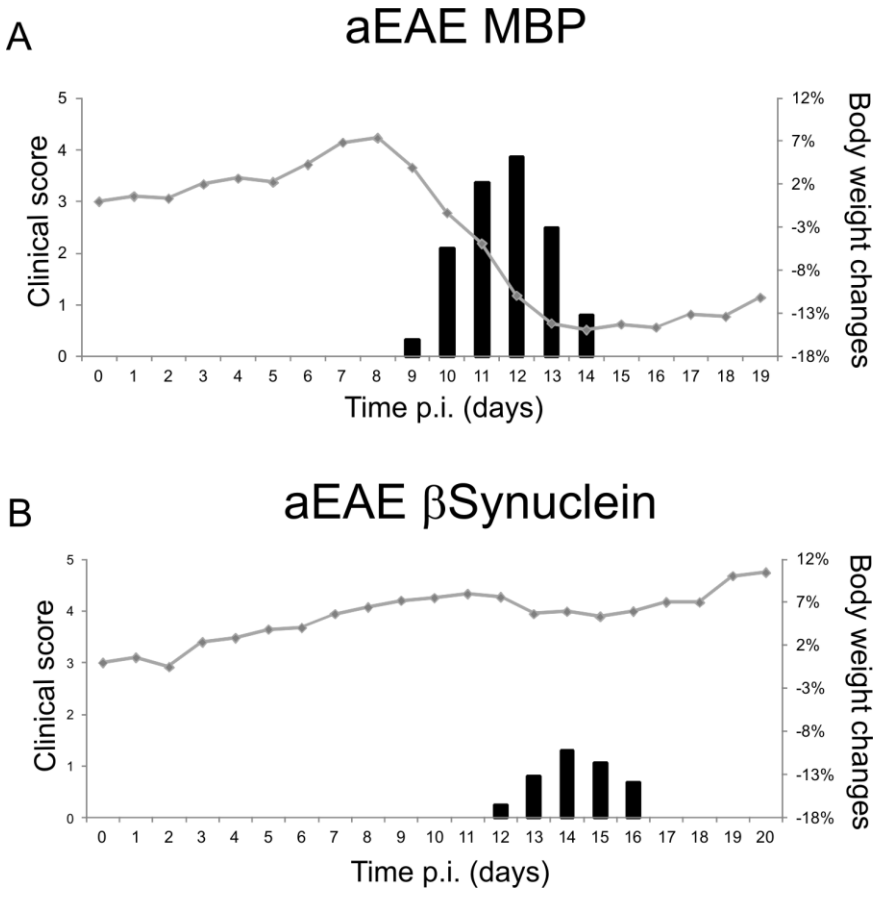

Figure 3.1 Clinical course of aEAE in MBP and βSyn immunized animals. Average body weight changes in per cent (line) and severity of clinical symptoms (bars) of Lewis rats after immunization with the MPB protein **(A)** or the βSyn peptide **(B)** emulsified in Complete Freund`s Adjuvant. The following score system was used: 0, no sign of disease; 0.5, loss of tail tonus; 1, tail paralysis; 2, gait disturbance; 3, hind limb paralysis; 4, tetraparesis and 5, moribund. p.i., post immunization. n = 6 per group. Representative data of 3 independent experiments are shown.

3.2 Establishment and characterisation of $T_{MBP\text{-}GFP}$ and $T_{\beta Syn\text{-}GFP}$ cell lines

EAE is a classical T cell-mediated disease that can be induced by either active immunization or by passive transfer of antigen-specific effector T cells. In order to investigate the specific role of T cells reactive against myelin or neuronal antigens in inducing EAE, T cells reactive against MBP or βSyn were established and tested *in vitro* for their phenotype and antigen specificity and *in vivo* for their pathogenic potential. Of note, the established T cell lines were retrovirally engineered to express GFP because the constant expression of the fluorescent marker allows the detection and quantification of these cells both *in vitro* and *in vivo*. For the phenotype characterisation $T_{MBP\text{-}GFP}$ and $T_{\beta Syn\text{-}GFP}$ cells were stained for the T cell specific surface markers CD4, CD8, TCR and the activation markers OX40 and IL-2R. Both lines showed a similar expression pattern of these markers (fig. 3.2 A and fig. 3.3 A). T cells of both specificities expressed the typical T cell marker TCR and were CD4-positive and CD8-negative (representatively shown here for activated T cell blasts). Two days after re-stimulation the activated T cell blasts show a high expression of the surface activation markers OX40 and IL-2R, which were down-regulated during the resting stage 7 days after re-stimulation (fig. 3.2 A and 3.3 A).

The antigen specificity of each line was tested via ^{3}H-thymidine proliferation assays. The $T_{MBP\text{-}GFP}$ and $T_{\beta Syn\text{-}GFP}$ cells were tested for their proliferative response to different antigens presented by APCs. $T_{MBP\text{-}GFP}$ and $T_{\beta Syn\text{-}GFP}$ cells proliferate specifically after the re-stimulation with their cognate antigen MBP protein or βSyn peptide, respectively (fig. 3.2 B and 3.3 B). Moreover, the proliferative response of $T_{MBP\text{-}GFP}$ and $T_{\beta Syn\text{-}GFP}$ cells to their cognate antigen was similarly strong as the response to Concanavalin A (ConA), which acts as a non-specific stimulator of T cell proliferation (positive control). Both cell lines showed only limited response when cultured with a sham antigen, the chicken egg white protein OVA or without antigen (negative control) (fig 3.2 B and 3.3 B).

Next the pathogenic potential of $T_{MBP\text{-}GFP}$ and $T_{\beta Syn\text{-}GFP}$ cells was tested *in vivo*. The disease was induced by intravenous (i.v.) injection of the T cells into the rat-tail and the animals were

subsequently scored on a daily basis according to the EAE scoring system described in fig. 3.1. As expected, animals that received $T_{MBP\text{-}GFP}$ cells developed a classical monophasic paralytic disease. After a preclinical symptom-free phase, animals started to lose body weight and developed a flaccid tail 3 days post transfer (p.t.). At the peak of disease, approximately 5 days p.t., the animals showed complete hind limb paralysis often in combination with weakness or paralysis of the front limbs (fig. 3.2 C and D). Afterwards the animals progressively recovered with complete remission of the symptoms 8 days p.t.. Also the animals that received $T_{\beta Syn\text{-}GFP}$ cells developed a monophasic paralytic disease with an incidence of 89 % (tab. 3.1). In total, 135 animals were analysed (tab. 3.1). Compared to the animals transferred with $T_{MBP\text{-}GFP}$ cells, these animals showed a prolonged preclinical phase (fig. 3.3 C). The onset of disease was between day 4 and day 5 after T cell transfer starting with identical symptoms as animals that were injected with $T_{MBP\text{-}GFP}$ cells (i.e. loss of body weight and paralysis of the tail). The peak of the disease was reached at day 7 post transfer. At this stage the animals showed the same paralytic symptoms as described before for the $T_{MBP\text{-}GFP}$ cell-induced ptEAE. Surprisingly, the animals recovered very rapidly reaching clinical score 0 from clinical EAE score 3-4 (complete hind limb paralysis, fig. 3.3 D left picture) in less than 24 h (fig. 3.3 C). Interestingly, four rats with βSyn-specific ptEAE showed uncommon disease symptoms. One animal suffered from hemiparesis, another animal showed a weakness of the right front limb (fig. 3.3 D middle picture) and two animals showed complete paralysis of both front limbs (fig. 3.3 D right picture).

Table 3.1 Clinical characteristics of βSyn-induced ptEAE

# animals	Disease onset (day)	Disease duration (days)	Peak on day	Max. score	Cumulative score	% BWL	% incidence
135	5,17± 0,74	2,70± 0,96	6,76± 0,77	2,78± 1,16	7,89± 4,64	10,76± 4,51	88,89

BWL, body weight loss; max., maximal; #, number; %, percent.

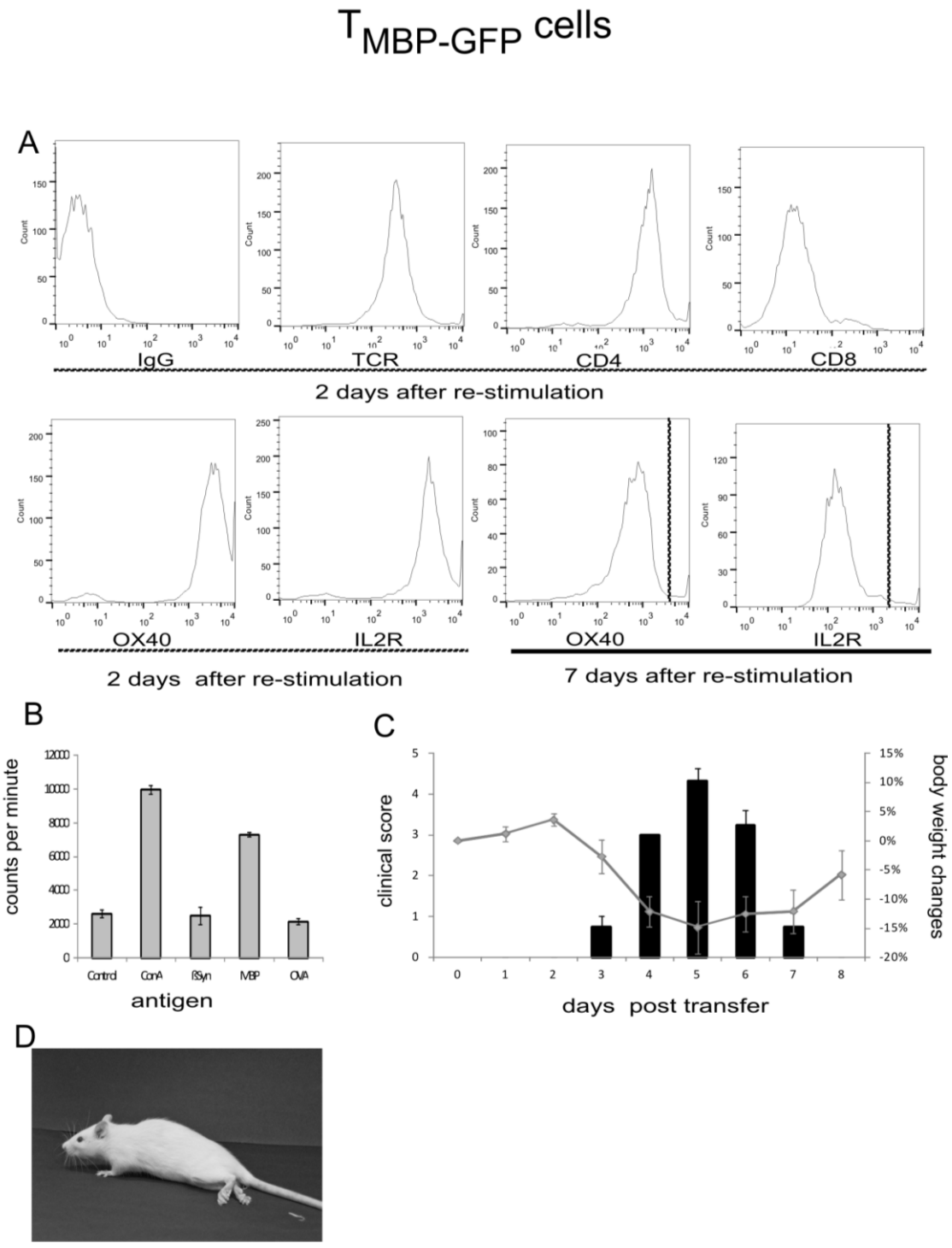

Figure 3.2 Characterisation of $T_{MBP\text{-}GFP}$ cells *in vitro* and *in vivo*. (A) $T_{MBP\text{-}GFP}$ cell phenotype. Expression of T cell markers TCR, CD4, CD8 and activation markers OX40 and IL-2R on the surface of T cell blasts (2 days after re-stimulation) and resting T cells (7 days after re-stimulation) was measured by flow cytometry. IgG, isotype control. **(B)** $T_{MBP\text{-}GFP}$ cell antigen specificity assessed by ^{3}H-thymidine proliferation assay. $T_{MBP\text{-}GFP}$ cells were co-cultured with irradiated thymocytes in presence of no antigen (control); Concanavalin A (ConA); β-Synuclein$_{93\text{-}111}$ peptide (βSyn); myelin basic protein (MBP); ovalbumin (OVA). 48 h later ^{3}H-thymidine was added. Radioactive incorporation was measured after further 12 h. Average and SD of triplicate samples are

depicted. **(C)** Clinical course of ptEAE. The graph shows a representative disease course. Average body weight changes in per cent (line) and clinical symptoms (bars) following intravenous transfer of $T_{MBP\text{-}GFP}$ cells in Lewis rats. Average and SD are depicted. n = 8. **(D)** Photographic documentation of the typical ptEAE symptom hind limb paralysis at the peak of the disease.

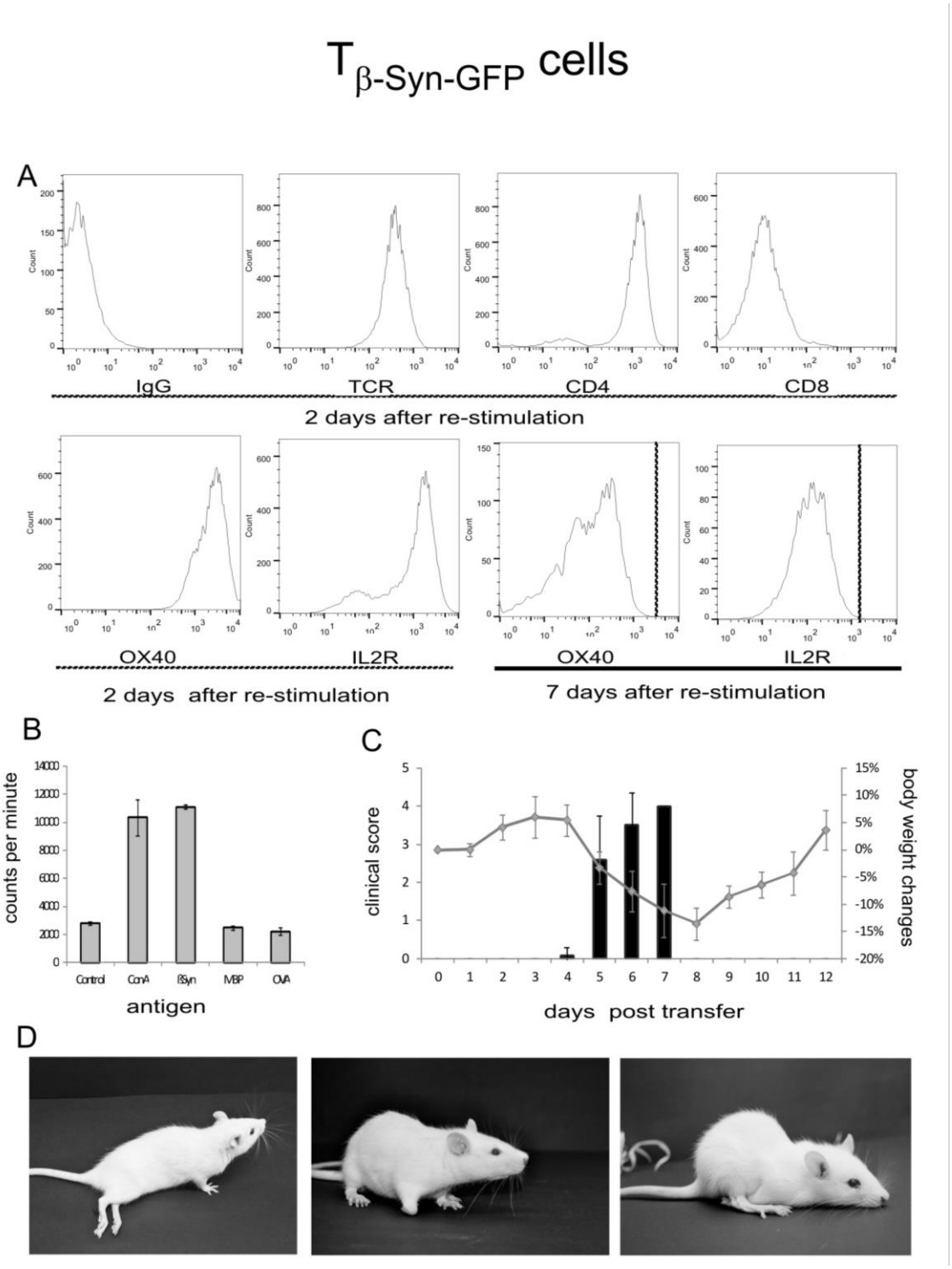

Figure 3.3 Characterisation of $T_{\beta Syn\text{-}GFP}$ cells *in vitro* and *in vivo*. (A) $T_{\beta Syn\text{-}GFP}$ cell phenotype. Expression of T cell markers TCR, CD4, CD8 and activation markers OX40 and IL-2R on the surface of T cell blasts (2 days after re-stimulation) and resting T cells (7 days after re-stimulation) was measured by flow cytometry. IgG, isotype control. **(B)** $T_{\beta Syn\text{-}GFP}$ cell antigen specificity assessed by ^{3}H-thymidine proliferation assay. The assay was performed as in fig. 3.2 B. Average and SD of triplicate samples are depicted. **(C)** Clinical course of ptEAE. The graph shows a representative disease course. Average body weight changes in per cent (line) and clinical symptoms (bars) following intravenous transfer of $T_{\beta Syn\text{-}GFP}$ cells in Lewis rats. Average and SD are depicted. n = 6. **(D)** Photographic documentation of the typical ptEAE symptom hind limb paralysis at the peak of the disease (left), and the uncommon symptoms of front limb weakness (middle) or front limb paralysis (right picture).

3.3. Infiltration kinetics of $T_{MBP\text{-}GFP}$ and $T_{\beta Syn\text{-}GFP}$ cells into the CNS

After showing that antigen-specific effector $T_{MBP\text{-}GFP}$ and $T_{\beta Syn\text{-}GFP}$ cells both induce a similar monophasic paralytic disease, I next investigated the infiltration kinetics of these cells during the different ptEAE phases. In the preclinical phase, $T_{\beta Syn\text{-}GFP}$ cells showed a similar homing kinetic as $T_{MBP\text{-}GFP}$ cells. Cells of both specificities infiltrated first the lung and then drastically increased in blood and spleen just before entering the CNS (fig. 3.4, and published for MBP-specific T cells in (Flügel et al., 2001; Odoardi et al., 2012)). As described before, $T_{\beta Syn\text{-}GFP}$ cells induced a prolonged preclinical phase. During this phase a 2-40-fold higher number of infiltrated antigen-specific T cells could be detected in peripheral organs (fig. 3.4). At the end of the preclinical phase (day 3 post transfer for $T_{MBP\text{-}GFP}$ cells; day 4 post transfer for $T_{\beta Syn\text{-}GFP}$ cells) effector T cells started to enter the CNS. $T_{MBP\text{-}GFP}$ cells infiltrated the meninges of the brain and SC in similar numbers, whereas in the parenchyma MBP-specific T cells in the SC highly outnumbered those in the brain (fig. 3.5 A). $T_{\beta Syn\text{-}GFP}$ cell invasion into the meninges was more pronounced in the brain compared to the SC. Interestingly, the number of these T cells in both brain and spinal cord parenchyma was very similar (fig. 3.5 B).

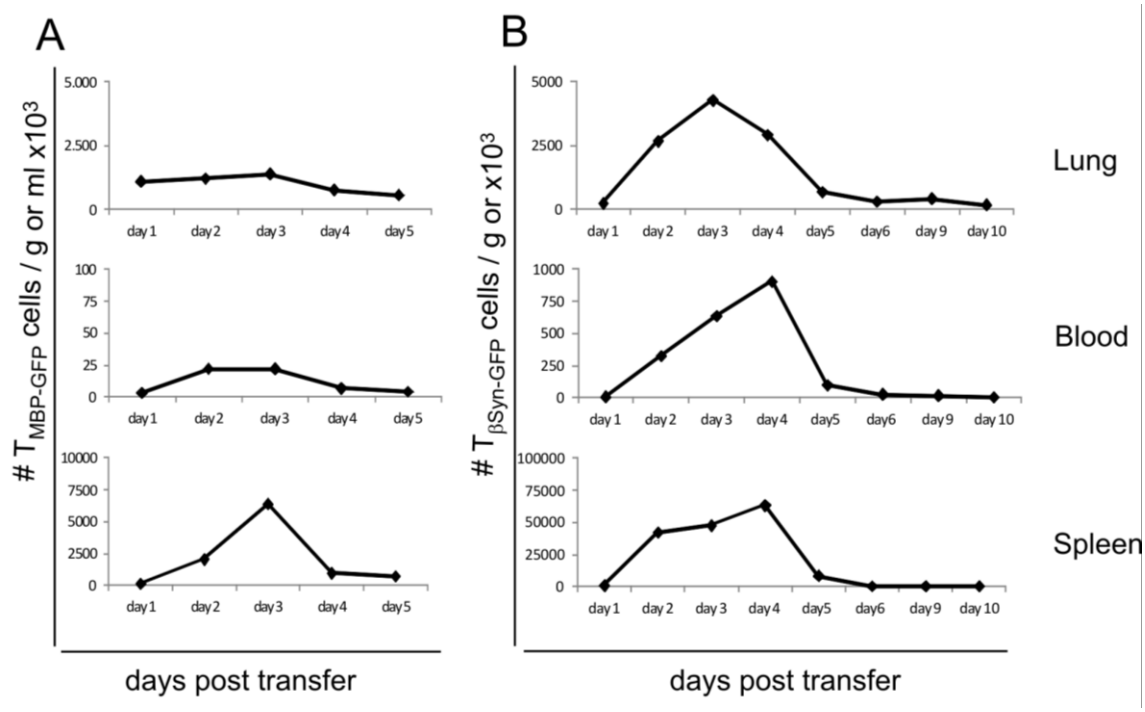

Figure 3.4 $T_{MBP-GFP}$ and $T_{\beta Syn-GFP}$ cell homing into peripheral organs during ptEAE. $T_{MBP-GFP}$ or $T_{\beta Syn-GFP}$ cell blasts were transferred into recipient rats and their infiltration into the peripheral organs lung, blood and spleen was determined during ptEAE by flow cytometry. **(A)** Infiltration kinetic of $T_{MBP-GFP}$ cells. **(B)** Infiltration kinetic $T_{\beta Syn-GFP}$ cells. Absolute numbers of $T_{MBP-GFP}$ or $T_{\beta Syn-GFP}$ cells /gram or ml of organ x 10^3. #, number; g, gram.

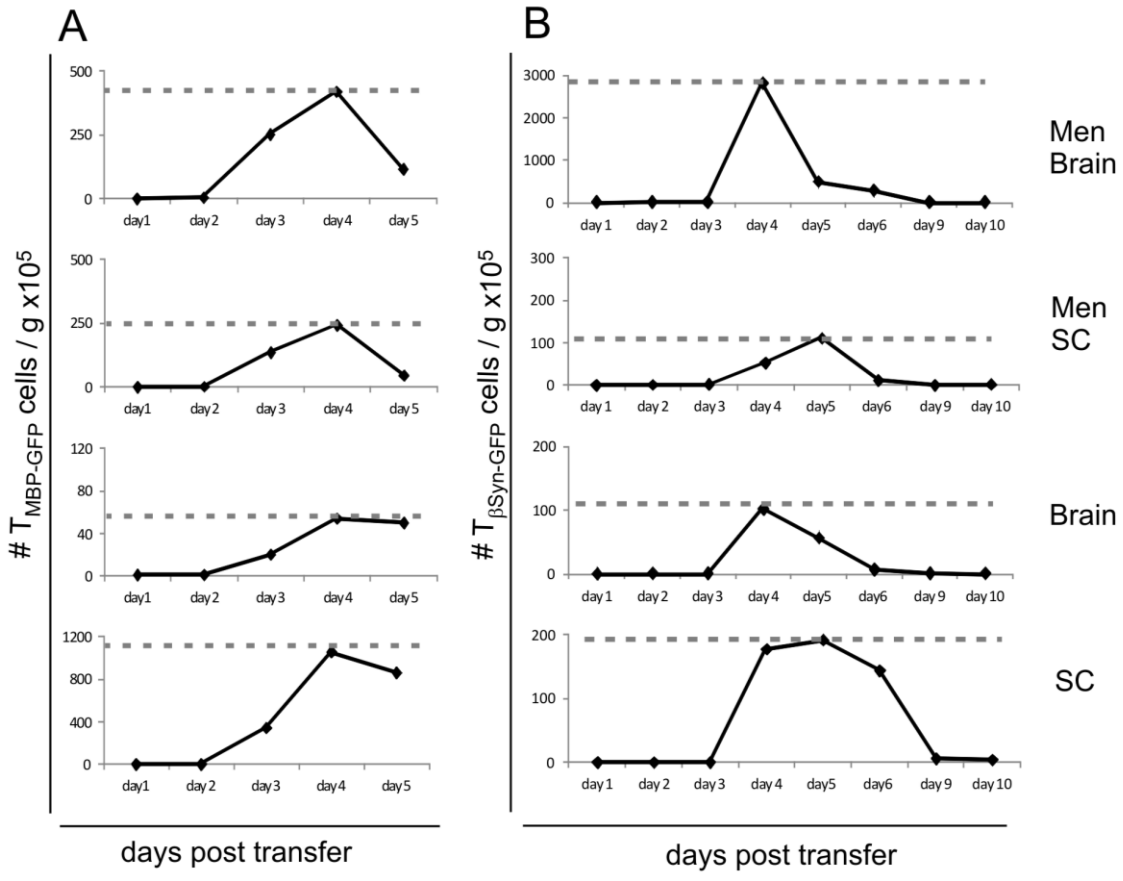

Figure 3.5 $T_{MBP\text{-}GFP}$ and $T_{\beta Syn\text{-}GFP}$ cell homing into the CNS during ptEAE. $T_{MBP\text{-}GFP}$ or $T_{\beta Syn\text{-}GFP}$ cell blasts were transferred into recipient rats and their infiltration into the brain meninges (Men Brain), SC meninges (Men SC), brain parenchyma (Brain) and SC parenchyma (SC) was determined during ptEAE by flow cytometry. **(A)** Infiltration kinetic of $T_{MBP\text{-}GFP}$ cells. **(B)** Infiltration kinetic $T_{\beta Syn\text{-}GFP}$ cells. Absolute numbers of $T_{MBP\text{-}GFP}$ or $T_{\beta Syn\text{-}GFP}$ cells /gram of organ x 10^5. #, number; g, gram.

3.4 Infiltration route and tissue distribution of $T_{MBP\text{-}GFP}$ and $T_{\beta Syn\text{-}GFP}$ cells within the CNS

3.4.1 Analysis at the onset of disease

To validate the kinetic data of infiltrated $T_{MBP\text{-}GFP}$ and $T_{\beta Syn\text{-}GFP}$ cells and to learn about the entry route and the areas of the CNS that were targeted by these cells, decalcified cryo-sections from the brain (coronal sections) and SC (transverse sections) of ptEAE-affected rats were prepared and histologically analysed by fluorescence microscopy. The advantage of decalcification is that this technique allows the sectioning of the CNS tissue with the surrounding bone. The meninges of the CNS remain intact and therefore meningeal infiltration by effector T cells can be analysed. At the onset of $T_{MBP\text{-}GFP}$ cell-induced ptEAE cortical meningeal and perivascular meningeal T cell infiltration was detected in brain coronal sections (fig. 3.6 A-C). Moreover, some $T_{MBP\text{-}GFP}$ cells infiltrated the sub-pial tissue and the ventricular ependyma at this time point (fig. 3.6. B and D). T cell infiltration in the choroid plexus epithelium was not observed in any of the analysed sections (fig. 3.6 D). In the meninges surrounding the hypothalamus first $T_{MBP\text{-}GFP}$ cell infiltrates were detected (fig. 3.6 K). No inflammatory foci were visible in the parenchyma, both in the grey and white matter (fig. 3.6 A-E). A similar infiltration pattern of the brain, as described for $T_{MBP\text{-}GFP}$ cells, was observed for βSyn-induced ptEAE at this early time point of the disease (fig. 3.6 F-J, L).

The analysis of SC transverse sections (thoracic level) from animals affected by $T_{MBP\text{-}GFP}$ cell -induced ptEAE showed the following typical homing pattern. At the onset of the disease $T_{MBP\text{-}GFP}$ cells started to infiltrate the tissue from the meninges. A characteristic meningeal ring of T cell infiltrates around the SC parenchyma was detected (fig. 3.7 A-B). In the vicinity of these cells first sub-pial and intraparenchymal $T_{MBP\text{-}GFP}$ cells were visible (fig. 3.7 B-C). In comparison, $T_{\beta Syn\text{-}GFP}$ cell infiltration in the SC meninges was less pronounced in the early EAE phase and mainly limited to the area where the meninges are attached to the dorsal horn and in close proximity to the grey matter (fig. 3.7 D-E). Surprisingly, intense deep grey matter βSyn T cell infiltrates around parenchymal vessels were observed (fig. 3.7 F). Moreover, at this time point of ptEAE, βSyn-specific T cells have started to infiltrate the grey matter of the

spinal cord (fig. 3.7 F). No infiltration foci in the white matter parenchyma could be observed (fig. 3.7 D-F).

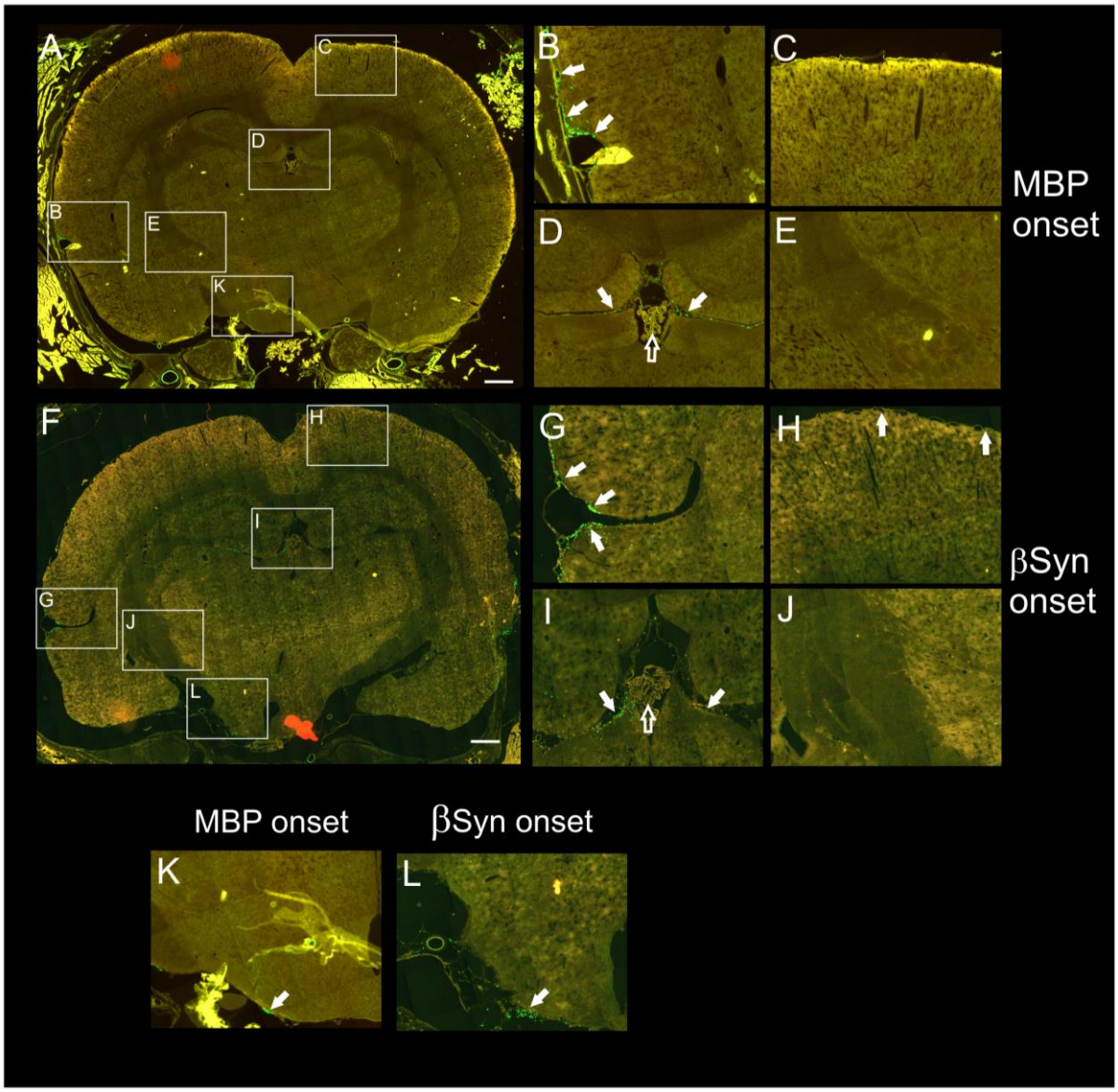

Figure 3.6 $T_{MBP\text{-}GFP}$ and $T_{\beta Syn\text{-}GFP}$ cell infiltration route into the brain at the onset of ptEAE. Representative fluorescence microscopic images of brain coronal sections (at the level of the hippocampus) at the onset of ptEAE induced either by $T_{MBP\text{-}GFP}$ cells **(A-E and K)** or by $T_{\beta Syn\text{-}GFP}$ cells **(F-J and L)**. **(A and F)** Overview. Magnifications: **(B/G)** cortical meningeal and perivascular meningeal T_{GFP} cell infiltrates, T_{GFP} cell infiltration in: **(C/H)** parietal cortex/associated pia mater, **(D/I)** dorsal third ventricle with choroid plexus, **(E/J)** internal capsule, **(K/L)** hypothalamus. Closed arrows indicate $T_{MBP\text{-}GFP}$ or $T_{\beta Syn\text{-}GFP}$ cells, open arrows point to non-infiltrated choroid plexus epithelium. **(A and F)** Scale bar: 1000 µm, **(B-E, G-L)** magnifications (approx. 3 x).

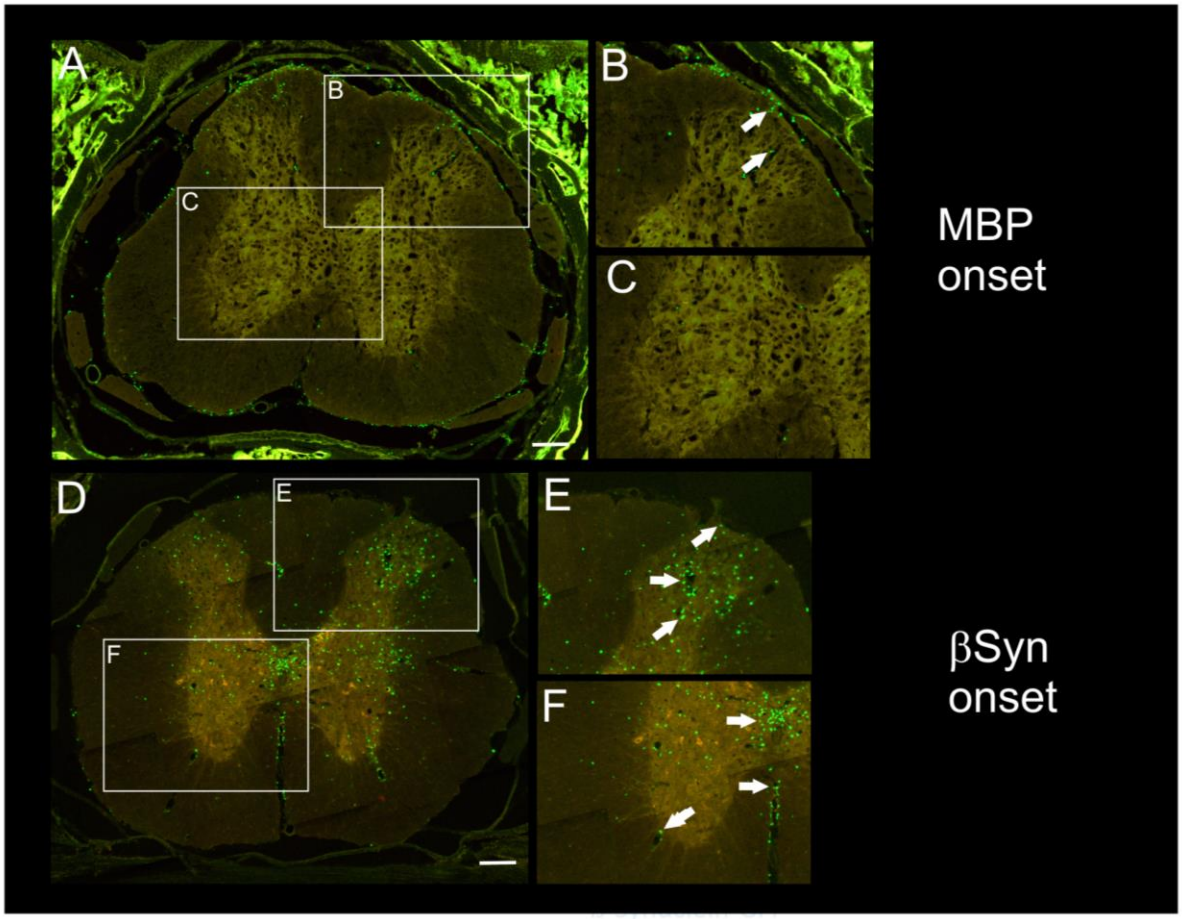

Figure 3.7 $T_{MBP\text{-}GFP}$ and $T_{\beta Syn\text{-}GFP}$ cell infiltration route into the SC at the onset of ptEAE. Representative fluorescence microscopic images of SC transverse sections (thoracic level) at the onset of ptEAE induced either by $T_{MBP\text{-}GFP}$ cells **(A-C)** or by $T_{\beta Syn\text{-}GFP}$ cells **(D-F)**. **(A and D)** Overview. Magnifications: T_{GFP} cell infiltration in: **(B and E)** pia mater and white matter, **(C and F)** deep grey matter. Closed arrows indicate $T_{MBP\text{-}GFP}$ or $T_{\beta Syn\text{-}GFP}$ cells. **(A and D)** Scale bar: 200 µm, **(B-C, E-F)** magnifications (approx. 1.5 x).

3.4.2 Analysis at the peak of disease

As already indicated by the flow cytometric data (see chapter 3.3) only a low number of infiltrated effector T cells was seen by fluorescence microscopy in the brain parenchyma at the peak of ptEAE induced by $T_{MBP\text{-}GFP}$ cells. A limited fraction of pial and single sub-pial cortical $T_{MBP\text{-}GFP}$ cells were detected (fig. 3.8 B and C). Parenchymal T cell infiltration was visible adjacent to ventricular ependyma (fig. 3.8 D, here adjacent to the dorsal third ventricle) and in the hypothalamic tissue near to the hypothalamic meninges (fig. 3.8 K). The hot spots of parenchymal T cell infiltration however, were white matter regions like the internal capsule and the optic tract (fig. 3.8 E). In contrast, animals affected by $T_{\beta Syn\text{-}GFP}$ cell-induced EAE show a high number of cortical grey matter infiltration at the peak of disease. Massive sub-pial and moreover intra-cortical T cell spreading was detected (fig. 3.8 G and H).

Furthermore, parenchymal infiltration around the ventricular system and within the hypothalamus was observed (fig. 3.8 I and L). In general, myelin-poor regions were favoured by $T_{\beta Syn\text{-}GFP}$ cells whereas white matter-rich regions were mainly devoid of these cells (fig. 3.8 J). In the SC, $T_{MBP\text{-}GFP}$ cells were spread not just throughout the white matter but also deeply inside the grey matter (fig. 3.9 A-C). In striking contrast to $T_{MBP\text{-}GFP}$ cell distribution, the massive infiltration of $T_{\beta Syn\text{-}GFP}$ cells was mostly confined to the grey matter parenchyma (fig. 3.9 D-F).

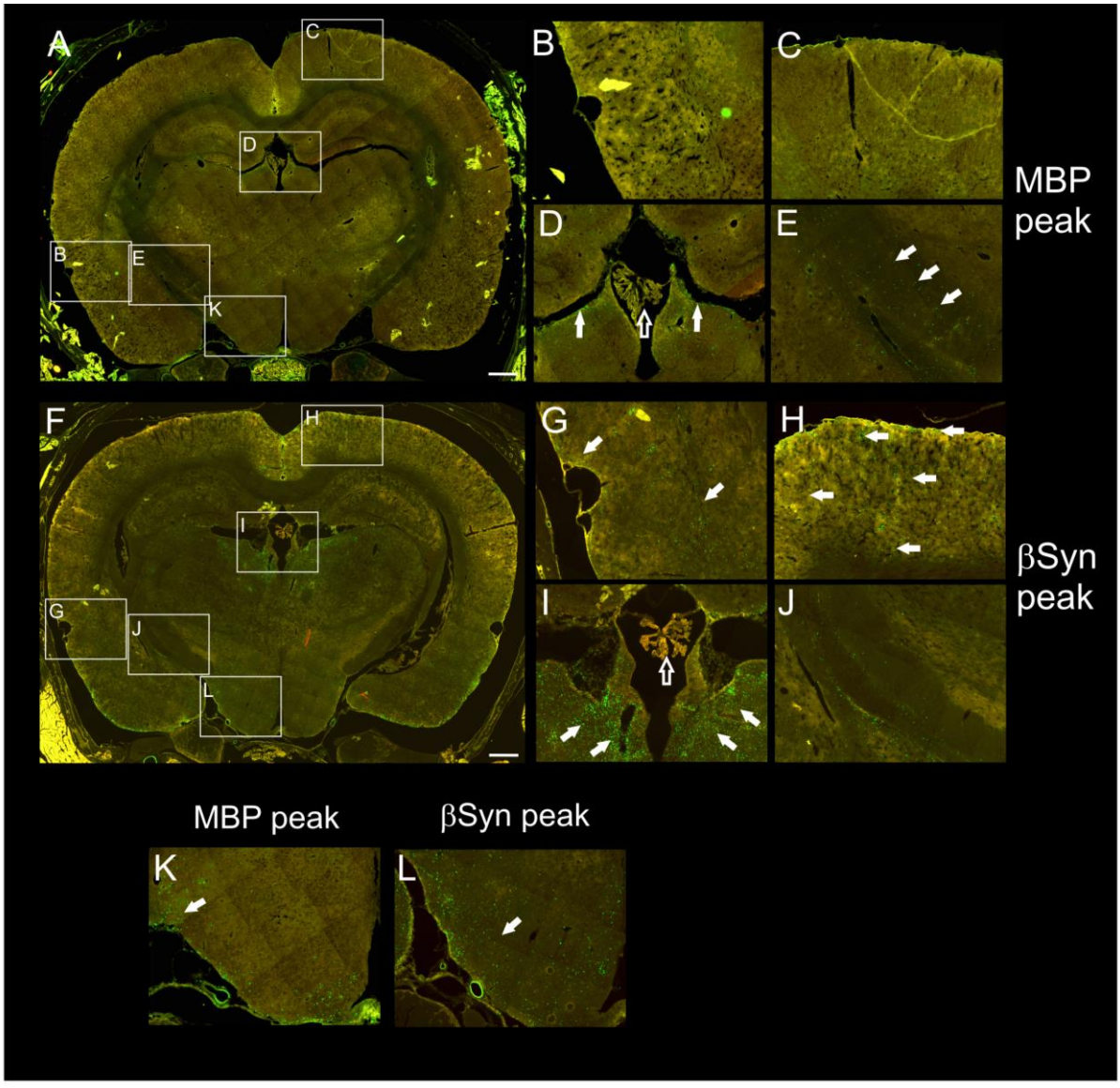

Figure 3.8 Regions of the brain infiltrated by $T_{MBP\text{-}GFP}$ and $T_{\beta Syn\text{-}GFP}$ cells at the peak of ptEAE. Representative fluorescence microscopic images of brain coronal sections (at the level of the hippocampus) at the peak of ptEAE. **(A-E and K)** Brain of a $T_{MBP\text{-}GFP}$ cell-induced ptEAE-affected animal. **(F-J and L)** Brain of a $T_{\beta Syn\text{-}GFP}$ cell-induced ptEAE-affected animal. **(A/F)** Overview. Magnifications: **(B/G)** cortical meningeal and perivascular meningeal T_{GFP} cell infiltration, T_{GFP} cell infiltration in: **(C/H)** parietal cortex/associated pia mater, **(D/I)** dorsal third ventricle with choroid plexus, **(E/J)** internal capsule, **(K/L)** hypothalamus. Closed arrows

indicate $T_{MBP\text{-}GFP}$ or $T_{\beta Syn\text{-}GFP}$ cells, open arrows point to non-infiltrated choroid plexus epithelium. **(A and F)** Scale bar: 1000 µm, **(B-E, G-L)** magnifications (approx. 3 x).

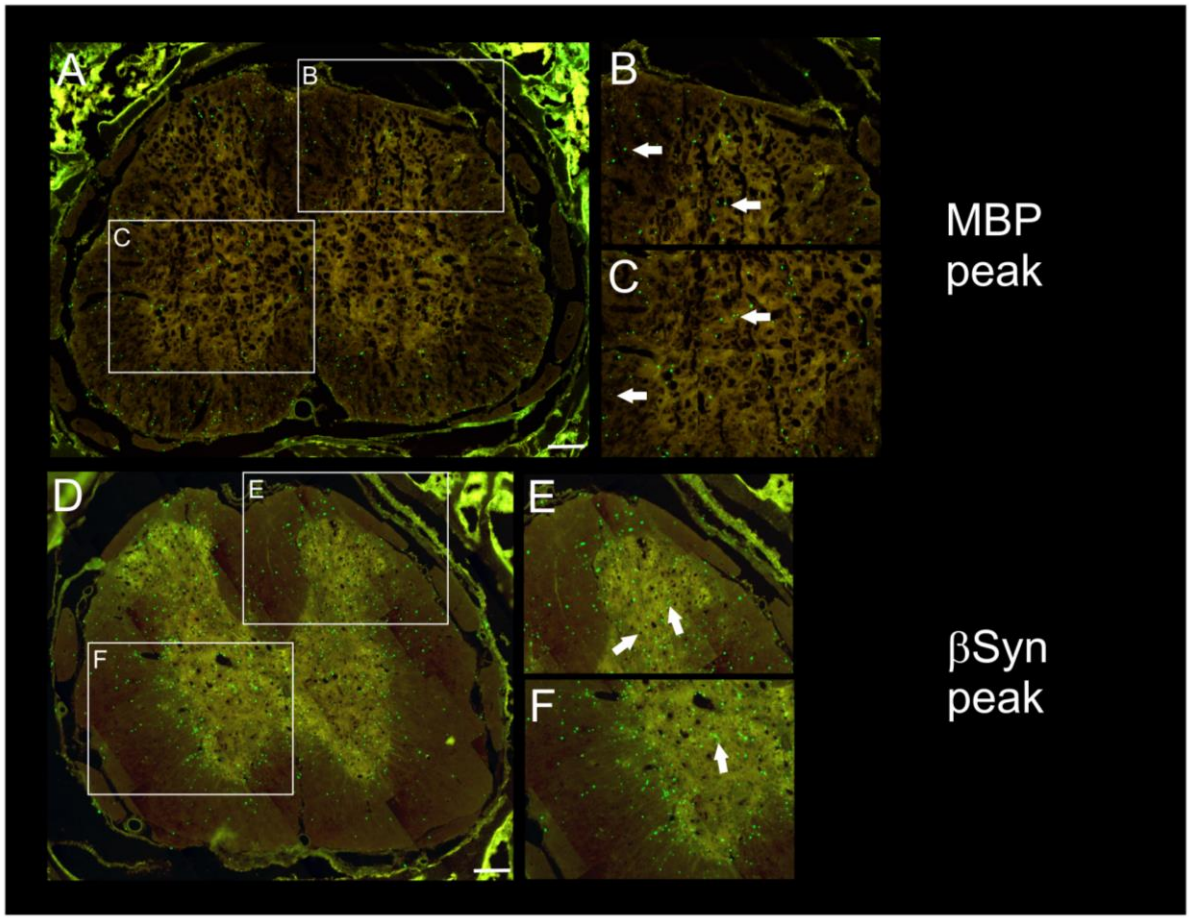

Figure 3.9 Regions of the spinal cord infiltrated by $T_{MBP\text{-}GFP}$ and $T_{\beta Syn\text{-}GFP}$ cells at the peak of ptEAE. Representative fluorescence microscopic images of SC transverse sections (thoracic level) at the peak of ptEAE. **(A-C)** SC of a $T_{MBP\text{-}GFP}$ cell-induced ptEAE-affected animal. **(D-F)** SC of a $T_{\beta Syn\text{-}GFP}$ cell-induced ptEAE-affected animal. **(A/D)** Overview. Magnifications: T_{GFP} cell infiltration in: **(B/E)** pia mater and white matter, **(C/F)** deep grey matter. Closed arrows indicate $T_{MBP\text{-}GFP}$ or $T_{\beta Syn\text{-}GFP}$ cells **(A and D)** Scale bar: 200 µm, **(B-C, E-F)**, magnifications (approx. 1.5 x).

3.5 Apoptosis rate of $T_{MBP\text{-}GFP}$ and $T_{\beta Syn\text{-}GFP}$ cells in the CNS

The previously described histological data indicated that the antigen specificity of effector T cells is important for entry site and distribution of these cells within the CNS. Next I asked whether differing apoptosis rate in $T_{MBP\text{-}GFP}$ and $T_{\beta Syn\text{-}GFP}$ cells in the target tissues could explain the observed different infiltration pattern. To answer this question, animals transferred either with $T_{MBP\text{-}GFP}$ or with $T_{\beta Syn\text{-}GFP}$ cells were sacrificed during the course of EAE. The CNS tissues were isolated and the percentage of effector T cells positive for active Caspase-3, an early apoptosis marker, was measured via flow cytometry.

This analysis revealed that independently from the EAE phase examined (onset, aggravation or peak) only a low percentage of $T_{MBP\text{-}GFP}$ cells extracted from brain and SC meninges and parenchyma were active Caspase-3-positive. The highest percentage of positive $T_{MBP\text{-}GFP}$ cells was detected in SC meninges whereas in brain meninges only half as much cells were apoptotic at the same time point. In the parenchyma no substantial differences in the percentage of apoptotic $T_{MBP\text{-}GFP}$ cells were detected (fig. 3.10 A).

The levels of apoptotic $T_{\beta Syn\text{-}GFP}$ cells in the CNS of ptEAE-affected animals were also at a low level during disease progression. Similar to the observation made for $T_{MBP\text{-}GFP}$ cells, no substantial differences in the percentage of active Caspase-3-positive $T_{\beta Syn\text{-}GFP}$ cells were detected in the different CNS compartments (fig. 3.10 B).

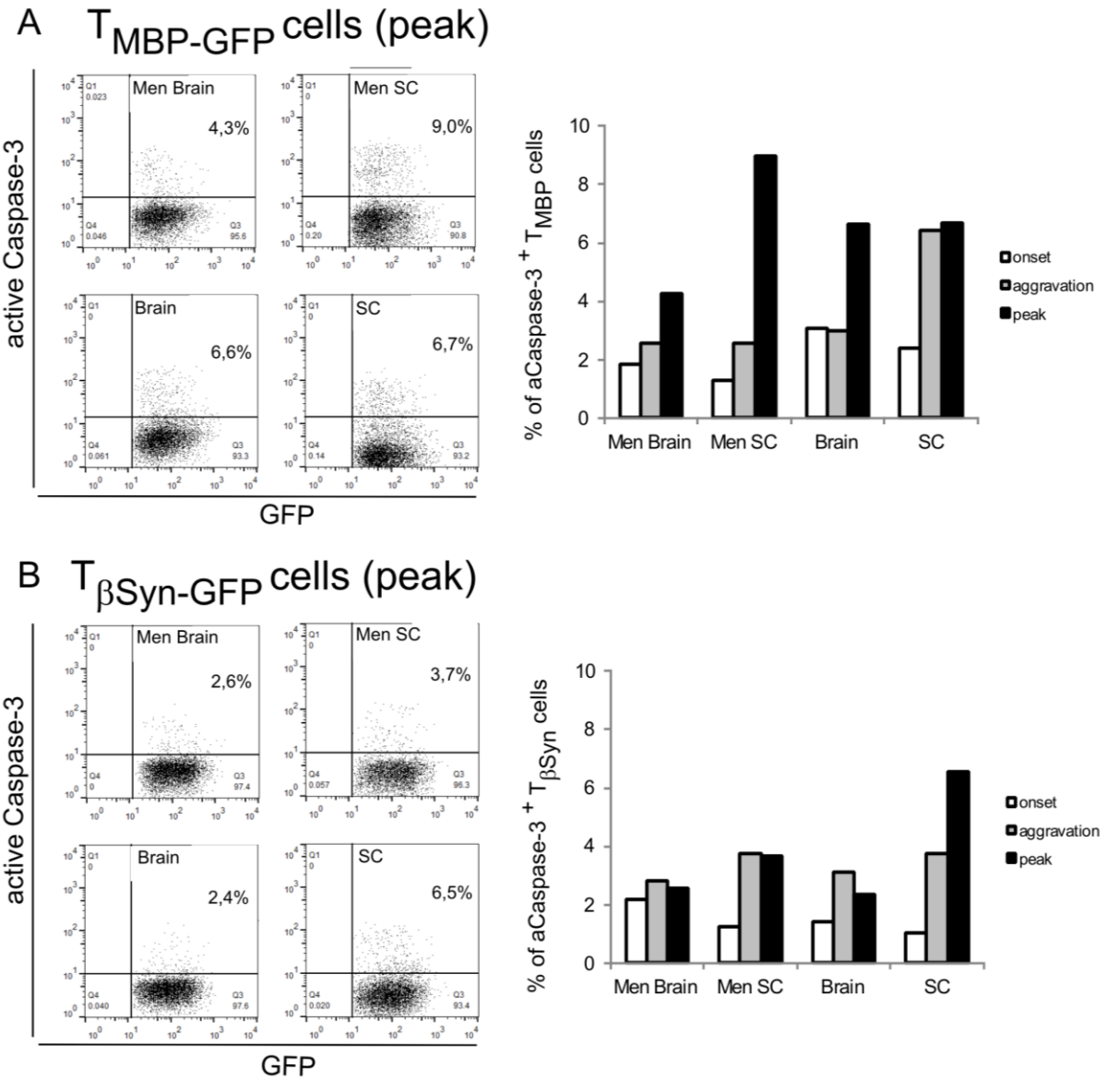

Figure 3.10 The apoptosis rate of $T_{MBP\text{-}GFP}$ and $T_{\beta Syn\text{-}GFP}$ cells in the CNS during EAE. $T_{MBP\text{-}GFP}$ or $T_{\beta Syn\text{-}GFP}$ cells were isolated from CNS tissue homogenates of ptEAE-affected animals during the course of the disease. T_{GFP} cells from brain meninges (Men Brain), SC meninges (Men SC), brain parenchyma (Brain) and SC parenchyma (SC) were stained for active Caspase-3. The percentage of positive T_{GFP} cells was determined via flow cytometry. **(A and B) left side:** Representative dot plots show active Caspase-3 expression of $T_{MBP\text{-}GFP}$ cells **(A)** or $T_{\beta Syn\text{-}GFP}$ cells **(B)** extracted from the indicated CNS compartments at the peak of the disease. **(A and B) right side:** Diagrams show the percentage of active Caspase-3-positive $T_{MBP\text{-}GFP}$ cells **(A)** or $T_{\beta Syn\text{-}GFP}$ cells **(B)** in different CNS compartments of ptEAE-affected animals at disease onset, during disease aggravation and at the peak of the disease.

3.6 Pro-inflammatory chemokine expression in MBP- and βSyn-induced ptEAE

Next it was investigated whether a differential expression of chemokines in the different CNS compartments could justify the observed homing pattern of effector T cells. Therefore, the expression of the chemokines CCL5, CXCL9, CXCL10, CXCL11 and CXCL12 was analysed via QRT PCR in the naïve situation or at the onset and peak of EAE induced by $T_{MBP\text{-}GFP}$ cells or $T_{\beta Syn\text{-}GFP}$ cells. At the day of T cell transfer (day 0), only a very low expression of the inflammatory chemokines CCL5, CXCL9, CXCL10 and CXCL11 was observed in the meninges and parenchyma of the CNS in both ptEAE types (fig. 3.11). In contrast, a high basal expression of CXCL12 was detected in the CNS meninges of these animals (fig. 3.11 A and B, upper rows). During EAE a strong reduction of CXCL12 expression was seen in brain and SC meninges independent of the antigen specificity of the disease-inducing T cells (fig. 3.11, upper rows).

During EAE induced by $T_{MBP\text{-}GFP}$ cells the expression of the inflammatory chemokines CXCL10 and CXCL11 was markedly up-regulated in SC meninges and parenchyma, especially at the onset of the disease. In addition, the CXCL9 level was elevated during ptEAE in the SC parenchyma compared to base level. The meninges and parenchyma of the brain showed only mild up-regulation of the chemoattractive guiding cues during disease progression compared to SC tissues (fig. 3.11 A).

In the meninges and SC parenchyma of animals affected by βSyn-induced ptEAE lower levels of inflammatory chemokines compared to animals affected by $T_{MBP\text{-}GFP}$ cell-induced ptEAE were observed. Taken together, these data indicated that the expression of the inflammatory chemokines during ptEAE mirrored the $T_{MBP\text{-}GFP}$ or $T_{\beta Syn\text{-}GFP}$ cell infiltration pattern.

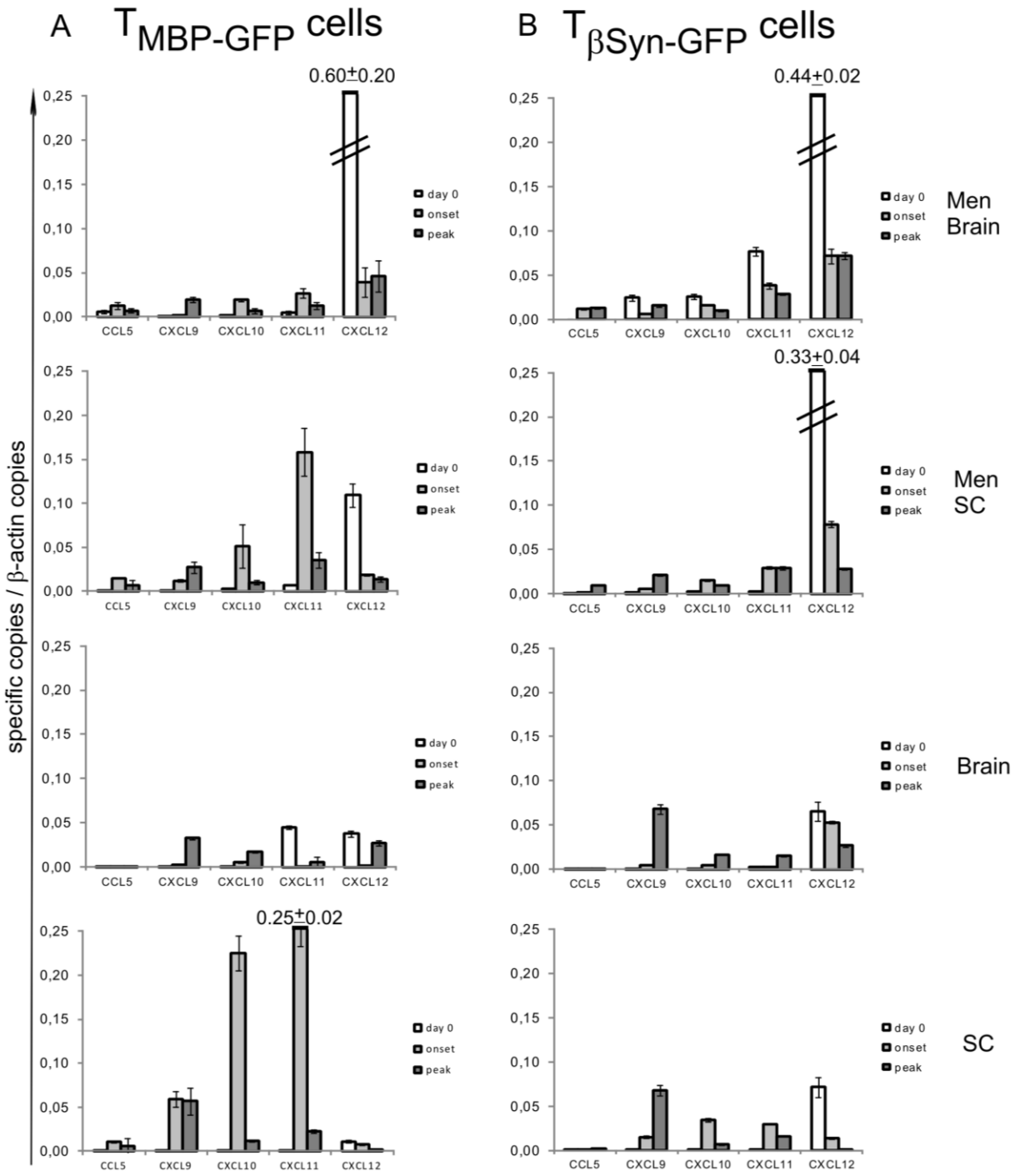

Figure 3.11 Expression of pro-inflammatory chemokines in the CNS during $T_{MBP\text{-}GFP}$ and $T_{\beta Syn\text{-}GFP}$ cell-induced ptEAE. Total CNS tissue homogenates were analysed for the expression of the pro-inflammatory chemokines CCL5, CXCL9, CXCL10, CXCL11 and the homeostatic chemokine CXCL12 by QRT-PCR. **(A) left column:** $T_{MBP\text{-}GFP}$ cell-induced chemokine expression. **(B) right column:** $T_{\beta Syn\text{-}GFP}$ cell-induced chemokine expression. Day 0, day of transfer; Men Brain, brain meninges; Men SC, SC meninges; Brain, brain parenchyma; SC, SC parenchyma; onset, onset of ptEAE; peak, peak of ptEAE. Specific copies in relation to β-actin copies are shown.

3.7 Chemokine receptor and integrin expression profile of $T_{MBP\text{-}GFP}$ and $T_{\beta Syn\text{-}GFP}$ cells during ptEAE

It has previously been shown that after transfer $T_{MBP\text{-}GFP}$ cells undergo in the peripheral organs a complex reprogramming that allow them to overcome the blood-brain barrier (BBB). More specifically the effector T cells down-regulate the activation markers and up-regulate the expression of several integrins and chemokine receptors (Odoardi et al., 2012). Therefore, I investigated whether the expression of chemokine receptors and integrins on the surface of effector $T_{MBP\text{-}GFP}$ and $T_{\beta Syn\text{-}GFP}$ cells is crucial for the observed divergent CNS homing pattern (see chapter 3.3 and 3.4). T_{GFP} cells of both specificities were purified via fluorescence activated cell sorting (FACS) from the blood of the T_{GFP} cell-injected animals at the onset of the disease and analysed for the expression of their surface receptor profile by QRT-PCR. $T_{MBP\text{-}GFP}$ and $T_{\beta Syn\text{-}GFP}$ cells expressed a similar pattern of the chemokine receptors CXCR4, CCR7, CCR6, CXCR3, CCR5 and of the integrins VLA-4 and LFA-1. The expression of CXCR3, CXCR4 and VLA-4 was more pronounced than the expression of the other surface receptors for both antigen-specific T cells (fig. 3.12 A). To flank the gene expression analysis with functional data a T cell migration assay was performed in which the chemotactic migration of the $T_{MBP\text{-}GFP}$ or $T_{\beta Syn\text{-}GFP}$ cell towards the chemokines CCL5, CCL19, CCL20, CXCL11 and CXCL12 was analysed. Both effector T cell types sorted from blood in the early phase of the disease showed a preferential migratory response to CCL20 and CXCL11 (fig. 3.12 B). According to these data the chemokine receptor/integrin expression profile in the periphery was not responsible for the observed different infiltration pattern of $T_{MBP\text{-}GFP}$ and $T_{\beta Syn\text{-}GFP}$ cells in the target tissues.

Next I investigated the chemokine receptor and integrin expression profile and the chemotactic behaviour of effector T cells of both specificities sorted from CNS tissue at the onset and peak of the disease. At both time points of investigation, auto-reactive $T_{MBP\text{-}GFP}$ and $T_{\beta Syn\text{-}GFP}$ cells show a similar expression pattern, as discovered previously for blood-purified effector T cells: Independently from the original CNS compartment, CXCR3 and CXCR4 were the most expressed chemokine receptors and in the integrin group VLA-4 was more expressed than LFA-1 (fig. 3.13 A and B). In addition, the same migratory response pattern of effector T cells to the inflammatory and the homeostatic or lymphoid chemokines was detected at the peak of disease. CCL20 and CXCL11 seemed to be chemo-attractive for both effector T cell types (fig. 3.14 A and B). In summary, there was no difference in the expression of surface receptors or the chemokine response pattern detectable in grey- or white

matter-specific T cells. Therefore, it seems unlikely that these proteins are responsible for the differences in T cell homing behaviour between $T_{MBP\text{-}GFP}$ and $T_{\beta Syn\text{-}GFP}$ cells.

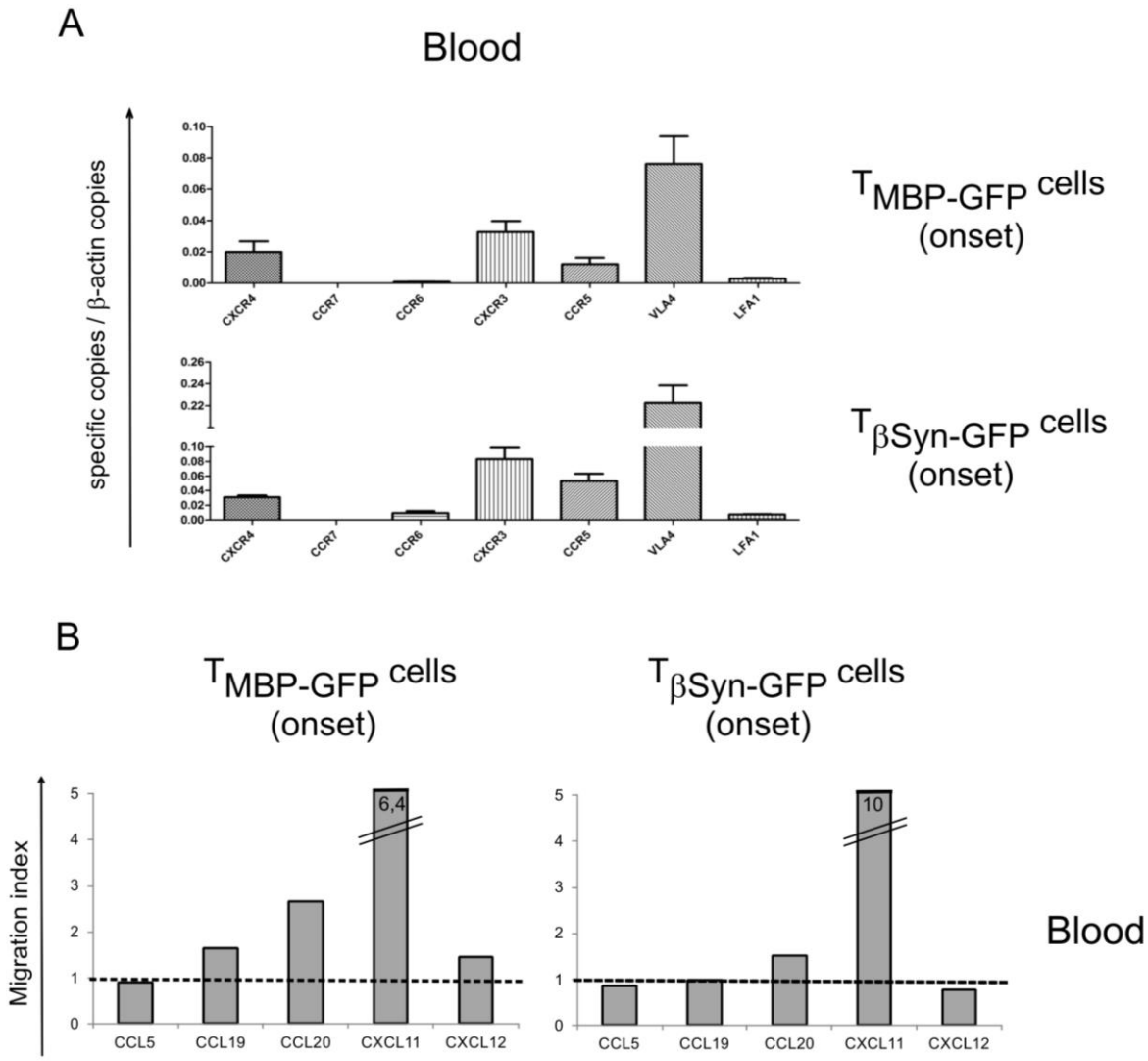

Figure 3.12 Surface expression of chemokine receptors and integrins and chemotactic response of blood-derived effector $T_{MBP\text{-}GFP}$ and $T_{\beta Syn\text{-}GFP}$ cells during ptEAE. EAE was induced by the transfer of $T_{MBP\text{-}GFP}$ or $T_{\beta Syn\text{-}GFP}$ cells to Lewis rats. Peripheral blood T_{GFP} cells were collected and **(A)** purified by FACS sorting at the early disease onset or **(B)** enriched by an OptiPrep gradient at the same time point. **(A)** The expression of the chemokine receptors CXCR4, CCR7, CCR6, CXCR3, CCR5 and the integrins VLA-4 and LFA-1 was analysed by QRT-PCR. Specific copies in relation to β-actin copies are shown. Data of two independent experiments are shown. Average and SD are depicted. **(B)** The ability of effector T cells to migrate towards the chemokines CCL5, CCL19, CCL20, CXCL11 or CXCL12 was tested by a transwell migration assay. Migrated T cells were counted by flow cytometry and the migratory response of the T cells was calculated as cell migration index (ratio of transmigrated T cells in response to chemokines versus control without chemokines). One representative data set of two independent experiments is shown.

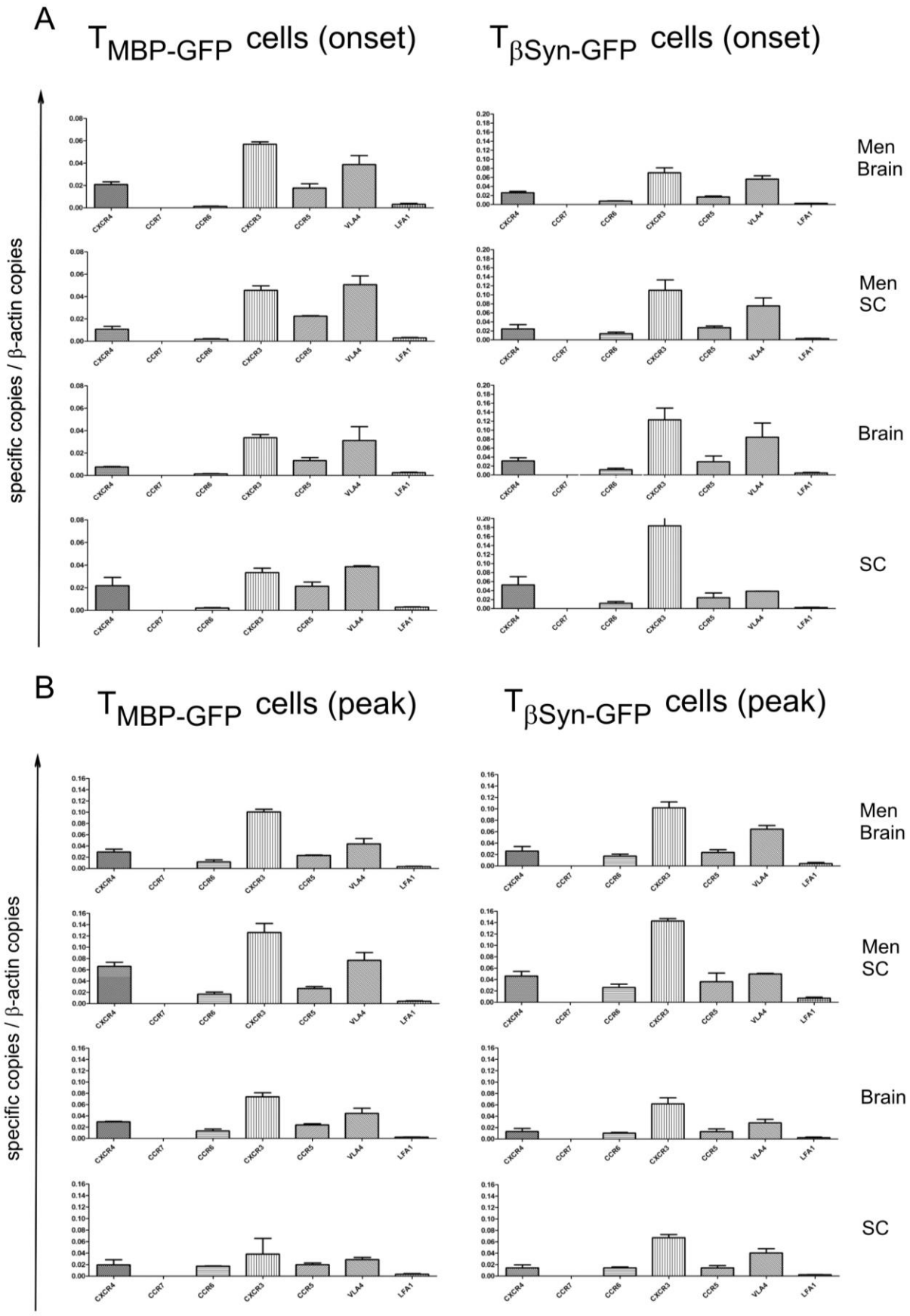
A
T MBP-GFP cells (onset)
T βSyn-GFP cells (onset)
specific copies / β-actin copies
Men Brain
Men SC
Brain
SC
CXCR4
CCR7
CCR6
CXCR3
CCR5
VLA4
LFA1
B
T MBP-GFP cells (peak)
T βSyn-GFP cells (peak)
specific copies / β-actin copies
Men Brain
Men SC
Brain
SC

Figure 3.13 The surface expression pattern of chemokine receptors and integrins of CNS-derived effector $T_{MBP\text{-}GFP}$ and $T_{\beta Syn\text{-}GFP}$ cells during ptEAE. EAE was induced by the transfer of $T_{MBP\text{-}GFP}$ or $T_{\beta Syn\text{-}GFP}$ cells to Lewis rats. T_{GFP} cells in CNS tissue homogenate were enriched by a percoll gradient and further purified by FACS at disease onset **(A)** or at the peak of the disease **(B)**. The expression of the chemokine receptors CXCR4, CCR7, CCR6, CXCR3, CCR5 and the integrins VLA-4 and LFA-1 was analysed by QRT-PCR. Specific copies in relation to β-actin copies are shown. Data of three independent experiments are shown. Average and SD are depicted. Men Brain, brain meninges; Men SC, SC meninges; Brain, brain parenchyma; SC, SC parenchyma.

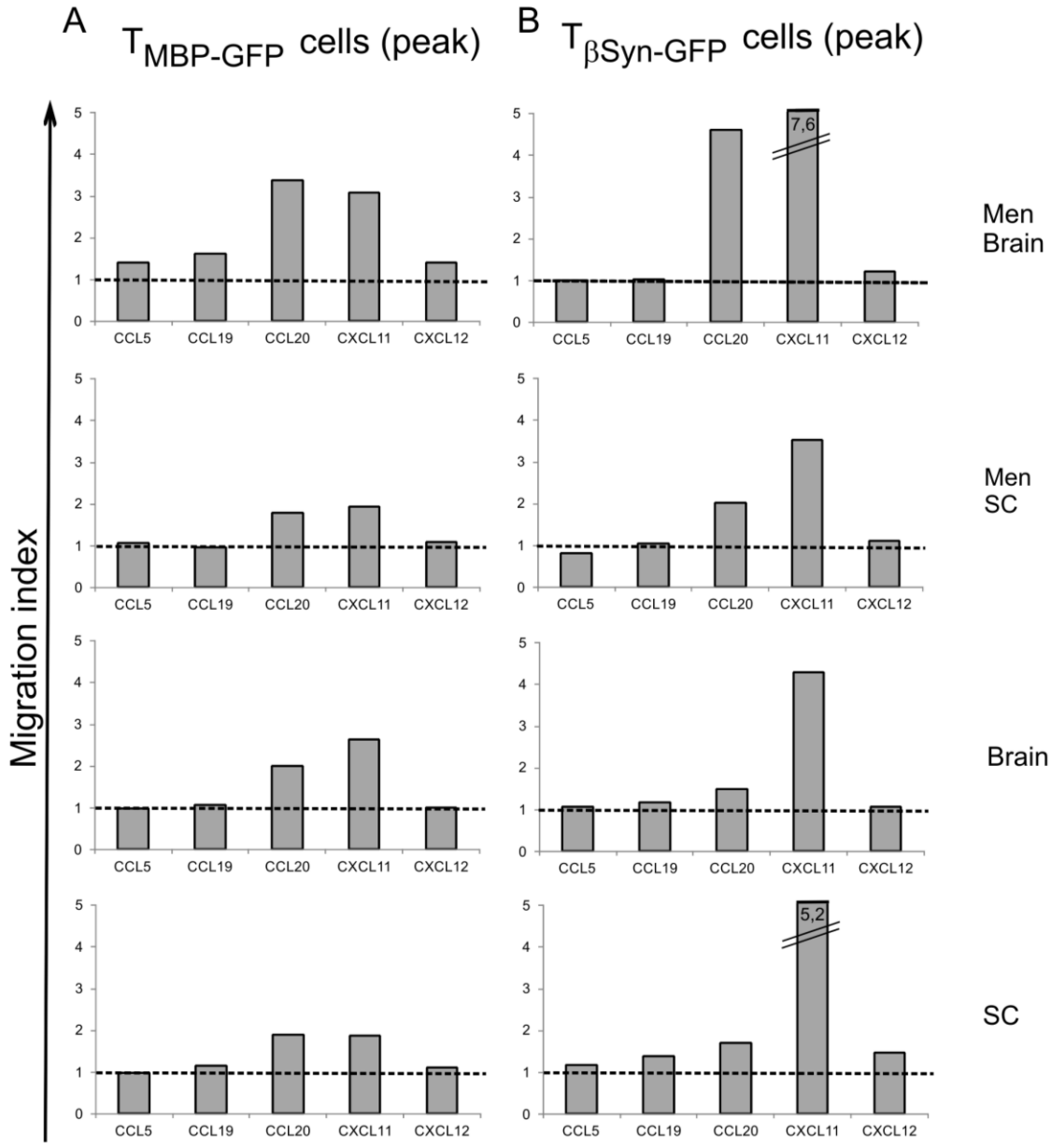

Figure 3.14 The migratory response pattern of CNS-isolated effector $T_{MBP\text{-}GFP}$ and $T_{\beta Syn\text{-}GFP}$ cells in $T_{MBP\text{-}GFP}$ or $T_{\beta Syn\text{-}GFP}$ cell-induced ptEAE. EAE was induced by the transfer of $T_{MBP\text{-}GFP}$ or $T_{\beta Syn\text{-}GFP}$ cells to Lewis rats. Animals were sacrificed at the peak of the disease. T_{GFP} cells in CNS tissue homogenate were enriched by an OptiPrep gradient. The ability of effector T cells to migrate towards the chemokines CCL5, CCL19, CCL20, CXCL11 or CXCL12 was analysed by a transwell migration assay. Migrated T cells were counted by flow

cytometry and the migratory response was calculated as cell migration index (ratio of transmigrated T cells in response to chemokines versus control without chemokines). One representative data set of two independent experiments is shown. Men Brain, brain meninges; Men SC, SC meninges; Brain, brain parenchyma; SC, SC parenchyma.

3.8 The activation state of effector T cells in the target organ and its role for CNS homing.

It was shown that effector T cells, which overcome the BBB, have to be locally re-activated by APCs presenting their cognate antigen in order to penetrate deeper into the CNS. This re-activation is strongly dependent on the availability of the antigen and the specificity of T cells. Therefore, only T cells, which encounter their specific antigen become activated and the activation state of effector T cells is crucial for the CNS homing behaviour (Bartholomäus et al., 2009). In order to test if the CNS activation profile is consistent with the infiltration pattern of $T_{MBP\text{-}GFP}$ or $T_{\beta Syn\text{-}GFP}$ cells, the CNS tissue of ptEAE-affected animals (MBP- and βSyn-specific subtypes) was analysed at the onset and the peak of the disease for the expression of the key T cell activation markers IFN-γ and IL-17 by QRT-PCR. At the onset of the disease a higher expression of both activation markers was detected in the SC meninges and even more pronounced in SC parenchyma compared with brain meninges and parenchyma during $T_{MBP\text{-}GFP}$ cell-induced ptEAE (fig. 3.15 A). The same tendency was seen at the peak of the disease in the parenchyma (fig. 3.15 C).

A different activation profile was observed in the target tissues of $T_{\beta Syn}$ cells: Here, the expression level of the activation markers in the meninges of brain and SC were similar at disease onset, whereas in the parenchyma there was a higher expression of IFN-γ and IL-17 in SC compared to brain (fig. 3.15 B). At the peak of the disease, the expression of both activation markers was on a similar level in all analysed tissues (fig. 3.15 D).

To learn about the expression of key activation markers of effector T cells on their way to the CNS at the T cellular level, $T_{MBP\text{-}GFP}$ and $T_{\beta Syn\text{-}GFP}$ cells were sorted from blood of the respective ptEAE-affected animals in the early onset of the disease and analysed via QRT-PCR. Both cell types express IFN-γ and IL-17 at a similar level and in a similar IFN-γ to IL-17 ratio (fig. 3.16 A and B).

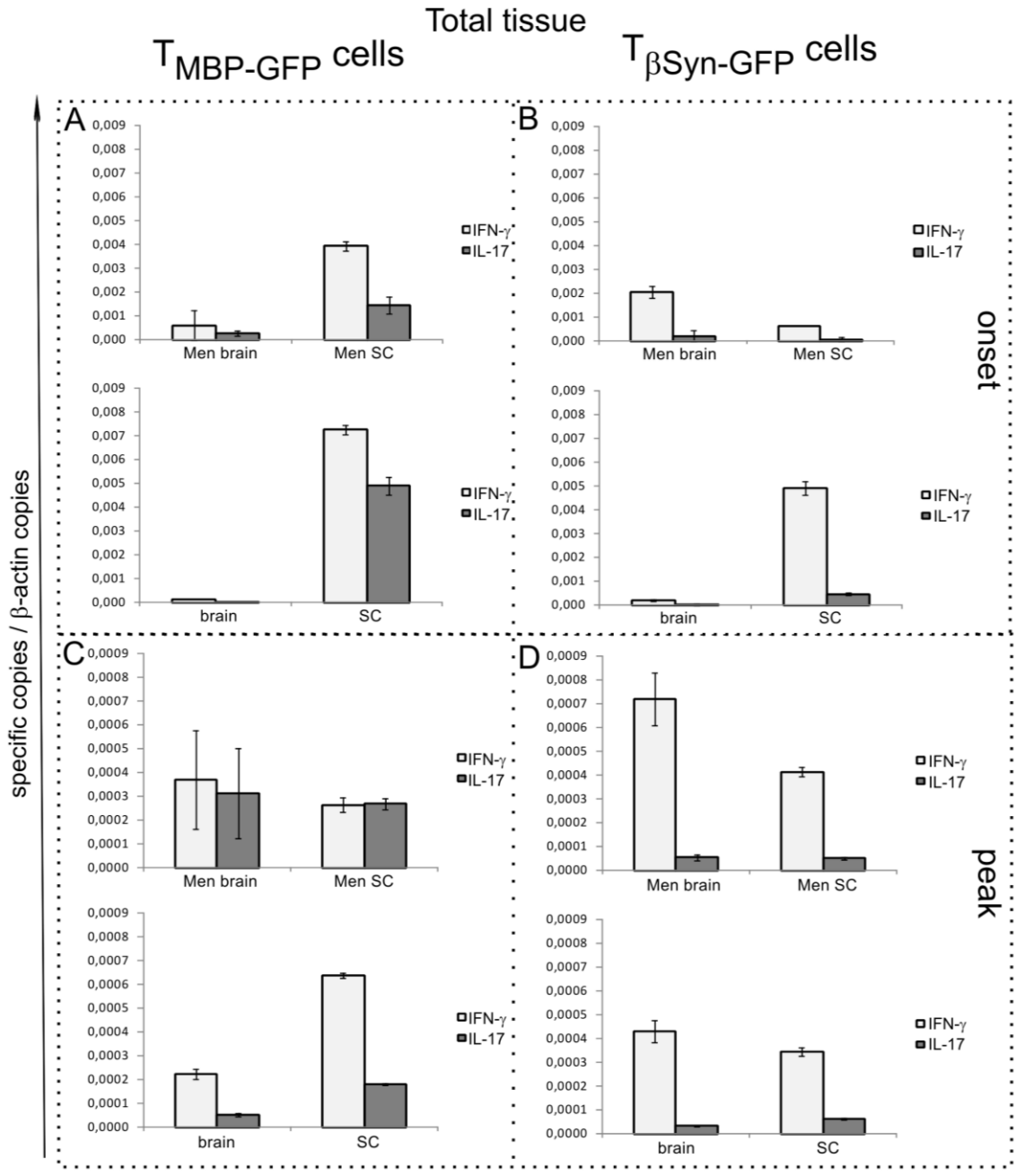

Figure 3.15 Expression of activation markers in CNS tissue. EAE was induced by the transfer of $T_{MBP\text{-}GFP}$ or $T_{\beta Syn\text{-}GFP}$ cells to Lewis rats. CNS tissue homogenate was analysed at disease onset **(A-B)** or at the peak of the disease **(C-D)** for the expression of the key cytokines IFN-γ and IL-17 via QRT-PCR. Of three independent experiments one representative data set is shown. Bars show specific copies in relation to β-actin copies. Average and SD of duplicate measurements are shown. Men Brain, brain meninges; Men SC, SC meninges; Brain, brain parenchyma; SC, SC parenchyma.

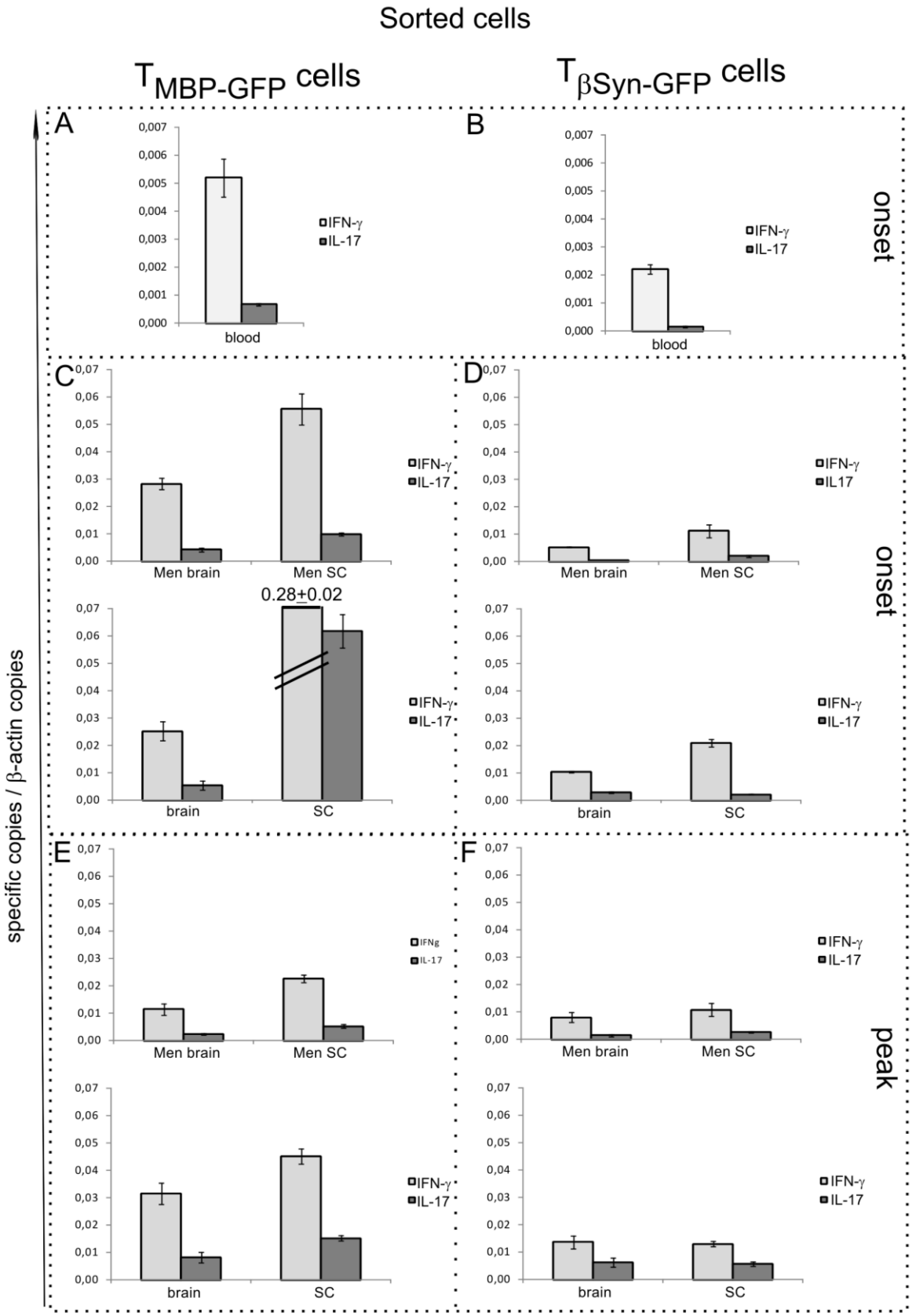

Figure 3.16 Expression of activation markers by effector T cells during ptEAE. EAE was induced by the transfer of $T_{MBP\text{-}GFP}$ or $T_{\beta Syn\text{-}GFP}$ cells to Lewis rats. T_{GFP} cells from blood or CNS tissue homogenate were enriched by lymphocyte separation medium or percoll gradient and further purified by FACS sorting at disease

onset **(A-D)** or at the peak of the disease **(E-F)**. The expression of the key cytokines IFN-γ and IL-17 was analysed by QRT-PCR. Of three independent experiments one representative data set is shown. Bars show specific copies in relation to β-actin copies. Average and SD of duplicate measurements are shown. Men Brain, brain meninges; Men SC, SC meninges; Brain, brain parenchyma; SC, SC parenchyma.

In order to evaluate the previous results from total CNS tissue at effector T cell level, cytokine expression analysis was additionally performed with sorted $T_{MBP\text{-}GFP}$ and $T_{\beta Syn\ -GFP}$ cells derived from total CNS tissue homogenates. This analysis revealed that independently from the antigen specificity, the time point or the tissue analysed the effector T cells sorted from the CNS were always more activated than the ones sorted from blood (fig. 3.16 A- F), which indicates that an activation of these T cells in the target tissue occurred.

$T_{MBP\text{-}GFP}$ cells sorted from meninges and parenchyma of the SC showed a higher activation marker expression compared to those isolated from brain meninges and parenchyma at the onset of the disease (fig. 3.16 C) whereas this tendency was less pronounced at the peak of the disease (fig. 3.16 E). Consistently with the analyses of total CNS homogenates (fig. 3.15 B and D, upper graphs), $T_{\beta Syn\text{-}GFP}$ cells sorted from the meninges of brain and SC show a nearly equal level of marker expression at the onset and the peak of disease (fig. 3.16 D and F, upper graphs). A similar expression pattern as in the meninges was detected in the parenchyma of the brain and the spinal cord (fig. 3.16 D and F). In general it was conspicuous that the activation marker expression was higher at disease onset compared to the peak of disease independent of the tissue analysed (fig. 3.15 and 3.16).

3.9 Visualization and *in situ* analysis of effector T cells in the target organ

3.9.1 Establishment of imaging windows to access CNS meninges

So far, all the described results were based on *ex vivo* analysis. In order to visualize $T_{MBP\text{-}GFP}$ or $T_{\beta Syn\text{-}GFP}$ cells directly in the target organ in living animals and to investigate their function at single cell level, live imaging by two-photon laser scanning microscopy (2P-LSM) of meninges of brain and spinal cord was performed. To access the dorsal spinal cord meninges, the “open spine window” preparation was performed, which is a well-established method in our lab. However, in order to access the meninges of the parietal cortex, an appropriate preparation method had to be established. Two different methods, a closed thinned skull and an open skull window, were developed, compared and tested for their applicability.

When compared, a higher laser power had to be applied through the thinned skull window in order to image the effector T cells in the meninges of the brain (tab. 3.2). Still, the imaging

depth of the open skull window was greater (200 µm vs. 100 µm) and it allowed the detection of deeper infiltrated T cells in the leptomeningeal area of the descending perforant vessels and of the parenchymal capillaries (tab. 3.2 and fig. 3.17 A-B). Moreover, it has previously been shown that the use of an open skull window for *in vivo* imaging was associated with high dendritic spine turnover and substantial glia activation starting 2 days after surgery (Xu et al., 2007). In our study the imaging session never lasted more than 12 hours, a time point not analysed in the mentioned work. However, considered these caveats, a parallel analysis of the motility behaviour of effector T cells was performed through both cranial windows at different time points of the disease. No differences in the motility pattern of extravasated effector T cells in the leptomeninges were observed. Imaged $T_{MBP\text{-}GFP}$ cells showed the same speed and straightness when imaged through one or the other cranial window (fig. 3.17 C). Therefore, the open skull window, which provides a deeper imaging field and thereby enables the imaging of descending vessels and deeper T cell infiltrates, was chosen for further experiments (fig. 3.17 B).

Table 3.2 Comparison between both established cranial window types for two-photon live imaging of effector T cell motility behaviour in brain leptomeninges

	Thinned skull window	**Open skull window**
Preparation-induced tissue damage (indicated by leakage of blood)	No remarkable damage ➔ method applicable independent of inflammation level	Limited leakage of dural blood vessels (at a high level of inflammation)
Laser power	35 %	28 %
Imaging depth	Approx. 100 µm	Approx. 200 µm
Motility behaviour of extravasated $T_{MBP\text{-}GFP}$ cells (speed and straightness)	No statistical differences to open skull window (see fig. 3.17 for further details)	No statistical differences to the thinned skull window (see fig. 3.17 for further details)

Statistical significance was determined by the Man Whitney test.

*P < 0.05; **P < 0.01; ***P < 0.001; ****P < 0.

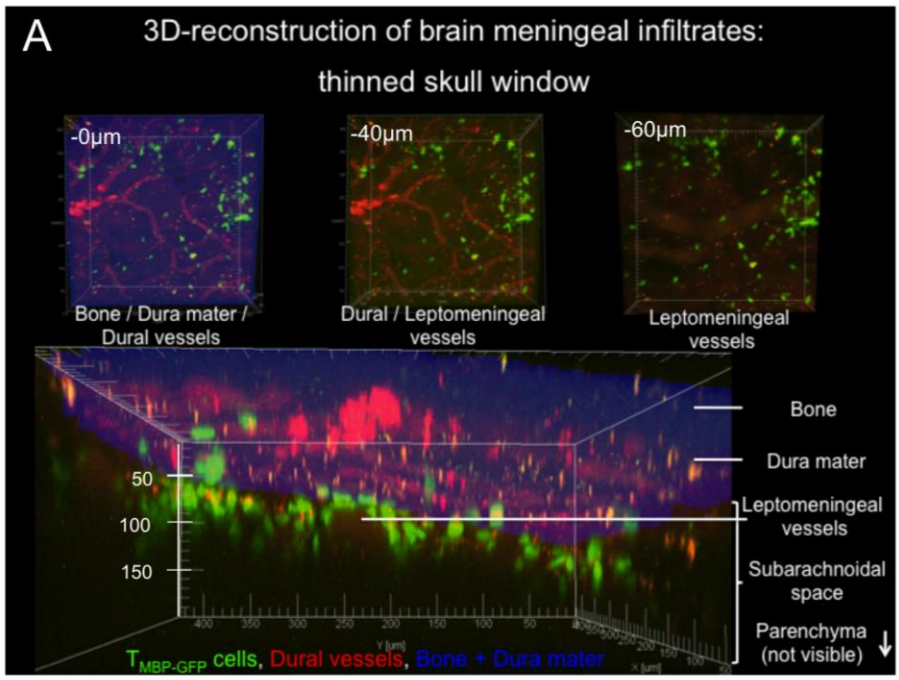
A
3D-reconstruction of brain meningeal infiltrates:
thinned skull window
-0µm
-40µm
-60µm
Bone / Dura mater / Dural vessels
Dural / Leptomeningeal vessels
Leptomeningeal vessels
Bone
Dura mater
Leptomeningeal vessels
Subarachnoidal space
Parenchyma (not visible)
50
100
150
T MBP-GFP cells, Dural vessels, Bone + Dura mater

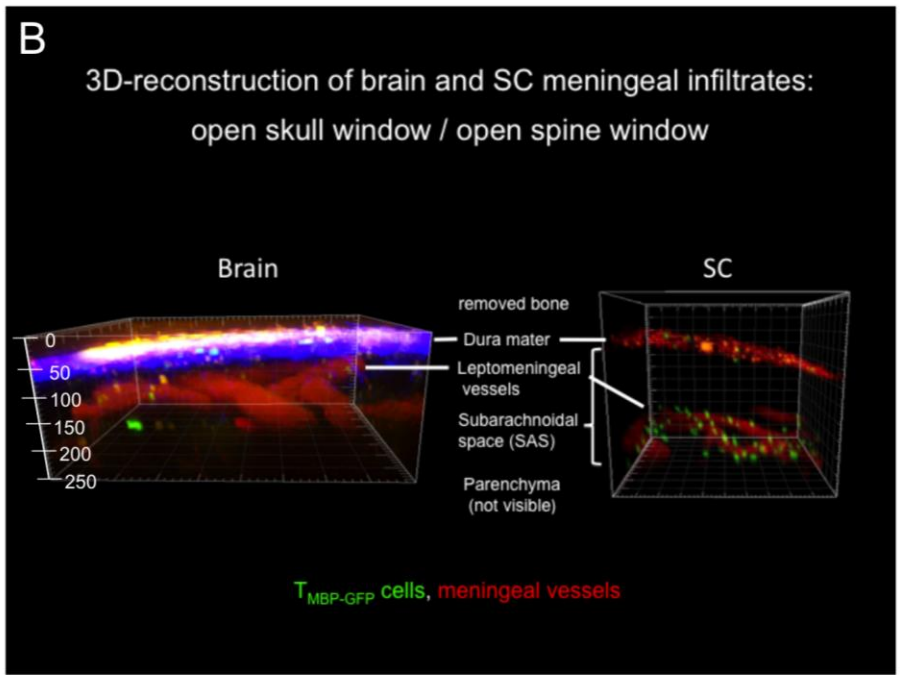
B
3D-reconstruction of brain and SC meningeal infiltrates:
open skull window / open spine window
Brain
SC
removed bone
Dura mater
Leptomeningeal vessels
Subarachnoidal space (SAS)
Parenchyma (not visible)
0
50
100
150
200
250
T MBP-GFP cells, meningeal vessels

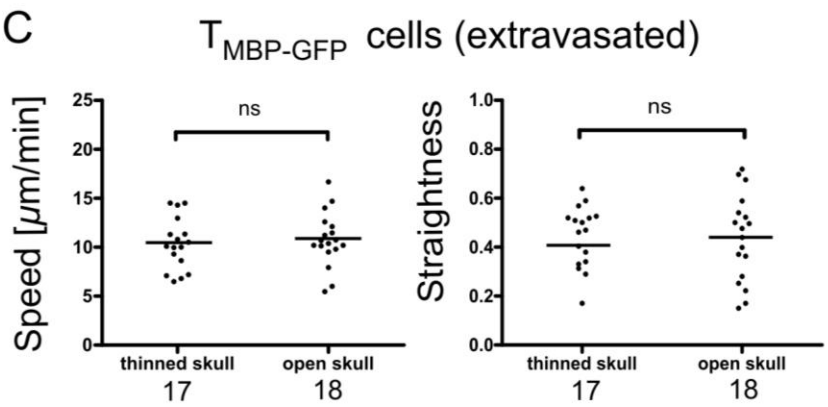
C
T MBP-GFP cells (extravasated)
Speed [µm/min]
ns
thinned skull
open skull
17
18
Straightness
ns
thinned skull
open skull
17
18

Figure 3.17 Establishment and comparison of two cranial window types for two-photon live imaging of effector T cell motility behaviour in brain leptomeninges. Two cranial windows for intravital 2P-LSM were established and tested for their functionality and short-term influence on effector T cell motility behaviour. **(A)** The less invasive thinned skull window is limited in imaging depth. An imaging z-stack of brain leptomeninges was acquired through the thinned skull window. The z- stack was analysed with the Imaris software. Picture 1 (upper row, level -0 µm) shows the top view of the z-stack (blue, bone + dura mater (second harmonic generation signal); red, underlying dural vessels and leptomeningeal vessels; green, $T_{MBP\text{-}GFP}$ cell infiltrates). In picture 2 (upper row, level -40 µm) the bone was virtually removed by cutting off the upper layers of the z-stack (red, dural vessels (bright red signal) and underlying leptomeningeal vessels (pale red); green, $T_{MBP\text{-}GFP}$ cell infiltrates). In addition, in picture 3 (upper row, level -60 µm) the dura mater was virtually removed by further cutting off the upper levels of the z-stack. The leptomeningeal vessels are only visible in pale red (green, $T_{MBP\text{-}GFP}$ cell infiltrates). In the bottom row a 3D picture of the imaging stack was constructed. The deeper portion of the leptomeningeal vessels and deeper T cell infiltrates are not displayed because of insufficient imaging depth. **(B)** 3D reconstructions of brain and spinal cord after open window preparation. The open skull window allows the display of descending leptomeningeal vessels and deeper $T_{MBP\text{-}GFP}$ cell infiltrates. The three-dimensional reconstruction of the SC was adapted from (Bartholomäus et al., 2009). Blue, second harmonic generation signal; red, blood vessels stained by Dextran Texas Red; green, $T_{MBP\text{-}GFP}$ cell infiltrates; GFP, green fluorescent protein. **(C)** Comparison of the motility parameters track speed and track straightness of extravasated T cells imaged through the thinned skull and open skull cranial window. The displacement of tracked cells divided by the path length is indicated as straightness (a value of one means completely straight and directed movement). Dots represent the average value of individually tracked cells. Lines indicate the average value of all tracked cells. Data include the analysis of 17 or 18 $T_{MBP\text{-}GFP}$ cells. Statistical significance was determined by the Man Whitney test. ns, not significant; *P < 0.05, **P < 0.01, ***P < 0.001, ****P < 0.

3.9.2 Motility behaviour of effector $T_{MBP\text{-}GFP}$ and $T_{\beta Syn\text{-}GFP}$ cells in brain and SC leptomeninges

In order to characterize the motility behaviour of effector T cells reactive against either myelin or neuronal antigen in the leptomeninges of brain and SC during ptEAE, both compartments were imaged in three dimensions by 2P-LSM over time. An example of the track analysis of GFP-positive effector T cells is shown for $T_{\beta Syn\text{-}GFP}$ cells in the leptomeninges of the brain in figure 3.18.

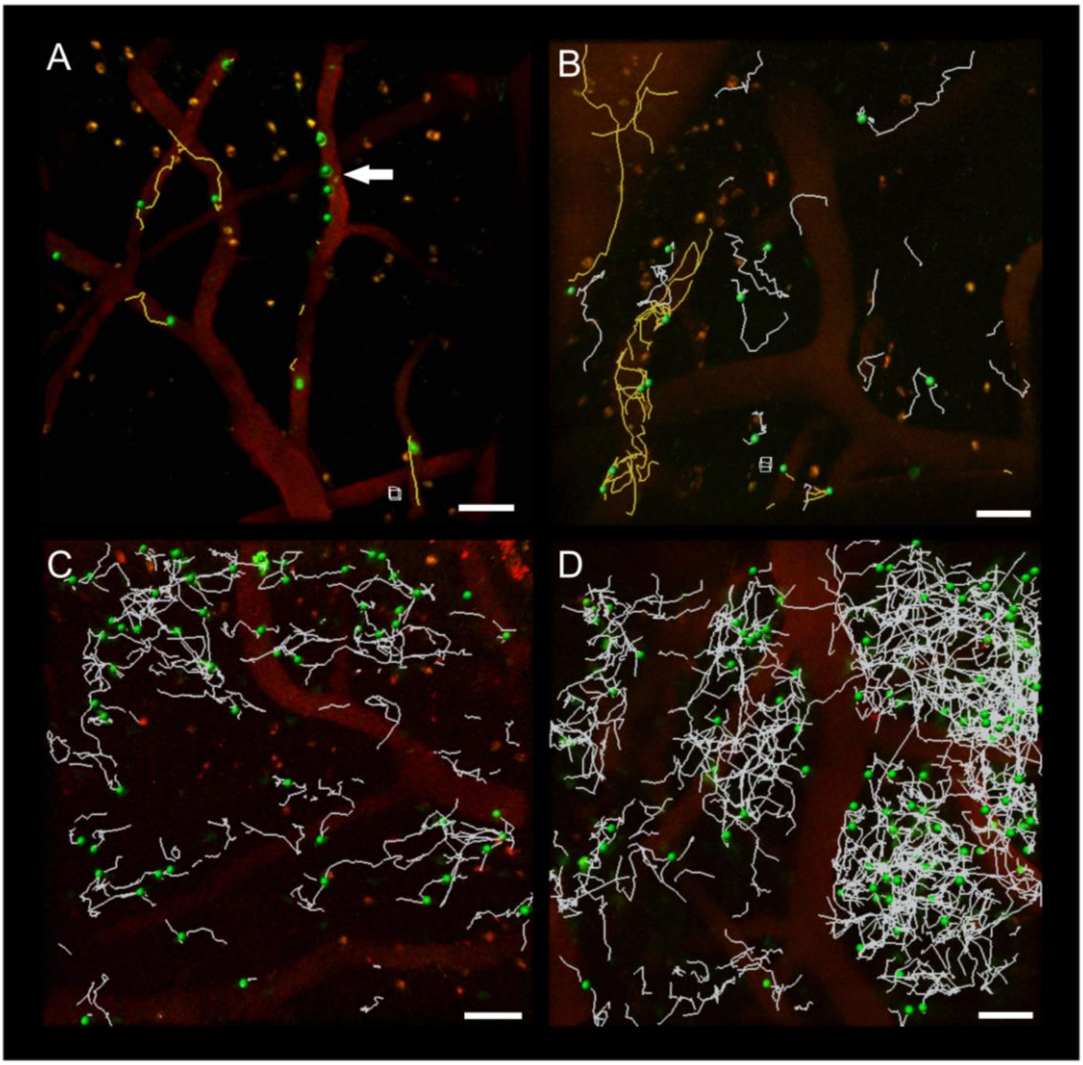

Figure 3.18 Real-time imaging of the motility behaviour of effector $T_{\beta Syn\text{-}GFP}$ cells in the brain leptomeninges. 3D time-lapse movies were acquired via intravital 2P-LSM during the preclinical **(A-B)** and clinical phase **(C-D)** of EAE induced by i.v. transfer of $T_{\beta Syn\text{-}GFP}$ cells. Each movie was recorded for 32 min and analysed by the Imaris software. Green, $T_{\beta Syn\text{-}GFP}$ cells; red, leptomeningeal vessels labelled by i.v. injection of Dextran Texas Red; white, extravasated T cell trajectories; yellow, intraluminal T cell trajectories. Note that the first incoming $T_{\beta Syn\text{-}GFP}$ cells **(A)** are located exclusively in the leptomeningeal vessels where they show a crawling (yellow trajectories) or a rolling behaviour (single green dots, arrow). Some hours later a part of the cells starts to extravasate **(B, white trajectories)**. At the beginning of the clinical symptoms **(C)** most of the effector T cells are extravasated. Some hours later the number of extravasated T cells increased drastically **(D)**. Scale bar: 50 µm.

3.9.3 Analysis of the motility behaviour of effector $T_{MBP\text{-}GFP}$ and $T_{\beta Syn\text{-}GFP}$ cells during the intraluminal phase

Previous studies of our group showed that in ptEAE effector $T_{MBP\text{-}GFP}$ cells display a characteristic motility behaviour upon reaching the leptomenigeal vessels of the SC at the

onset of the disease. The effector T cells crawl along the intraluminal surface of the blood vessels (72 % of intraluminal cells) before extravasation. Only a minor fraction of intraluminal T cells (28 %) roll along the vessel wall (fig. 3.19 A and Bartholomäus et al., 2009). In order to assess whether this behaviour is specific for effector T cells in leptomeningeal vessels of the SC or in general hold true in any CNS compartment during MBP-induced ptEAE, the intraluminal crawling behaviour of $T_{MBP\text{-}GFP}$ cells in brain meningeal vessels was analysed. MBP-specific T cells, which arrive in the leptomeningeal vessels, show the typical vessel-associated crawling behaviour. Quantification of rolling and crawling effector $T_{MBP\text{-}GFP}$ cells in the subarachnoidal vessels of the brain revealed that rolling T cells (59 %) outnumber crawling T cells (41 %) (fig. 3.19 A).

Subsequently, the motility behaviour of the intraluminal $T_{MBP\text{-}GFP}$ cells was compared to the one of $T_{\beta Syn\text{-}GFP}$ cells. Interestingly, in animals affected by βSyn-induced ptEAE most of the effector T cells were rolling (77 % or 87 %) in the subarachnoidal vessels both in the brain and the SC. Only 23 % (brain) or 13 % (SC) of effector T cells crawled along the blood vessel wall (fig. 3.19 B). In the early intraluminal phase (fig. 3.18 A) the rolling T cell phenotype was more pronounced than in the late intraluminal phase (indicated in fig. 3.18 B, quantification not shown).

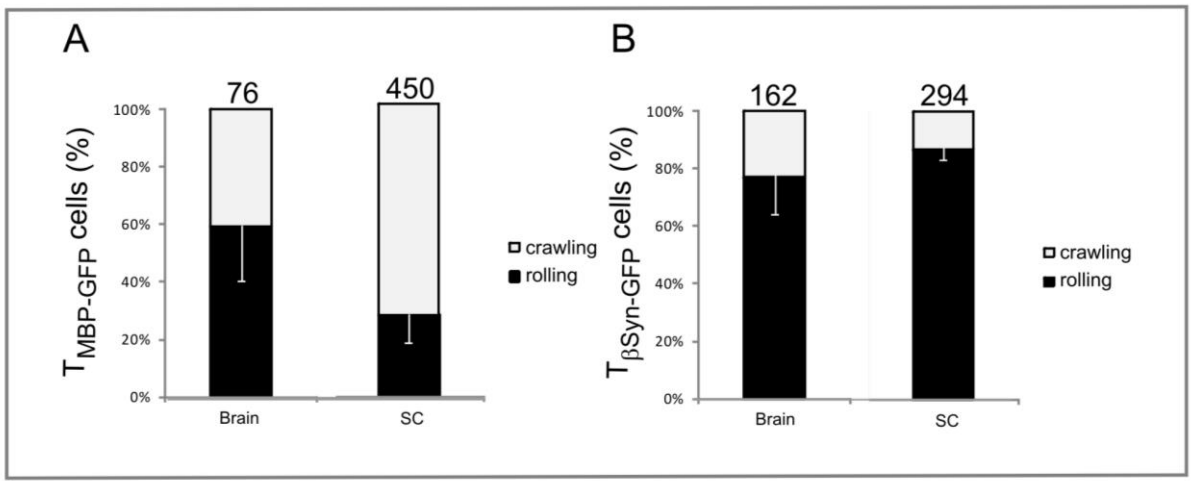

Figure 3.19 Quantification of rolling and crawling effector T cells within CNS leptomeningeal vessels. $T_{MBP\text{-}GFP}$ cells and $T_{\beta Syn\text{-}GFP}$ cells were used to induce ptEAE in Lewis rats. The leptomeninges of the brain and the SC were imaged during the intraluminal phase of effector T cells (just before disease onset) via 2P-LSM. The bar diagrams show the percentage of $T_{MBP\text{-}GFP}$ cells **(A)** or $T_{\beta Syn\text{-}GFP}$ cells **(B)** rolling (black) or crawling (grey) in the vascular beds of brain and SC leptomeninges. The number of analysed cells is indicated at the top of the bars. (Data in (A) (right bar) were kindly provided by Christian Schläger, Department of Neuroimmunology, Institute for Multiple Sclerosis Research, University of Göttingen). Average and SD are depicted.

3.9.4 Analysis of the intraluminal crawling phenotype of $T_{MBP\text{-}GFP}$ cells and $T_{\beta Syn\text{-}GFP}$ cells in the leptomeningeal vessels of brain and SC.

In order to learn if different crawling characteristics could justify the different pattern of inflammation that was observed, the crawling behaviour of $T_{MBP\text{-}GFP}$ and $T_{\beta Syn\text{-}GFP}$ cells was analysed in the meningeal vessels of brain and SC at the onset of the clinical symptoms (fig. 3.20). In the brain meninges a generally low number of intraluminal $T_{MBP\text{-}GFP}$ cells was detected (fig. 3.22 A). The MBP-specific T cells in the leptomeningeal vessels of the brain crawled at a higher speed and more straight along the vessel wall than the ones in the SC (fig. 3.20 A).

During $T_{\beta Syn\text{-}GFP}$ cell-induced ptEAE more T cells were detected in brain meninges compared to MBP-induced EAE at the onset of the disease (fig. 3.22 A and fig. 3.23 A). Similar to what was observed for MBP-specific T cells, $T_{\beta Syn\text{-}GFP}$ cell trajectories were straighter in the brain vessels than in the SC, but the cell speed in the two compartments was similar (fig. 3.20 B and tab. 3.3). Finally, we compared the crawling parameters of MBP- and βSyn-specific T cells in the vessels of the two CNS compartments: No differences in the analysed parameters were detectable in the brain meningeal vessels, whereas $T_{MBP\text{-}GFP}$ cells were faster and straighter than $T_{\beta Syn\text{-}GFP}$ cells in the SC leptomeningeal vessels (table 3.3).

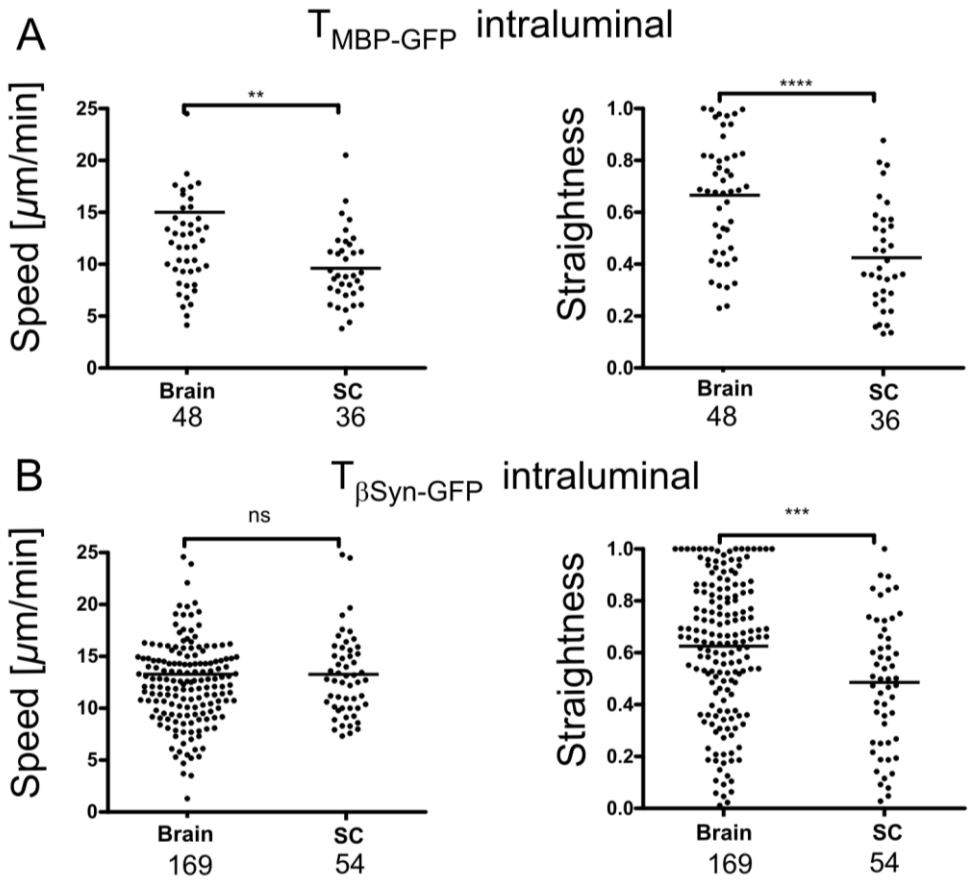

Figure 3.20 Crawling behaviour of intraluminal $T_{MBP\text{-}GFP}$ and $T_{\beta Syn\text{-}GFP}$ cells in the leptomeningeal vessels of the brain and the SC at the onset of inflammation. EAE was induced by transfer of $T_{MBP\text{-}GFP}$ cells or $T_{\beta Syn\text{-}GFP}$ cells to Lewis rats. Intraluminal crawling of the effector T cells in CNS vessels was imaged via 2P-LSM. Paths of the T cells were tracked. The locomotion parameters track speed and track straightness are shown. The displacement of tracked cells divided by the path length is indicated as straightness (a value of 1 means completely straight and directed movement). Dots represent the average value of individually tracked cells. Lines indicate average value of all tracked cells. Data include the analysis of 48 and 36 $T_{MBP\text{-}GFP}$ or 169 and 54 $T_{\beta Syn\text{-}GFP}$ cells in the brain and spinal cord, respectively. T cells from three independent experiments were included in the analysis. Statistical significance was determined by the Man Whitney test. ns, not significant; *P < 0.05, **P < 0.01, ***P < 0.001, ****P < 0.

Table 3.3 Comparison of motility parameters of intraluminal $T_{MBP\text{-}GFP}$ and $T_{\beta Syn\text{-}GFP}$ cells in the CNS compartments at disease onset

	Brain (meninges)		**Significance**	**SC (meninges)**		**Significance**
Cell type	**$T_{MBP\text{-}GFP}$ cells**	**$T_{\beta Syn\text{-}GFP}$ cells**		**$T_{MBP\text{-}GFP}$ cells**	**$T_{\beta Syn\text{-}GFP}$ cells**	
Speed (µm/min)	14.9 ± 12.16	13.1 ± 5.79	ns	9.65 ± 3.65	13.3 ± 4.19	***
Straightness	0.66 ± 0.23	0.62 ± 0.27	ns	0.42 ± 0.20	0.48 ± 0.25	ns

Mean ± s.d. are shown. Statistical significance was determined by the Man Whitney test. ns, not significant; *P < 0.05; **P < 0.01; ***P < 0.001; ****P < 0.

3.9.5 Motility behaviour of motile extravasated effector $T_{MBP\text{-}GFP}$ and $T_{\beta Syn\text{-}GFP}$ cells in the leptomeninges

After diapedesis $T_{MBP\text{-}GFP}$ cells mainly crawl on the abluminal surface of the leptomeningeal vessels getting in contact with perivascular phagocytes. Later they diffusely infiltrate the meningeal area (Bartholomäus et al., 2009). In order to investigate if the same step-wise invasion was detectable in $T_{\beta Syn\text{-}GFP}$ cells, their distribution in the leptomeningeal areas was analysed by 2P-LSM during ptEAE (fig. 3.23 B). Similar to $T_{MBP\text{-}GFP}$ cells (fig. 3.22 B), $T_{\beta Syn\text{-}GFP}$ cells accumulated in the perivascular areas of the SC vessels just after extravasation and some hours later they spread all over the meningeal plane (fig. 3.23 B right picture). Surprisingly, the perivascular phase was never observed in the leptomeningeal area of the brain independently of T cell antigen-specificity. This might be due to the lack of perivascular phagocytes in the brain meninges, which would appear as red dots in close proximity to the

vessels (fig. 3.22 B left picture and 3.23 B left picture). A clear quantitative difference between the two cells types was observed: infiltration of $T_{MBP\text{-}GFP}$ cells into the leptomeningeal area during ptEAE was low in the brain and very pronounced in the SC (fig. 3.22 C). During βSyn-induced ptEAE a dominant infiltration into brain leptomeninges was detected (fig. 3.23 C).

The motility pattern of non-vessel-associated motile effector T cells in the leptomeningeal areas of the brain and SC was analysed. Effector T cells of both specificities move with similar speed in both compartments of the CNS at all analysed time points (fig. 3.21). When the meningeal infiltration increased, $T_{\beta Syn\text{-}GFP}$ cells virtually disappeared from the leptomeninges and could be found in the parenchyma (fig. 3.24). $T_{MBP\text{-}GFP}$ cells remained in the brain leptomeninges during the entire ptEAE course.

Table 3.4 Comparison of motility parameters of extravasated $T_{MBP\text{-}GFP}$ and $T_{\beta Syn\text{-}GFP}$ cells in the CNS compartments at disease onset

	Brain (meninges)		**Significance**	**SC (meninges)**		**Significance**
Cell type	**$T_{MBP\text{-}GFP}$ cells**	**$T_{\beta Syn\text{-}GFP}$ cells**		**$T_{MBP\text{-}GFP}$ cells**	**$T_{\beta Syn\text{-}GFP}$ cells**	
Speed (µm/min)	10.7 ± 2.38	8.22 ± 1.81	***	10.3 ± 1.60	10.3 ± 1.67	ns
Straightness	0.43 ± 0.18	0.42 ± 0.16	ns	0.44 ± 0.15	0.50 ± 0.18	ns

Mean ± s.d. are shown. Statistical significance was determined by the Man Whitney test. ns, not significant; *P < 0.05; **P < 0.01; ***P < 0.001; ****P < 0.

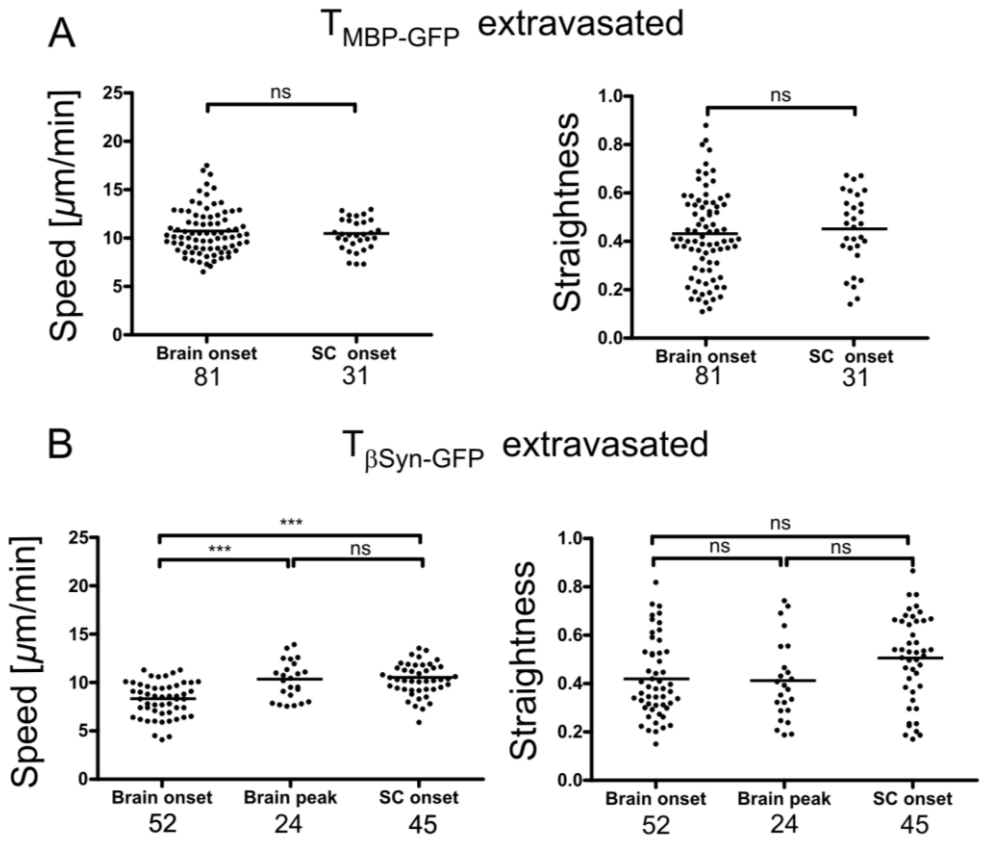

Figure 3.21 Crawling behaviour of motile extravasated $T_{MBP\text{-}GFP}$ and $T_{\beta Syn\text{-}GFP}$ cells in the leptomeningeal area of brain and SC. EAE was induced by transfer of $T_{MBP\text{-}GFP}$ cells or $T_{\beta Syn\text{-}GFP}$ cells to Lewis rats. The crawling of extravasated effector T cells was imaged via 2P-LSM. Afterwards the T cell paths were tracked. The locomotion parameters track speed and track straightness are shown for $T_{MBP\text{-}GFP}$ cells **(A)** and $T_{\beta Syn\text{-}GFP}$ cells **(B)**. The displacement of tracked cells divided by the path length is indicated as straightness (a value of 1 means completely straight and directed movement). Dots represent the average value of individually tracked cells. Lines indicate average value of all tracked cells. T cells from several independent experiments were included in the analysis and the total number of analysed cells is indicated for each graph. Statistical significance was determined by the Man Whitney test (upper graphs) or the Kruskal-Wallis test (lower graphs). ns, not significant; *P < 0.05, **P < 0.01, ***P < 0.001, ****P < 0.

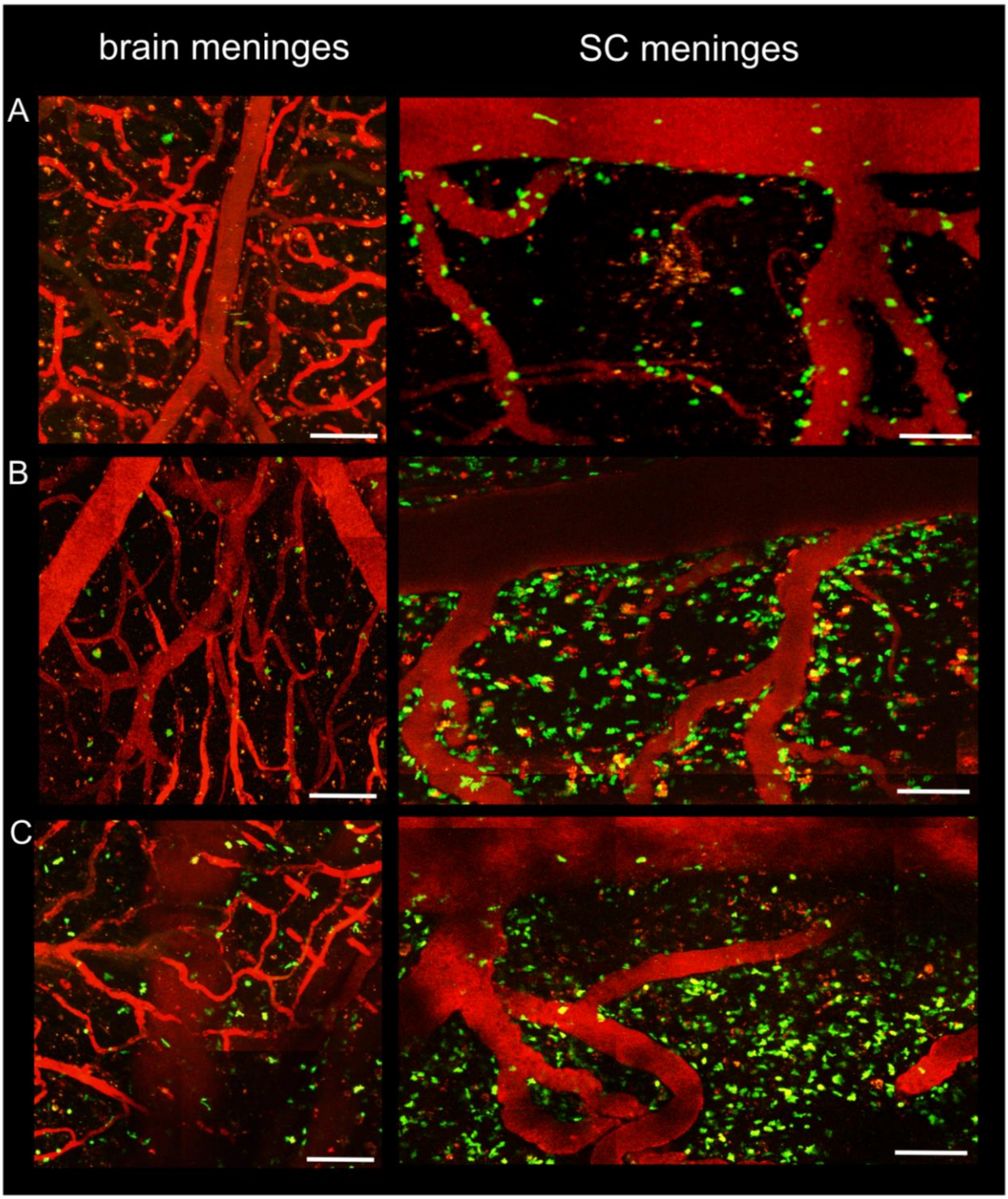

Figure 3.22 Time-lapse analysis of $T_{MBP\text{-}GFP}$ cell invasion in the leptomeninges of the CNS. Overview pictures composed of individual z-stack scans of the meninges of the parietal cortex (left) and the dorsal SC (right) acquired by intravital 2P-LSM. Red thread-like structures, dural and leptomeningeal vessels of the brain (left) and leptomeningeal vessels of the SC (right) labelled by intravenous injection of Dextran Texas Red; red dots, APCs labelled by intrathecal injection of Dextran Texas Red; green, $T_{MBP\text{-}GFP}$ cells. **(A)** At the onset of meningeal inflammation effector T cells enter the leptomeningeal vessels. The number of invading effector T cells is much higher in SC vessels (right) compared to brain vessels (left). **(B)** After an intraluminal phase effector T cells extravasate and accumulate at the abluminal side of leptomeningeal vessels of the dorsal SC. They can be found in close proximity to perivascular APCs (right). In the parietal cortex T cells extravasate and directly distribute in the leptomeningeal area. No perivascular APCs are detected (left). **(C)** The leptomeninges

of the dorsal SC harbour a massive number of effector $T_{MBP\text{-}GFP}$ cells (right). In the same phase the number of effector $T_{MBP\text{-}GFP}$ cells is remarkably lower in the leptomeninges of the parietal cortex (left). Scale 100 µm.

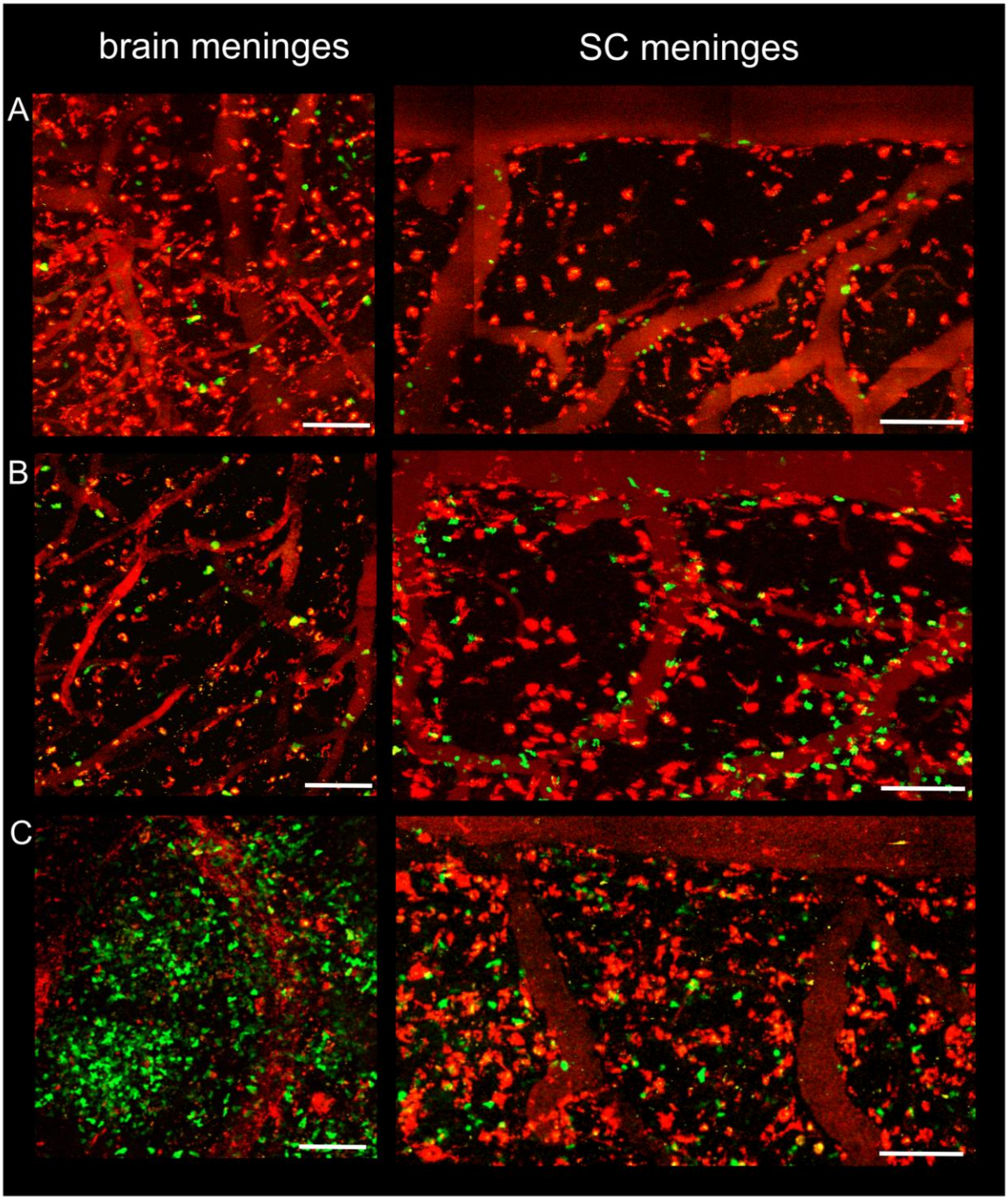

Figure 3.23 Time-lapse analysis of $T_{\beta Syn\text{-}GFP}$ cell invasion in the leptomeninges of the CNS. Overview pictures composed of individual z-stack scans of the meninges of the parietal cortex (left) and the dorsal SC (right) acquired by intravital 2P-LSM. Red thread-like structures, dural and leptomeningeal vessels of the brain (left) and leptomeningeal vessels of the SC (right) labelled by intravenous injection of Dextran Texas Red; red dots, APCs labelled by intrathecal injection of Dextran Texas Red; green, $T_{\beta Syn\text{-}GFP}$ cells. **(A)** At the onset of meningeal inflammation effector T cells are predominantly located in the leptomeningeal vessels. The number of invading effector T cells seems to be similar in SC (right) and brain vessels (left). **(B)** After an intraluminal

phase effector T cells extravsate and accumulate at the abluminal side of leptomeningeal vessels of the dorsal SC. They can be found in close proximity to perivascular APCs (right). In the parietal cortex T cells extravasate and directly start to invade the leptomeninges. Perivascular APCs are lacking (left). **(C)** At the peak of the disease the leptomeninges of the parietal cortex are infiltrated massively by effector $T_{\beta Syn\text{-}GFP}$ cells (left). At the same time point in the disease, the number of effector $T_{\beta Syn\text{-}GFP}$ cells seemed to be lower in the leptomeningeal areas of the dorsal SC (right). Scale 100 µm.

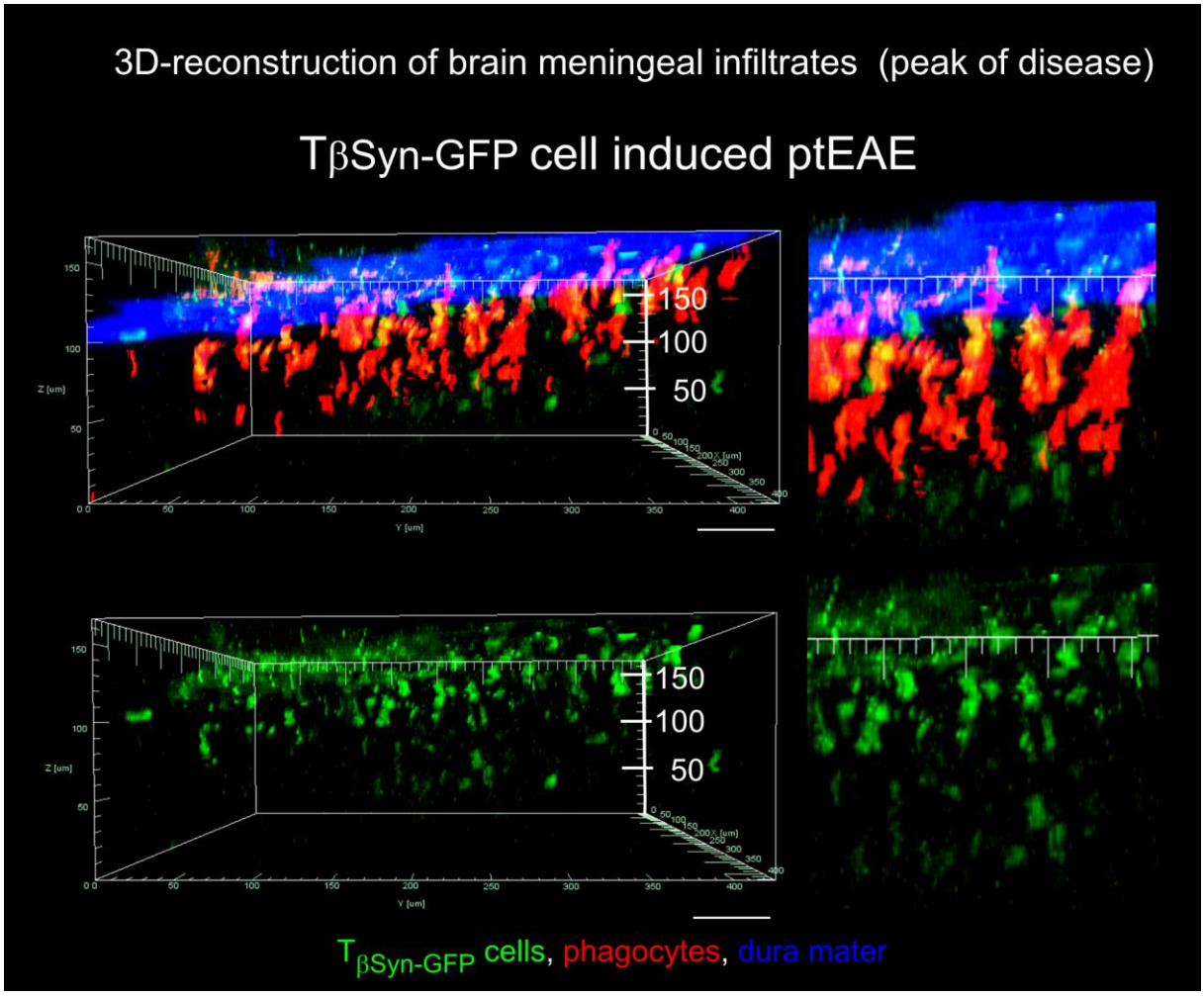

Figure 3.24 Effector $T_{\beta Syn\text{-}GFP}$ cells migrate deeper into the leptomeningeal area during meningeal inflammation. A z-stack of scans of the parietal cortex leptomeninges was acquired via intravital 2P-LSM and reconstructed in 3D. $T_{\beta Syn\text{-}GFP}$ cells have started to migrate from the superior level of the leptomeningeal area to the parenchyma. Some $T_{\beta Syn\text{-}GFP}$ cells passed the layer of leptomeningeal APCs and reached an infiltration depth of 170 µm. Blue, dura mater (second harmonic generation signal); green, $T_{\beta Syn\text{-}GFP}$ cells; red, APCs labelled by intrathecal injection of Dextran Texas Red.

3.10 Direct visualisation of the activation of effector T cells *in situ* at single cell level

In order to investigate if the re-activation of the antigen-specific T cells could also take place deep in the CNS parenchyma, T_{MBP} and $T_{\beta Syn}$ cells, which express the regulatory subunit of the transcription factor "nuclear factor of T cell activation" (NFAT) together with YFP were used to detect T cell activation. Dr. Lodygin (Department of Neuroimmunology, Institute for Multiple Sclerosis Research, University of Göttingen) established a NFAT-sensor and MBP-specific T cells expressing NFAT-YFP ($T_{MBP\text{-}NFAT\text{-}YFP}$ cells). He demonstrated *in vitro* that the translocation of YFP-labelled NFAT occurs shortly after T cell activation. A nuclear NFAT signal was already detectable 3 min after the activation of the T cells with anti-rat-CD3 antibodies *in vitro* (Lodygin et al., in press). *Ex vivo* quantification of $T_{MBP\text{-}NFAT\text{-}YFP}$ cells with nuclear NFAT isolated from the SC of a ptEAE-affected animal was carried out by Dr. Lodygin while $T_{MBP\text{-}NFAT\text{-}YFP}$ cell activation events in the brain of these animals were quantified as part of this thesis. Moreover, βSyn-specific $T_{NFAT\text{-}YFP}$ cells were established and tested *in vitro* for the effective translocation of NFAT-YFP after activation with APCs and the βSyn peptide. Already 1 h after the start of the co-culture an increase in the number of $T_{\beta Syn\text{-}NFAT\text{-}YFP}$ cells with nuclear NFAT was detected (fig. 3.25 A and B). After 2-3 h the highest level of NFAT translocation was detected (approx. 70-80 % of $T_{\beta Syn\text{-}NFAT\text{-}YFP}$ cells showed a nuclear YFP signal). After a plateau phase a decrease in $T_{\beta Syn\text{-}NFAT\text{-}YFP}$ cells containing nuclear NFAT-YFP was detected 36 h after the start of the co-culture (fig. 3.25 A and B).

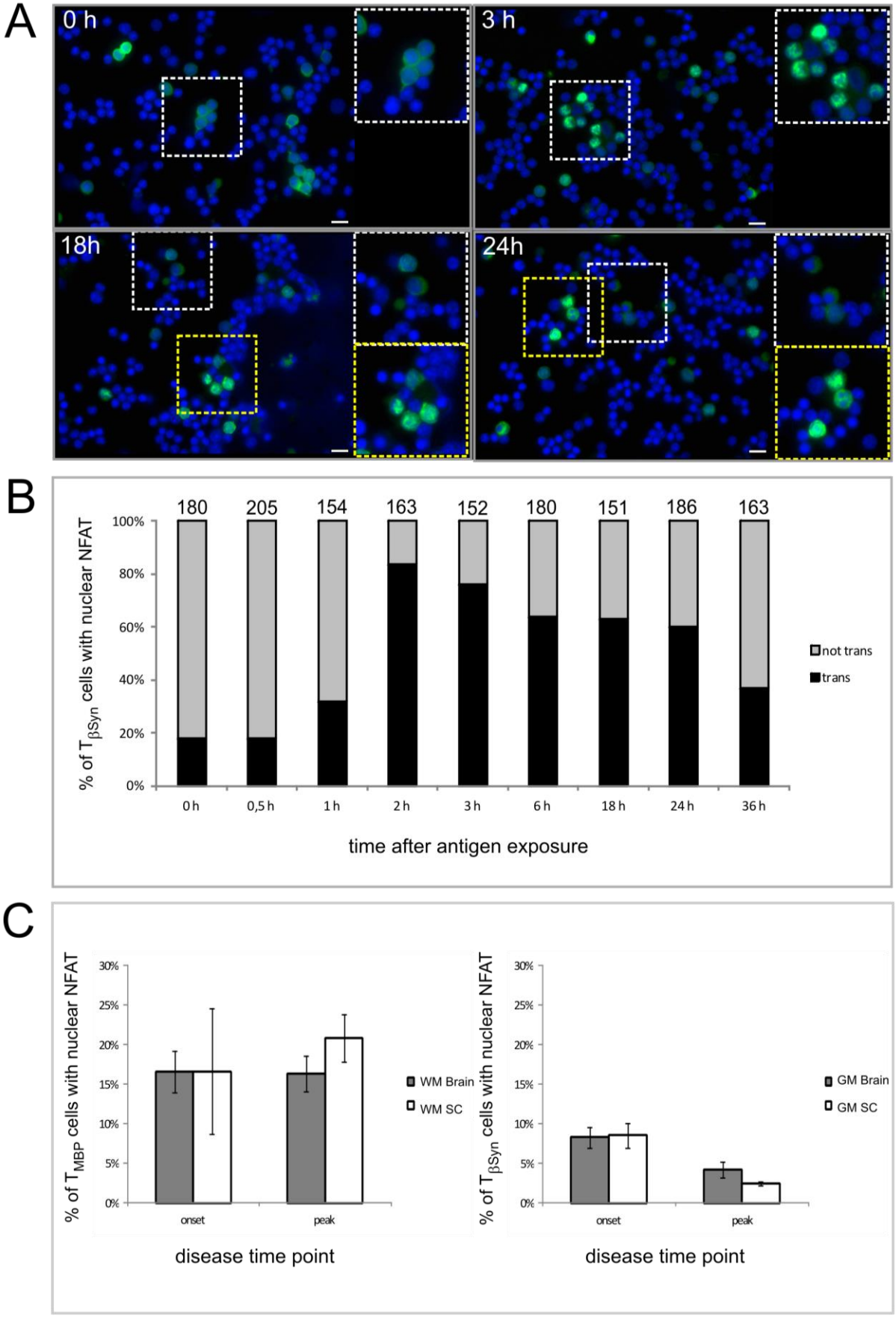
A
0 h
3 h
18h
24h
B
180
205
154
163
152
180
151
186
163
100%
80%
60%
40%
20%
0%
% of T βSyn cells with nuclear NFAT
not trans
trans
0 h
0,5 h
1 h
2 h
3 h
6 h
18 h
24 h
36 h
time after antigen exposure
C
30%
25%
20%
15%
10%
5%
0%
% of T MBP cells with nuclear NFAT
WM Brain
WM SC
onset
peak
disease time point
% of T βSyn cells with nuclear NFAT
GM Brain
GM SC
onset
peak
disease time point

Figure 3.25 Direct visualization of effector $T_{MBP\text{-}NFAT\text{-}YFP}$ or $T_{\beta Syn\text{-}NFAT\text{-}YFP}$ cell activation *in vitro* and *ex vivo* at single cell level. (A and B) $T_{\beta Syn\text{-}NFAT\text{-}YFP}$ cells were incubated with APCs and re-stimulated with the $T_{\beta Syn}$ peptide. After 0, 0.5, 1, 2, 3. 6, 18, 24 and 36 h T cells were fixed and the cell nuclei were stained with DAPI. $T_{\beta Syn\text{-}NFAT\text{-}YFP}$ cells were analysed by fluorescence microscopy. **(A)** Representative time points 0, 3, 18 and 24 h after re-stimulation are shown. In the control situation (0 h after re-stimulation) most T cells showed a cytosolic NFAT-YFP signal while the nuclei are NFAT-YFP-negative. 2 and up to 3 h after re-stimulation, the highest number of T cells with nuclear NFAT-YFP was detected. Afterwards, the number decreased again (18 and 24 h). Scale bars: 10 µm. **(B)** Number of T cells with nuclear NFAT were counted and are shown in a bar diagram as percentage of $T_{\beta Syn}$ cells with nuclear NFAT. Not trans (NFAT not translocated), grey bars; trans (NFAT translocated), black bars). On the top of the bars the number of analysed cells is indicated. **(C)** Histological analysis of $T_{MBP\text{-}NFAT\text{-}YFP}$ cell and $T_{\beta Syn\text{-}NFAT\text{-}YFP}$ cell activation during ptEAE in brain and SC tissue. Number of $T_{MBP\text{-}NFAT\text{-}YFP}$ cells or $T_{\beta Syn\text{-}NFAT\text{-}YFP}$ cells with nuclear NFAT were counted in WM or GM respectively and are shown in a bar diagram as percentage of cells with nuclear NFAT. Total number of $T_{MBP\text{-}NFAT\text{-}YFP}$ cells analysed: onset: brain n = 392, SC n =313, peak: brain n = 456, SC n = 274; Total number of $T_{\beta Syn\text{-}NFAT\text{-}YFP}$ cells analysed: onset: Brain n = 497, SC n = 556, peak: Brain n = 1154, SC n = 699.

Furthermore, $T_{\beta Syn\text{-}NFAT\text{-}YFP}$ cells were used *in vivo* to induce βSyn-specific ptEAE. After transfer of $T_{\beta Syn\text{-}NFAT\text{-}YFP}$ cells to Lewis rats, the animals developed a monophasic paralytic disease similar to the one observed after transfer of $T_{\beta Syn\text{-}GFP}$ cells (data not shown and fig. 3.3 C) and the effector T cells exhibited a similar CNS homing pattern (data not shown). For further analysis, $T_{MBP\text{-}NFAT\text{-}YFP}$ and $T_{\beta Syn\text{-}NFAT\text{-}YFP}$ cell-injected animals were sacrificed at the onset and peak of the disease. Brain and SC tissue sections of these animals were examined for NFAT translocation events. It was previously shown in this thesis that the infiltration of βSyn-specific T cells in the CNS parenchyma is limited to GM areas and MBP-specific T cells mainly infiltrate the WM of the brain (see chapters 3.3 and 3.4). Therefore, the analysis of NFAT translocation in the effector T cells was limited to these areas of interest. Effector $T_{\beta Syn\text{-}NFAT\text{-}YFP}$ cells showed a higher percentage of nuclear NFAT at the onset (approx. 8.3 % in the brain and 8.6 % in the SC) compared to the peak of the disease (approx. 4.2 % in the brain and 2.4 % in the SC) in brain and SC grey matter (fig. 3.25 C). Effector $T_{MBP\text{-}NFAT\text{-}YFP}$ cells showed a similar percentage (approx. 16.3-20.9 %) of T cells with nuclear NFAT at the onset and peak of the disease in brain and SC white matter. During $T_{\beta Syn\text{-}GFP}$ cell-induced ptEAE the percentage of T cells containing nuclear NFAT was generally lower compared to animals affected by MBP-induced ptEAE.

4. Discussion

4.1 Characterisation of infiltration pattern and tissue distribution of encephalitogenic T cells in GM and WM of different milieus of the CNS

The aim of this thesis was to analyse the autoimmune responses in distinct milieus of the CNS and to determine the crucial factor(s) for the homing pattern of effector T cells specific for either grey or white matter antigens into the target organ.

The neuronal antigen β-synuclein$_{93-111}$ peptide (βSyn) and the classical myelin antigen MBP were tested for their potential to induce EAE. For this purpose, Lewis rats were immunized with MBP or βSyn in complete Freund´s adjuvant. Independently which antigen was used immunized animals developed an EAE with "classical" paralytic disease symptoms, i.e. ascending paresis paralysis (fig. 3.1). In order to investigate the specific role of effector T cells reactive against myelin or neuronal antigens, $T_{MBP\text{-}GFP}$ cells and $T_{\beta Syn\text{-}GFP}$ cells were established and tested *in vivo* and *in vitro*. Both T cell lines were specific for their appropriate antigen (fig. 3.2 B and 3.3 B), showed the TCR^+ $CD4^+$ T cell phenotype and up-regulated the surface activation markers OX40 and IL-2R after re-stimulation (fig. 3.2 A and 3.3 A). When tested *in vivo* all $T_{MBP\text{-}GFP}$ cell transferred animals and the vast majority of $T_{\beta Syn\text{-}GFP}$ cell transferred animals developed a paralytic monophasic disease with similar disease severity (fig. 3.2 C and 3.3 C). In most $T_{\beta Syn\text{-}GFP}$ cell transferred animals a delay in disease onset and a faster recovery was observed. Due to the fact that β-synuclein is expressed by neurons, it seems possible that after βSyn-specific ptEAE-induction animals might suffer from different neurological symptoms in addition to classical EAE symptoms. In the literature βSyn is described as the only one of 70 CNS-associated new candidate peptides that was able to induce an EAE-like phenotype in Lewis rats after immunization with the peptide or transfer of non-labelled βSyn-specific T cells (Mor and Cohen, 2006). This was quite surprising considered that β-synuclein lacks a signal peptide and therefore it is considered to be a cytosolic protein (George, 2002). Because neurons themselves do not express MHC class II molecules it remains unclear how the β-synuclein antigen is presented to CD4-positive T cells. Recently it has been shown that α-synuclein, a related member of the same protein family with similar protein structure can be secreted *in vitro* and *in vivo* (Emmanouilidou et al., 2010; 2011); no similar experimental evidence is reported for β-synuclein. In two of the three published studies the induction of EAE with βSyn required a boosting pre-treatment of Lewis rats to induce a severe disease. The animals were submitted to irradiation to disrupt the

BBB or treated with cyclophosphamide, which enhances the autoimmune response prior to immunization (Kela-Madar et al., 2009; Mor et al., 2003). Uncommon cases of EAE were not described. In contrast to previous studies βSyn-specific EAE in this thesis was evoked without pre-treatment. Generally, a classical ascending paralysis was observed. It came as a surprise, though, that 4 animals (of the 139 clinically examined) developed a very uncommon disease phenotype that included upper limb paralysis or hemiparesis. It cannot be excluded that the occurrence of further uncommon symptoms was under-estimated. The clinical analysis was limited to motor symptoms that in the rats are generally ascribed to subcortical or SC lesions due to the lack of monosynaptic excitatory cortico-motoneuronal connections (Alstermark et al., 2004). No testing of cortical functions was performed.

None of the three published β-synuclein studies analysed the pathophysiological background of βSyn-mediated EAE in detail. Mor et al. were mainly focussing on the induction of an EAE-like phenotype in the experimental animals, the analysis of disease symptoms and the characterisation of EAE-inducing T cells *in vitro* (Mor et al., 2003; Mor and Cohen, 2006). In addition, the authors showed inflammatory infiltrates in the SC and cerebral cortex of βSyn-immunized animals, but no further detailed analysis was published (Mor et al., 2003). Kela-Madar et al. confirmed the encephalitogenicity of a similar βSyn peptide including the amino acids 92-110 and showed that the immune response to the neuronal antigen can lead to T- and B-cell-mediated autoimmune spreading to epitopes of other neuronal but also myelin antigens (Kela-Madar et al., 2009). In the present study, a detailed analysis of the homing behaviour of both $T_{MBP\text{-}GFP}$ cells and $T_{\beta Syn\text{-}GFP}$ cells during the different ptEAE phases was performed.

Antigen specificity did not influence the effector T cell homing behaviour during the preclinical phase in the peripheral tissues. As previously described for $T_{MBP\text{-}GFP}$ cells (Odoardi et al., 2012) $T_{\beta Syn\text{-}GFP}$ cells first entered the lung and then peaked in spleen and blood just before entering the CNS tissues.

The homing pattern of $T_{MBP\text{-}GFP}$ cells and $T_{\beta Syn\text{-}GFP}$ cells in the CNS tissues was analysed by using 3 different parallel approaches: flow cytometry, 2P-LSM and histology. Histological analyses were performed on decalcified samples in order to keep the meninges intact. 2P-LSM and histological data revealed that $T_{MBP\text{-}GFP}$ cells infiltrated the brain meninges in lower numbers than SC meninges (fig. 3.6 A-C and 3.7 A and B, fig. 3.22); instead flow-cytometry analysis revealed similar numbers of invading $T_{MBP\text{-}GFP}$ cells in both compartments (fig. 3.5 A). It might be reasonable to assume that the T cell number in brain meninges was overestimated during *ex vivo* analysis due to anatomical differences between the 2 compartments. The cranial dura mater is composed of two layers, an inner or meningeal and

an outer or endosteal layer, closely connected together. Instead the spinal dura mater forms a loose sheath around the medulla spinalis: even if it is separated from the arachnoidea by a potential cavity, the subdural cavity, the two membranes are, in fact, in strict contact. As a consequence, during the preparation the cranial dura mater, which contributes significantly to the total meningeal weight, but is only poorly infiltrated by T cells, was removed when the skull was opened. On the other hand, the spinal dura mater, also poorly infiltrated by T cells, was not separated from the leptomeninges.

As expected, in the SC parenchyma the number of $T_{MBP\text{-}GFP}$ cells was higher than in brain as shown both by histology and flow cytometry (fig. 3.8 A, D and E and fig. 3.9 A-C, fig. 3.5 A). This is in line with the general observation that in EAE the brain tissue is less infiltrated by $T_{MBP\text{-}GFP}$ cells and shows lower inflammation (Cross et al., 1993; Pender et al., 1995).

Interestingly, analysis of CNS tissue revealed that $T_{\beta Syn\text{-}GFP}$ cells entered the brain in higher number than $T_{MBP\text{-}GFP}$ cells do (fig. 3.8); moreover, the number of infiltrating cells was similar in brain and SC parenchyma (fig. 3.5).

Several different entry routes of effector T cells in the CNS have been postulated (Ransohoff et al., 2003). According to recent data the choroid plexus could play an important role for effector T cell entry. Indeed in the mouse model, T_H17 cells were postulated to initiate EAE by entering through the choroid plexus via the CCR6-CCL20 axis (Reboldi et al., 2009). In our model the choroid plexus seemed to be irrelevant for effector T cell entry into the brain, because no T_{GFP} cells were found in the plexus epithelium at any time point independently from the antigen specificity (fig. 3.6 D and I or 3.8 D and I). It has been previously shown by our group that both in rat and in mouse ptEAE, effector $T_{MBP\text{-}GFP}$ cells enter the SC tissue through the leptomeningeal vessels (Bartholomäus et al., 2009). Histological analysis of decalcified cryo-sections of animals transferred with MBP- and βSyn-specific T cells revealed that both of these cell types used the same infiltration route into brain parenchyma: at disease onset GFP-positive effector T cells entered the meninges and partially the underlying brain parenchyma. Interestingly, $T_{\beta Syn\text{-}GFP}$ and $T_{MBP\text{-}GFP}$ cells seemed to use different entry sites in the SC: while white matter antigen-specific $T_{MBP\text{-}GFP}$ cells as expected entered from the entire surrounding meninges, $T_{\beta Syn\text{-}GFP}$ cells were mainly found in the meninges adjacent to the dorsal horn (fig. 3.7). Moreover, the cells were located in deep grey matter mainly around parenchymal vessels. Hence the grey matter parenchyma was likely infiltrated directly by these cells.

At the peak of the disease, only few $T_{MBP\text{-}GFP}$ cells were found in the brain parenchyma and were mainly located around the ventricular ependyma and in the white matter regions (fig. 3.8

D and E). In contrast, at the same time point massive $T_{\beta Syn\text{-}GFP}$ cell infiltrates were located in the sub-pial area and deep in the cortical grey matter (fig. 3.8 G and H). As expected, in the SC $T_{MBP\text{-}GFP}$ cells (Kawakami et al., 2005b; Bartholomäus et al., 2009) were distributed not just in the white matter but also in the grey matter; whereas $T_{\beta Syn\text{-}GFP}$ cells infiltrated almost exclusively the grey matter at the peak of the disease.

To my knowledge, the specific and massive distribution of effector $T_{\beta Syn\text{-}GFP}$ cells in the grey matter is unique. Cortical infiltration and preferential involvement of the grey matter are rare in EAE models where the infiltration in general is localized in the SC and mainly in the white matter (Linker and Lee, 2009). The described active EAE models are less suitable to investigate the role of the effector T cells responsible for disease pathogenesis because they do not allow the tracking of the pathogenic effector T cells (Pomeroy et al., 2005; Storch et al., 2006; Huizinga et al., 2008). One of these cortical EAE models is the focal EAE model described by Merkler (Merkler et al., 2006b). In contrast to this study the cortical infiltrations in the present study were not evoked by exogenous manipulation after EAE induction. To my knowledge only one model of passive transfer EAE has been described. In this model, T cells reactive against the neuronal antigen TAG-1 were used for disease induction (Derfuss et al., 2009). The inflammatory infiltrates found in this study were localized in both white matter and grey matter but they were limited to the perivascular areas.

The cortical effector T cell infiltrations in βSyn-induced ptEAE observed in this study resembled the infiltrates found in cortical lesions of early and moreover primary progressive multiple sclerosis patients (Lucchinetti et al., 2011; Choi et al., 2012). Similar to these patients, animals affected by βSyn-specific ptEAE show marked but diffuse meningeal and perivascular meningeal, but also sub-pial infiltration of T cells, which spreads intracortically. Further analysis of CNS tissue will reveal whether secondary recruited inflammatory cells and T cell-induced tissue damage are prominent in this ptEAE model.

4.2 Analysis of the mechanisms that determine effector T cell infiltration and distribution in GM and WM of different CNS milieus

Histological analysis showed that the antigen specificity of effector T cells is important for entry site and distribution of these cells within the CNS. Both tissue-intrinsic properties and cell-dependent factors could justify this observation.

The CNS parenchyma has been described as an immune hostile milieu that induces rapid apoptosis in the incoming effector T cells (Bauer et al., 1998). However, the apoptosis rate

detected by anti-active Caspase-3 antibody staining of both $T_{MBP\text{-}GFP}$ and $T_{\beta Syn\text{-}GFP}$ cells was low at all the examined time points and in all the analysed tissues. Even if there was a general mild increase of apoptosis rate at the peak of the disease, no main differences between the CNS compartments were detected at the same time point.

It is well-known that chemokines play a key role in the immune system by directing the trafficking of immune cells in the different tissues both in a healthy state as well under inflammatory condition (Bromley et al., 2008). It was demonstrated that transmigration of effector T cells across the BBB is chemokine-dependent and therefore the chemokine/chemokine receptor pathway plays an important role in T cell homing into the CNS (reviewed in Holman et al., 2011). CCL19 could be detected by in situ hybridization at the level of the BBB (Alt et al., 2002). In our system the expression of CCL19 was detectable at very low levels in the meninges of brain and SC by QRT-PCR, but there were no remarkable differences between these two compartments (data not shown). Also the expression of the homeostatic chemokine CXCL12 and the pro-inflammatory chemokines CCL5, CXCL9, CXCL10, and CXCL11 in the CNS was analysed via QRT-PCR in naïve animals and during the EAE course. The expression levels of all these chemokines but CXCL12 were very low in naïve animals in all the CNS compartments and increased during the inflammation mirroring the effector T cell infiltration pattern. Conversely, CXCL12 expression was very high in the non-inflamed meningeal tissue both in brain and SC and was down-regulated during inflammation (fig. 3.11). CXCL12 is known to be expressed constitutively in the CNS, especially by endothelial cells of the CNS vasculature (Stumm et al., 2002; Krumbholz et al., 2006). Under non-inflamed conditions this signalling molecule is expressed on the parenchymal surface of CNS endothelial cells and seems to function by repelling CXCR4-expressing leukocytes from the BBB (McCandless et al., 2006; 2008a; 2008b). In MS and EAE re-distribution of CXCL12 from the abluminal side of the CNS microvasculature towards the luminal side was shown (McCandless et al., 2008a; 2008b; Cruz-Orengo et al., 2011). The alteration in the CXCL12 expression correlated with disease severity (McCandless et al., 2008a) and was associated with leukocyte entry (McCandless et al., 2006). However, even if the observed down-regulation of the T cell repellent CXCL12 might promote the entry into the CNS of MBP- or βSyn-specific effector T_{GFP} cells the very similar expression of this molecule in both the meningeal compartments does not justify the different pattern of entry of the effector T cells.

Alternatively, the distinct tissue distribution of $T_{MBP\text{-}GFP}$ and $T_{\beta Syn\text{-}GFP}$ cells could be due to cell-intrinsic properties. Recently it has been shown that after transfer effector T cells have to undergo a complex re-programming of their expression profile by down-regulating their activation and proliferation program and up-regulating an appropriate set of surface molecules (i.e. chemokine receptors and integrins) in the peripheral organs. These phenotypic changes are necessary to allow the effector T cells to overcome the BBB (Odoardi et al., 2012). Just before entering the CNS $T_{MBP\text{-}GFP}$ or $T_{\beta Syn\text{-}GFP}$ cells isolated from blood showed a similar integrin and chemokine receptor expression profile and thereby had the same prerequisites to enter the CNS (fig. 3.12 A). The cells of both specificities strongly expressed VLA-4 which is necessary for effector T cells to first interact shortly with and later to firmly adhere to the vascular epithelial cells of the BBB (Berlin et al., 1995; Vajkoczy et al., 2001; Bartholomäus et al., 2009). LFA-1 expression was lower than VLA-4 expression in both cell types (fig. 3.12 A).

Regarding the chemokine receptor expression profile, a strong expression of CXCR3 and CXCR4 and a lower expression of CCR5, CCR6 by both effector T cell types was detected (fig. 3.12 A). Functional *ex vivo* transmigration analysis performed in parallel revealed that $T_{MBP\text{-}GFP}$ or $T_{\beta Syn\text{-}GFP}$ cells, purified from blood at the onset of the disease, showed a similar preferential chemoattraction to CCL20 (ligand of CCR6) and CXCL11 (ligand of CXCR3), whereas no directional movement versus CXCL12 (ligand of CXCR4) was observed (fig. 3.12 B). The high expression level of CXCR3 in effector T cells is well documented. In several disease models it has been shown that this chemokine receptor plays an essential role in licensing T cell entry into the CNS (Groom and Luster, 2011). In particular in Lewis rat ptEAE it has been shown that CXCR3 blocking by specific monoclonal antibodies strongly reduces disease severity (Sporici and Issekutz, 2010). Also the CCR6/CCL20 axis has been involved in the recruitment of effector T cells at the beginning of the inflammation not just in the choroid plexus (Reboldi et al., 2009) but also in the spinal cord at the fifth lumbar vertebrae: the up-regulation of the CCL20 ligand at this SC level led to infiltration of auto-reactive T cells in the area of chemokine expression (Arima et al., 2012). My data suggest that both these chemokine receptors and the VLA-4 integrin could play a major role in the initial effector T cell entry in the target tissue at the onset of the disease. However, the finding that $T_{MBP\text{-}GFP}$ and $T_{\beta Syn\text{-}GFP}$ cells show the same surface receptor expression pattern just before the entry in the target tissue indicated that other mechanisms determine the different CNS homing pattern of these cells. It was demonstrated that distinct expression of adhesion molecules and chemokine receptors on $T_{MBP\text{-}GFP}$ and $T_{\beta Syn\text{-}GFP}$ cells in the target tissue could not be the

reason of the different topology of the lesions. Independently from the antigen specificity, the T_{GFP} cells isolated from the different CNS compartments during on-going inflammation showed a very similar expression profile of these molecules and a preferential targeted migration towards CXCL11 and CCL20. Moreover, the expression of VLA-4 was higher than LFA-1 expression in T cells of both specificities (fig. 3.13 and 3.14).
Finally, also the hypothesis that a different ratio between T_H1 and T_H17 cells may determine the site of infiltration in the CNS (Stromnes et al., 2008) could be reasonably excluded because $T_{MBP\text{-}GFP}$ and $T_{\beta Syn\text{-}GFP}$ cells showed a very similar cytokine expression profile before entering the CNS (fig. 3.16).

By combining 2P-LSM and functional characterization it has been shown in a previous study that effector T_{MBP} cells enter the SC via the meninges in a step-wise mechanism. The incoming cells first crawl extensively on the intraluminal leptomeningeal endothelium; after diapedesis they scan the outside surface of the vessel wall where they get in contact with local perivascular phagocytes, which are able to present the cognate antigen (Bartholomäus et al., 2009). Consequently, as it was recently demonstrated *in vivo* by using a genetically encoded NFAT biosensor the T cells get locally re-activated in the leptomeninges (Lodygin et al., in press). The level of activation is essential for the T cellular invasion into the parenchyma and it is dependent on antigen availability (Kawakami et al., 2004). It is important to note that the motility parameters of effector T cells during the extravasation steps are related to their activation status: brain-ignorant T_{OVA} cells that are not activated in the CNS tissues crawl faster and for shorter time in the leptomeningeal vessels compared to $T_{MBP\text{-}GFP}$ cells. Moreover, once extravasated they established shorter contacts with meningeal phagocytes. Based on this background I hypothesized that a different antigen distribution and therefore a different activation level could justify the observed divergent infiltration pattern of $T_{MBP\text{-}GFP}$ cells in brain and SC. In order to test this hypothesis, *in vivo* imaging of effector T cells in brain and SC meninges was performed. Whereas the optical window for accessing the lumbar SC had been already established (Odoardi et al., 2007; Bartholomäus et al., 2009), the access window to the parietal cortex had to be established and tested. Interestingly, from an anatomical point of view the two tissues visualized by 2P-LSM showed some remarkable differences: the 3D collagen network identified by second harmonic generation was much more prominent in the SC compared to the brain meninges (not shown). Moreover, whereas numerous local macrophages were detected around the SC meningeal vessels the same perivascular cells were in the brain just sporadically visible. Perhaps this difference in the

phagocyte distribution could justify why no perivascular accumulation of effector T cells was observed in any phase of the disease independently from the antigen-specificity and the level of infiltration (fig. 3.22 and 3.23, left pictures).

2P-LSM imaging of living animals showed that the motility behaviour of effector $T_{MBP\text{-}GFP}$ cells in brain meninges was very different from the motility pattern of the same cells in the SC meninges: during the intravascular phase the percentage of $T_{MBP\text{-}GFP}$ cells crawling on the brain leptomeningeal vessels was lower than in SC vessels (41 % vs. 72 %); moreover, the T cells crawled faster (14.9 μm/min vs. 9.65 μm/min) and in a more straight way (0.66 vs. 0.42), suggesting a reduced activation of the local endothelium in the brain. After diapedesis the effector T cell velocity that is likely to be controlled by cell-intrinsic properties (Lämmermann et al., 2008) was similar in both meningeal compartments (10.7 μm/min vs. 10.3 μm/min). Taken together, the motility data suggest a lower level of activation of effector $T_{MBP\text{-}GFP}$ cells in the brain meninges compared to the SC meninges. Consistent with the hypothesis that the activation level is critical for the further invasion in the parenchyma (Kawakami et al., 2005b), in all the investigated EAE phases the number of $T_{MBP\text{-}GFP}$ cells able to infiltrate the brain meninges was extremely low and no infiltration in the adjacent GM was detectable. The motility data were flanked by functional data. $T_{MBP\text{-}GFP}$ cells sorted from the meninges of both compartments showed a lower level of cytokine expression in the brain meninges compared to SC meninges (fig. 3.16 C). However, this data - even if consistent with the motility data - should be interpreted cautiously. 2P-LSM imaging of the brain was performed on the parietal cortex meninges that surmount grey matter regions whereas effector T cells were sorted from the total meninges that are in contact both with GM and WM areas. Therefore, in order to compare exactly the same meningeal compartment, assessment of the level of activation of T_{MBP} cells has to be performed *in situ* by using the NFAT biosensor.

Functional characterization and 2P-LSM analysis were also performed on $T_{\beta Syn\text{-}GFP}$ cells in the brain and SC meninges. In both CNS compartments, the level of activation of the sorted $T_{\beta Syn\text{-}GFP}$ cells was higher than in the blood indicative of a local re-activation. For the first time the step-wise invasion of effector T cells directed against a neuronal antigen into the CNS tissue was visualized via 2P-LSM. The first incoming T cells in the leptomeningeal vessels of SC and brain meninges were mainly rolling (approx. 80 %) resembling the motility behaviour of $T_{MBP\text{-}GFP}$ cells in the brain leptomeningeal vessels. After diapedesis in the SC meningeal compartment $T_{\beta Syn\text{-}GFP}$ cells showed the typical perivascular localization before spreading on top of the neuropil. On the brain meninges the same T cells immediately diffusely distributed

on the surface without showing a strict perivascular phase. With the on-going inflammation, $T_{\beta Syn\text{-}GFP}$ cells invaded in high numbers both of the meningeal compartments. Moreover, 2P-LSM imaging in the brain parenchyma showed that the $T_{\beta Syn\text{-}GFP}$ cells penetrated deep in the grey matter at the peak of the disease (fig. 3.24). Local re-activation of $T_{\beta Syn\text{-}GFP}$ cells in the brain GM might license these cells to penetrate deeper into the parenchyma. As discussed for T_{MBP} cells, more detailed investigation of the activation level of $T_{\beta Syn}$ cells *in situ* has to be performed by using the genetically encoded NFAT biosensor.

Even if it is reasonable to think that T cells of both specificities use the meninges as main entry port, the histological data suggest that the meninges might not be the sole way of entry. At the onset of the disease $T_{\beta Syn\text{-}GFP}$ cells were localized not only in the meningeal area but also deep in the GM of the SC mainly around parenchymal vessels (fig. 3.7). Similarly, at the peak of the disease $T_{MBP\text{-}GFP}$ cells were localized deep in the WM of the brain (fig. 3.8 E). In both cases the availability of the antigen seemed to determine the topology of T cell infiltration. This observation was particularly evident in the SC of $T_{\beta Syn\text{-}GFP}$ cell transferred animals. It is known that in rodents the DRG express a high level of β-synuclein whereas the perikarya of the SC motor neurons are largely devoid of this protein (Giasson et al., 2001). Accordingly, $T_{\beta Syn\text{-}GFP}$ cells were mainly localized in the posterior horns of the SC.
In order to investigate if the re-activation of the antigen specific T cells could also take place deep in the parenchyma, T_{MBP} and $T_{\beta Syn}$ cells, which express the regulatory subunit of the transcription factor NFAT together with YFP were used. NFAT activation is a very early event after TCR signalling; therefore translocation of NFAT from the cytosol to the nucleus allows monitoring in a spatial and temporal manner the process of activation. The results were clear: $T_{MBP\text{-}GFP}$ cells that underwent translocation were detectable in the WM of both SC and brain whereas successful translocation in $T_{\beta Syn\text{-}GFP}$ cells was detectable in the GM of the same compartments demonstrating a direct activation in the parenchyma.

4.3 Summary

In this work histological analysis, two-photon imaging and functional characterization were combined to investigate the mechanisms that regulate the entry of effector T cells into different CNS compartments i.e. brain and SC meninges, brain and SC parenchyma. For this purpose, EAE was induced by passive transfer of $T_{MBP\text{-}GFP}$ cells or $T_{\beta Syn\text{-}GFP}$ cells in Lewis rats. Irrespective of their differing antigen specificity, both types of effector T cells exhibited the same expression profile *in vitro* and a similar pathogenic potential *in vivo*. However, a radically different infiltration pattern between $T_{MBP\text{-}GFP}$ and $T_{\beta Syn\text{-}GFP}$ cells was demonstrated by histological analysis: whereas the $T_{MBP\text{-}GFP}$ cells predominantly infiltrated the SC, in particular the white matter region, the $T_{\beta Syn\text{-}GFP}$ cells were distributed exclusively in grey matter regions of both brain and SC. Chemokine expression or apoptosis rate in the different CNS compartments as assessed by quantitative real-time PCR and active Caspase-3 staining did not seem to play a role. Gene expression analysis of chemokine receptors or integrins on $T_{MBP\text{-}GFP}$ cells and $T_{\beta Syn\text{-}GFP}$ cells isolated from the periphery during the preclinical phase and from the different CNS compartments during the clinical phase excluded that these proteins played a role in determining the observed differential cell distribution. The chemokine expression data were confirmed by *ex vivo* transmigration studies.

In order to visualize the direct entry and distribution of the $T_{MBP\text{-}GFP}$ and $T_{\beta Syn\text{-}GFP}$ cells, life imaging by 2P-LSM was performed on the CNS meningeal compartments. As expected, $T_{MBP\text{-}GFP}$ cells invaded the meninges of the SC in high numbers whereas very few of them were visible in the brain meninges even at the peak of the disease. $T_{\beta Syn\text{-}GFP}$ cells at the onset of the disease invaded both the compartments in similar numbers. However, at the peak of the disease a massive infiltration of these cells was only detectable in the brain parenchyma, supporting the hypothesis that antigen-dependent activation of encephalitogenic T cells is the key factor that determines the distribution of these cells into the target tissue. Finally, by using a NFAT biosensor the *in situ* activation of T_{MBP} in the white matter and of $T_{\beta Syn}$ cells in the grey matter was demonstrated.

In my opinion the data have dual importance. From a scientific point of view it introduces a β-synuclein transfer EAE model that makes it possible to study grey matter inflammation, an important aspect of MS pathology. Secondly, the data could be of clinical relevance: it is now well accepted that at least some MS patients already have inflammatory lesions in their CNS grey matter in the early phase of the disease. Based on my data I suggest that an anti-neuronal adaptive immune response could be involved in the genesis of these lesions.

5. References

Abeliovich A, **Schmitz Y**, **Fariñas I**, **Choi-Lundberg D**, **Ho WH**, **Castillo PE**, **Shinsky N**, **Verdugo JM**, **Armanini M**, **Ryan A**, **Hynes M**, **Phillips H**, **Sulzer D**, **Rosenthal A**. Mice lacking alpha-synuclein display functional deficits in the nigrostriatal dopamine system. *Neuron* 25: 239–252, 2000.

Alstermark B, **Ogawa J**, **Isa T**. Lack of monosynaptic corticomotoneuronal EPSPs in rats: disynaptic EPSPs mediated via reticulospinal neurons and polysynaptic EPSPs via segmental interneurons. *J. Neurophysiol.* 91: 1832–1839, 2004.

Alt C, **Laschinger M**, **Engelhardt B**. Functional expression of the lymphoid chemokines CCL19 (ELC) and CCL 21 (SLC) at the blood-brain barrier suggests their involvement in G-protein-dependent lymphocyte recruitment into the central nervous system during experimental autoimmune encephalomyelitis. *Eur. J. Immunol.* 32: 2133–2144, 2002.

Arima Y, **Harada M**, **Kamimura D**, **Park J-H**, **Kawano F**, **Yull FE**, **Kawamoto T**, **Iwakura Y**, **Betz UAK**, **Márquez G**, **Blackwell TS**, **Ohira Y**, **Hirano T**, **Murakami M**. Regional neural activation defines a gateway for autoreactive T cells to cross the blood-brain barrier. *Cell* 148: 447–457, 2012.

Baranzini SE, **Wang J**, **Gibson RA**, **Galwey N**, **Naegelin Y**, **Barkhof F**, **Radue E-W**, **Lindberg RLP**, **Uitdehaag BMG**, **Johnson MR**, **Angelakopoulou A**, **Hall L**, **Richardson JC**, **Prinjha RK**, **Gass A**, **Geurts JJG**, **Kragt J**, **Sombekke M**, **Vrenken H**, **Qualley P**, **Lincoln RR**, **Gomez R**, **Caillier SJ**, **George MF**, **Mousavi H**, **Guerrero R**, **Okuda DT**, **Cree BAC**, **Green AJ**, **Waubant E**, **Goodin DS**, **Pelletier D**, **Matthews PM**, **Hauser SL**, **Kappos L**, **Polman CH**, **Oksenberg JR**. Genome-wide association analysis of susceptibility and clinical phenotype in multiple sclerosis. *Hum. Mol. Genet.* 18: 767–778, 2009.

Barnett MH, **Parratt JDE**, **Pollard JD**, **Prineas JW**. MS: is it one disease? *Int MS J* 16: 57–65, 2009.

Baron JL, **Madri JA**, **Ruddle NH**, **Hashim G**, **Janeway CA**. Surface expression of alpha 4 integrin by CD4 T cells is required for their entry into brain parenchyma. *J. Exp. Med.* 177: 57–68, 1993.

Bartholomäus I, **Kawakami N**, **Odoardi F**, **Schläger C**, **Miljkovic D**, **Ellwart JW**, **Klinkert WEF**, **Flügel-Koch C**, **Issekutz TB**, **Wekerle H**, **Flügel A**. Effector T cell interactions with meningeal vascular structures in nascent autoimmune CNS lesions. *Nature* 462: 94–98, 2009.

Bashir K, **Whitaker JN**. Clinical and laboratory features of primary progressive and secondary progressive MS. *Neurology* 53: 765–771, 1999.

Bauer J, **Bradl M**, **Hickley WF**, **Forss-Petter S**, **Breitschopf H**, **Linington C**, **Wekerle H**, **Lassmann H**. T-cell apoptosis in inflammatory brain lesions: destruction of T cells does not depend on antigen recognition. *Am. J. Pathol.* 153: 715–724, 1998.

Baxter AG. The origin and application of experimental autoimmune encephalomyelitis. *Nat. Rev. Immunol.* 7: 904–912, 2007.

Bechmann I, **Galea I**, **Perry VH**. What is the blood-brain barrier (not)? *Trends Immunol.* 28: 5–11, 2007.

Ben-Nun A, **Wekerle H**, **Cohen IR**. The rapid isolation of clonable antigen-specific T lymphocyte lines capable of mediating autoimmune encephalomyelitis. *Eur. J. Immunol.* 11: 195–199, 1981.

Berlin C, **Bargatze RF**, **Campbell JJ**, **Andrian von UH**, **Szabo MC**, **Hasslen SR**, **Nelson RD**, **Berg EL**, **Erlandsen SL**, **Butcher EC**. alpha 4 integrins mediate lymphocyte attachment and rolling under physiologic flow. *Cell* 80: 413–422, 1995.

Bielekova B, **Martin R**. Development of biomarkers in multiple sclerosis. *Brain* 127: 1463–1478, 2004.

Boggs JM. Myelin basic protein: a multifunctional protein. *Cell. Mol. Life Sci.* 63: 1945–1961, 2006.

Bozzali M, **Cercignani M**, **Sormani MP**, **Comi G**, **Filippi M**. Quantification of brain gray matter damage in different MS phenotypes by use of diffusion tensor MR imaging. *AJNR Am J Neuroradiol* 23: 985–988, 2002.

Bromley SK, **Mempel TR**, **Luster AD**. Orchestrating the orchestrators: chemokines in control of T cell traffic. *Nat. Immunol.* 9: 970–980, 2008.

Bø L, **Geurts JJG**, **van der Valk P**, **Polman C**, **Barkhof F**. Lack of correlation between cortical demyelination and white matter pathologic changes in multiple sclerosis. *Arch. Neurol.* 64: 76–80, 2007.

Bø L, **Vedeler CA**, **Nyland H**, **Trapp BD**, **Mørk SJ**. Intracortical multiple sclerosis lesions are not associated with increased lymphocyte infiltration. *Mult. Scler.* 9: 323–331, 2003a.

Bø L, **Vedeler CA**, **Nyland HI**, **Trapp BD**, **Mørk SJ**. Subpial demyelination in the cerebral cortex of multiple sclerosis patients. *J. Neuropathol. Exp. Neurol.* 62: 723–732, 2003b.

Calabrese M, **De Stefano N**, **Atzori M**, **Bernardi V**, **Mattisi I**, **Barachino L**, **Morra A**, **Rinaldi L**, **Romualdi C**, **Perini P**, **Battistin L**, **Gallo P**. Detection of cortical inflammatory lesions by double inversion recovery magnetic resonance imaging in patients with multiple sclerosis. *Arch. Neurol.* 64: 1416–1422, 2007.

Calabrese M, **Gallo P**. Magnetic resonance evidence of cortical onset of multiple sclerosis. *Mult. Scler.* 15: 933–941, 2009.

Call MJ. Small molecule modulators of MHC class II antigen presentation: mechanistic insights and implications for therapeutic application. *Mol. Immunol.* 48: 1735–1743, 2011.

Choi SR, **Howell OW**, **Carassiti D**, **Magliozzi R**, **Gveric D**, **Muraro PA**, **Nicholas R**, **Roncaroli F**, **Reynolds R**. Meningeal inflammation plays a role in the pathology of primary progressive multiple sclerosis. *Brain* 135: 2925–2937, 2012.

Cifelli A, **Arridge M**, **Jezzard P**, **Esiri MM**, **Palace J**, **Matthews PM**. Thalamic neurodegeneration in multiple sclerosis. *Ann. Neurol.* 52: 650–653, 2002.

Colley WC, **Sung TC**, **Roll R**, **Jenco J**, **Hammond SM**, **Altshuller Y**, **Bar-Sagi D**, **Morris AJ**, **Frohman MA**. Phospholipase D2, a distinct phospholipase D isoform with novel regulatory properties that provokes cytoskeletal reorganization. *Curr. Biol.* 7: 191–201, 1997.

Compston A, **Coles A**. Multiple sclerosis. *Lancet* 372: 1502–1517, 2008.

Cope AP. Studies of T-cell activation in chronic inflammation. *Arthritis Res.* 4 Suppl 3: S197–211, 2002.

Cross AH, **O'Mara T**, **Raine CS**. Chronologic localization of myelin-reactive cells in the lesions of relapsing EAE: implications for the study of multiple sclerosis. *Neurology* 43: 1028–1033, 1993.

Cruz-Orengo L, **Holman DW**, **Dorsey D**, **Zhou L**, **Zhang P**, **Wright M**, **McCandless EE**, **Patel JR**, **Luker GD**, **Littman DR**, **Russell JH**, **Klein RS**. CXCR7 influences leukocyte entry into the CNS parenchyma by controlling abluminal CXCL12 abundance during autoimmunity. *J. Exp. Med.* 208: 327–339, 2011.

Cua DJ, **Sherlock J**, **Chen Y**, **Murphy CA**, **Joyce B**, **Seymour B**, **Lucian L**, **To W**, **Kwan S**, **Churakova T**, **Zurawski S**, **Wiekowski M**, **Lira SA**, **Gorman D**, **Kastelein RA**, **Sedgwick JD**. Interleukin-23 rather than interleukin-12 is the critical cytokine for autoimmune inflammation of the brain. *Nature* 421: 744–748, 2003.

Denk W, **Strickler JH**, **Webb WW**. Two-photon laser scanning fluorescence microscopy. *Science* 248: 73–76, 1990.

Derfuss T, **Parikh K**, **Velhin S**, **Braun M**, **Mathey E**, **Krumbholz M**, **Kümpfel T**, **Moldenhauer A**, **Rader C**, **Sonderegger P**, **Pöllmann W**, **Tiefenthaller C**, **Bauer J**, **Lassmann H**, **Wekerle H**, **Karagogeos D**, **Hohlfeld R**, **Linington C**, **Meinl E**. Contactin-2/TAG-1-directed autoimmunity is identified in multiple sclerosis patients and mediates gray matter pathology in animals. *Proc. Natl. Acad. Sci. U.S.A.* 106: 8302–8307, 2009.

Dyment DA, **Yee IML**, **Ebers GC**, **Sadovnick AD**, **Canadian Collaborative Study Group**. Multiple sclerosis

in stepsiblings: recurrence risk and ascertainment. *J. Neurol. Neurosurg. Psychiatr.* 77: 258–259, 2006.

Emmanouilidou E, **Elenis D**, **Papasilekas T**, **Stranjalis G**, **Gerozissis K**, **Ioannou PC**, **Vekrellis K**. Assessment of α-synuclein secretion in mouse and human brain parenchyma. *PLoS ONE* 6: e22225, 2011.

Emmanouilidou E, **Melachroinou K**, **Roumeliotis T**, **Garbis SD**, **Ntzouni M**, **Margaritis LH**, **Stefanis L**, **Vekrellis K**. Cell-produced alpha-synuclein is secreted in a calcium-dependent manner by exosomes and impacts neuronal survival. *J. Neurosci.* 30: 6838–6851, 2010.

Engelhardt B, **Ransohoff RM**. The ins and outs of T-lymphocyte trafficking to the CNS: anatomical sites and molecular mechanisms. *Trends Immunol.* 26: 485–495, 2005.

Engelhardt B, **Ransohoff RM**. Capture, crawl, cross: the T cell code to breach the blood-brain barriers. *Trends Immunol.* 33: 579–589, 2012.

Engelhardt B, **Sorokin L**. The blood-brain and the blood-cerebrospinal fluid barriers: function and dysfunction. *Semin Immunopathol* 31: 497–511, 2009.

Eylar EH, **Kniskern PJ**, **Jackson JJ**. Myelin basic proteins. *Meth. Enzymol.* 32: 323–341, 1974.

Fisniku LK, **Chard DT**, **Jackson JS**, **Anderson VM**, **Altmann DR**, **Miszkiel KA**, **Thompson AJ**, **Miller DH**. Gray matter atrophy is related to long-term disability in multiple sclerosis. *Ann. Neurol.* 64: 247–254, 2008.

Flügel A, **Berkowicz T**, **Ritter T**, **Labeur M**, **Jenne DE**, **Li Z**, **Ellwart JW**, **Willem M**, **Lassmann H**, **Wekerle H**. Migratory activity and functional changes of green fluorescent effector cells before and during experimental autoimmune encephalomyelitis. *Immunity* 14: 547–560, 2001.

Flügel A, **Odoardi F**, **Nosov M**, **Kawakami N**. Autoaggressive effector T cells in the course of experimental autoimmune encephalomyelitis visualized in the light of two-photon microscopy. *J. Neuroimmunol.* 191: 86–97, 2007.

Flügel A, **Willem M**, **Berkowicz T**, **Wekerle H**. Gene transfer into CD4+ T lymphocytes: green fluorescent protein-engineered, encephalitogenic T cells illuminate brain autoimmune responses. *Nat. Med.* 5: 843–847, 1999.

Freund J, **McDermott K**. Sensitization to horse serum by means of adjuvants. *Proceedings of the Society for Experimental Biology and Medicine*. 49: 548-553, 1942.

Galvin JE, **Schuck TM**, **Lee VM**, **Trojanowski JQ**. Differential expression and distribution of alpha-, beta-, and gamma-synuclein in the developing human substantia nigra. *Exp. Neurol.* 168: 347–355, 2001.

Genain CP, **Nguyen MH**, **Letvin NL**, **Pearl R**, **Davis RL**, **Adelman M**, **Lees MB**, **Linington C**, **Hauser SL**. Antibody facilitation of multiple sclerosis-like lesions in a nonhuman primate. *J. Clin. Invest.* 96: 2966–2974, 1995.

George JM. The synucleins. *Genome Biol.* 3: REVIEWS3002, 2002.

Gerhardt H, **Betsholtz C**. Endothelial-pericyte interactions in angiogenesis. *Cell Tissue Res.* 314: 15–23, 2003.

Geurts JJG, **Bø L**, **Roosendaal SD**, **Hazes T**, **Daniëls R**, **Barkhof F**, **Witter MP**, **Huitinga I**, **van der Valk P**. Extensive hippocampal demyelination in multiple sclerosis. *J. Neuropathol. Exp. Neurol.* 66: 819–827, 2007.

Giasson BI, **Duda JE**, **Forman MS**, **Lee VM**, **Trojanowski JQ**. Prominent perikaryal expression of alpha- and beta-synuclein in neurons of dorsal root ganglion and in medullary neurons. *Exp. Neurol.* 172: 354–362, 2001.

Gilmore CP, **Donaldson I**, **Bø L**, **Owens T**, **Lowe J**, **Evangelou N**. Regional variations in the extent and pattern of grey matter demyelination in multiple sclerosis: a comparison between the cerebral cortex, cerebellar cortex, deep grey matter nuclei and the spinal cord. *J. Neurol. Neurosurg. Psychiatr.* 80: 182–187, 2009.

Gold R, **Linington C**, **Lassmann H**. Understanding pathogenesis and therapy of multiple sclerosis via animal models: 70 years of merits and culprits in experimental autoimmune encephalomyelitis research. *Brain* 129:

1953–1971, 2006.

Goverman J. Autoimmune T cell responses in the central nervous system. *Nat. Rev. Immunol.* 9: 393–407, 2009.

Grakoui A, **Bromley SK**, **Sumen C**, **Davis MM**, **Shaw AS**, **Allen PM**, **Dustin ML**. The immunological synapse: a molecular machine controlling T cell activation. *Science* 285: 221–227, 1999.

Groom JR, **Luster AD**. CXCR3 in T cell function. *Exp. Cell Res.* 317: 620–631, 2011.

Helm PJ, **Ottersen OP**, **Nase G**. Analysis of optical properties of the mouse cranium--implications for in vivo multi photon laser scanning microscopy. *J. Neurosci. Methods* 178: 316–322, 2009.

Helmchen F, **Denk W**. Deep tissue two-photon microscopy. *Nat. Methods* 2: 932–940, 2005.

Hemmer B, **Archelos JJ**, **Hartung H-P**. New concepts in the immunopathogenesis of multiple sclerosis. *Nat. Rev. Neurosci.* 3: 291–301, 2002.

Hemminki K, **Li X**, **Sundquist J**, **Hillert J**, **Sundquist K**. Risk for multiple sclerosis in relatives and spouses of patients diagnosed with autoimmune and related conditions. *Neurogenetics* 10: 5–11, 2009.

Hohlfeld R, **Wekerle H**. Autoimmune concepts of multiple sclerosis as a basis for selective immunotherapy: from pipe dreams to (therapeutic) pipelines. *Proc. Natl. Acad. Sci. U.S.A.* 101 Suppl 2: 14599–14606, 2004.

Holman DW, **Klein RS**, **Ransohoff RM**. The blood-brain barrier, chemokines and multiple sclerosis. *Biochim. Biophys. Acta* 1812: 220–230, 2011.

Huitinga I, **De Groot CJ**, **Van der Valk P**, **Kamphorst W**, **Tilders FJ**, **Swaab DF**. Hypothalamic lesions in multiple sclerosis. *J. Neuropathol. Exp. Neurol.* 60: 1208–1218, 2001.

Huizinga R, **Gerritsen W**, **Heijmans N**, **Amor S**. Axonal loss and gray matter pathology as a direct result of autoimmunity to neurofilaments. *Neurobiol. Dis.* 32: 461–470, 2008.

Huppa JB, **Davis MM**. T-cell-antigen recognition and the immunological synapse. *Nat. Rev. Immunol.* 3: 973–983, 2003.

International Multiple Sclerosis Genetics Consortium, **Hafler DA**, **Compston A**, **Sawcer S**, **Lander ES**, **Daly MJ**, **De Jager PL**, **de Bakker PIW**, **Gabriel SB**, **Mirel DB**, **Ivinson AJ**, **Pericak-Vance MA**, **Gregory SG**, **Rioux JD**, **McCauley JL**, **Haines JL**, **Barcellos LF**, **Cree B**, **Oksenberg JR**, **Hauser SL**. Risk alleles for multiple sclerosis identified by a genomewide study. *N. Engl. J. Med.* 357: 851–862, 2007.

International Multiple Sclerosis Genetics Consortium, **Wellcome Trust Case Control Consortium 2**, **Sawcer S**, **Hellenthal G**, **Pirinen M**, **Spencer CCA**, **Patsopoulos NA**, **Moutsianas L**, **Dilthey A**, **Su Z**, **Freeman C**, **Hunt SE**, **Edkins S**, **Gray E**, **Booth DR**, **Potter SC**, **Goris A**, **Band G**, **Oturai AB**, **Strange A**, **Saarela J**, **Bellenguez C**, **Fontaine B**, **Gillman M**, **Hemmer B**, **Gwilliam R**, **Zipp F**, **Jayakumar A**, **Martin R**, **Leslie S**, **Hawkins S**, **Giannoulatou E**, **D'alfonso S**, **Blackburn H**, **Martinelli Boneschi F**, **Liddle J**, **Harbo HF**, **Perez ML**, **Spurkland A**, **Waller MJ**, **Mycko MP**, **Ricketts M**, **Comabella M**, **Hammond N**, **Kockum I**, **McCann OT**, **Ban M**, **Whittaker P**, **Kemppinen A**, **Weston P**, **Hawkins C**, **Widaa S**, **Zajicek J**, **Dronov S**, **Robertson N**, **Bumpstead SJ**, **Barcellos LF**, **Ravindrarajah R**, **Abraham R**, **Alfredsson L**, **Ardlie K**, **Aubin C**, **Baker A**, **Baker K**, **Baranzini SE**, **Bergamaschi L**, **Bergamaschi R**, **Bernstein A**, **Berthele A**, **Boggild M**, **Bradfield JP**, **Brassat D**, **Broadley SA**, **Buck D**, **Butzkueven H**, **Capra R**, **Carroll WM**, **Cavalla P**, **Celius EG**, **Cepok S**, **Chiavacci R**, **Clerget-Darpoux F**, **Clysters K**, **Comi G**, **Cossburn M**, **Cournu-Rebeix I**, **Cox MB**, **Cozen W**, **Cree BAC**, **Cross AH**, **Cusi D**, **Daly MJ**, **Davis E**, **de Bakker PIW**, **Debouverie M**, **D'hooghe MB**, **Dixon K**, **Dobosi R**, **Dubois B**, **Ellinghaus D**, **Elovaara I**, **Esposito F**, **Fontenille C**, **Foote S**, **Franke A**, **Galimberti D**, **Ghezzi A**, **Glessner J**, **Gomez R**, **Gout O**, **Graham C**, **Grant SFA**, **Guerini FR**, **Hakonarson H**, **Hall P**, **Hamsten A**, **Hartung H-P**, **Heard RN**, **Heath S**, **Hobart J**, **Hoshi M**, **Infante-Duarte C**, **Ingram G**, **Ingram W**, **Islam T**, **Jagodic M**, **Kabesch M**, **Kermode AG**, **Kilpatrick TJ**, **Kim C**, **Klopp N**, **Koivisto K**, **Larsson M**, **Lathrop M**, **Lechner-Scott JS**, **Leone MA**, **Leppä V**, **Liljedahl U**, **Bomfim IL**, **Lincoln RR**, **Link J**, **Liu J**, **Lorentzen AR**, **Lupoli S**, **Macciardi F**, **Mack T**, **Marriott M**, **Martinelli V**, **Mason D**, **McCauley JL**, **Mentch F**, **Mero I-L**, **Mihalova T**, **Montalban X**, **Mottershead J**, **Myhr K-M**, **Naldi P**, **Ollier W**, **Page A**, **Palotie A**, **Pelletier J**, **Piccio L**, **Pickersgill T**, **Piehl**

F, **Pobywajlo S**, **Quach HL**, **Ramsay PP**, **Reunanen M**, **Reynolds R**, **Rioux JD**, **Rodegher M**, **Roesner S**, **Rubio JP**, **Rückert I-M**, **Salvetti M**, **Salvi E**, **Santaniello A**, **Schaefer CA**, **Schreiber S**, **Schulze C**, **Scott RJ**, **Sellebjerg F**, **Selmaj KW**, **Sexton D**, **Shen L**, **Simms-Acuna B**, **Skidmore S**, **Sleiman PMA**, **Smestad C**, **Sørensen PS**, **Søndergaard HB**, **Stankovich J**, **Strange RC**, **Sulonen A-M**, **Sundqvist E**, **Syvänen A-C**, **Taddeo F**, **Taylor B**, **Blackwell JM**, **Tienari P**, **Bramon E**, **Tourbah A**, **Brown MA**, **Tronczynska E**, **Casas JP**, **Tubridy N**, **Corvin A**, **Vickery J**, **Jankowski J**, **Villoslada P**, **Markus HS**, **Wang K**, **Mathew CG**, **Wason J**, **Palmer CNA**, **Wichmann H-E**, **Plomin R**, **Willoughby E**, **Rautanen A**, **Winkelmann J**, **Wittig M**, **Trembath RC**, **Yaouanq J**, **Viswanathan AC**, **Zhang H**, **Wood NW**, **Zuvich R**, **Deloukas P**, **Langford C**, **Duncanson A**, **Oksenberg JR**, **Pericak-Vance MA**, **Haines JL**, **Olsson T**, **Hillert J**, **Ivinson AJ**, **De Jager PL**, **Peltonen L**, **Stewart GJ**, **Hafler DA**, **Hauser SL**, **McVean G**, **Donnelly P**, **Compston A**. Genetic risk and a primary role for cell-mediated immune mechanisms in multiple sclerosis. *Nature* 476: 214–219, 2011.

Iwai A, **Masliah E**, **Yoshimoto M**, **Ge N**, **Flanagan L**, **de Silva HA**, **Kittel A**, **Saitoh T**. The precursor protein of non-A beta component of Alzheimer's disease amyloid is a presynaptic protein of the central nervous system. *Neuron* 14: 467–475, 1995.

Jakes R, **Spillantini MG**, **Goedert M**. Identification of two distinct synucleins from human brain. *FEBS Lett.* 345: 27–32, 1994.

Jenco JM, **Rawlingson A**, **Daniels B**, **Morris AJ**. Regulation of phospholipase D2: selective inhibition of mammalian phospholipase D isoenzymes by alpha- and beta-synucleins. *Biochemistry* 37: 4901–4909, 1998.

Kawakami N, **Lassmann S**, **Li Z**, **Odoardi F**, **Ritter T**, **Ziemssen T**, **Klinkert WEF**, **Ellwart JW**, **Bradl M**, **Krivacic K**, **Lassmann H**, **Ransohoff RM**, **Volk H-D**, **Wekerle H**, **Linington C**, **Flügel A**. The activation status of neuroantigen-specific T cells in the target organ determines the clinical outcome of autoimmune encephalomyelitis. *J. Exp. Med.* 199: 185–197, 2004.

Kawakami N, **Nägerl UV**, **Odoardi F**, **Bonhoeffer T**, **Wekerle H**, **Flügel A**. Live imaging of effector cell trafficking and autoantigen recognition within the unfolding autoimmune encephalomyelitis lesion. *J. Exp. Med.* 201: 1805–1814, 2005a.

Kawakami N, **Odoardi F**, **Ziemssen T**, **Bradl M**, **Ritter T**, **Neuhaus O**, **Lassmann H**, **Wekerle H**, **Flügel A**. Autoimmune CD4+ T cell memory: lifelong persistence of encephalitogenic T cell clones in healthy immune repertoires. *J. Immunol.* 175: 69–81, 2005b.

Kaye JF, **Kerlero de Rosbo N**, **Mendel I**, **Flechter S**, **Hoffman M**, **Yust I**, **Ben-Nun A**. The central nervous system-specific myelin oligodendrocytic basic protein (MOBP) is encephalitogenic and a potential target antigen in multiple sclerosis (MS). *J. Neuroimmunol.* 102: 189–198, 2000.

Kela-Madar N, **de Rosbo NK**, **Ronen A**, **Mor F**, **Ben-Nun A**. Autoimmune spread to myelin is associated with experimental autoimmune encephalomyelitis induced by a neuronal protein, beta-synuclein. *J. Neuroimmunol.* 208: 19–29, 2009.

Kidd D, **Barkhof F**, **McConnell R**, **Algra PR**, **Allen IV**, **Revesz T**. Cortical lesions in multiple sclerosis. *Brain* 122 (Pt 1): 17–26, 1999.

Kojima K, **Berger T**, **Lassmann H**, **Hinze-Selch D**, **Zhang Y**, **Gehrmann J**, **Reske K**, **Wekerle H**, **Linington C**. Experimental autoimmune panencephalitis and uveoretinitis transferred to the Lewis rat by T lymphocytes specific for the S100 beta molecule, a calcium binding protein of astroglia. *J. Exp. Med.* 180: 817–829, 1994.

Krumbholz M, **Theil D**, **Cepok S**, **Hemmer B**, **Kivisäkk P**, **Ransohoff RM**, **Hofbauer M**, **Farina C**, **Derfuss T**, **Hartle C**, **Newcombe J**, **Hohlfeld R**, **Meinl E**. Chemokines in multiple sclerosis: CXCL12 and CXCL13 up-regulation is differentially linked to CNS immune cell recruitment. *Brain* 129: 200–211, 2006.

Kutzelnigg A, **Lucchinetti CF**, **Stadelmann C**, **Brück W**, **Rauschka H**, **Bergmann M**, **Schmidbauer M**, **Parisi JE**, **Lassmann H**. Cortical demyelination and diffuse white matter injury in multiple sclerosis. *Brain* 128: 2705–2712, 2005.

Langrish CL, **Chen Y**, **Blumenschein WM**, **Mattson J**, **Basham B**, **Sedgwick JD**, **McClanahan T**, **Kastelein RA**, **Cua DJ**. IL-23 drives a pathogenic T cell population that induces autoimmune inflammation. *J. Exp. Med.* 201: 233–240, 2005.

Lassmann H, **Brück W**, **Lucchinetti C**. Heterogeneity of multiple sclerosis pathogenesis: implications for diagnosis and therapy. *Trends Mol Med* 7: 115–121, 2001.

Lavedan C. The synuclein family. *Genome Res.* 8: 871–880, 1998.

Lämmermann T, **Bader BL**, **Monkley SJ**, **Worbs T**, **Wedlich-Söldner R**, **Hirsch K**, **Keller M**, **Förster R**, **Critchley DR**, **Fässler R**, **Sixt M**. Rapid leukocyte migration by integrin-independent flowing and squeezing. *Nature* 453: 51–55, 2008.

Lees JR, **Golumbek PT**, **Sim J**, **Dorsey D**, **Russell JH**. Regional CNS responses to IFN-gamma determine lesion localization patterns during EAE pathogenesis. *J. Exp. Med.* 205: 2633–2642, 2008.

Leray E, **Yaouanq J**, **Le Page E**, **Coustans M**, **Laplaud D**, **Oger J**, **Edan G**. Evidence for a two-stage disability progression in multiple sclerosis. *Brain* 133: 1900–1913, 2010.

Ley K, **Laudanna C**, **Cybulsky MI**, **Nourshargh S**. Getting to the site of inflammation: the leukocyte adhesion cascade updated. *Nat. Rev. Immunol.* 7: 678–689, 2007.

Linington C, **Bradl M**, **Lassmann H**, **Brunner C**, **Vass K**. Augmentation of demyelination in rat acute allergic encephalomyelitis by circulating mouse monoclonal antibodies directed against a myelin/oligodendrocyte glycoprotein. *Am. J. Pathol.* 130: 443–454, 1988.

Linker RA, **Lee D-H**. Models of autoimmune demyelination in the central nervous system: on the way to translational medicine. *Exp Transl Stroke Med* 1: 5, 2009.

Lipton MM, **Freund J**. Encephalomyelitis in the rat following intracutaneous injection of central nervous system tissue with adjuvant. *Proc. Soc. Exp. Biol. Med.* 81: 260–261, 1952.

Lodygin D, Odoardi F, Schläger C, Körner H, van den Brandt J, Reichardt H, Kitz A, Nosov M, Haberl M, Flügel A. Real time imaging of NFAT dynamics reveals a crucial role of early T cell activation for the clinical fate in CNS autoimmunity. *Nat. Med.* In press.

Lucchinetti C, **Brück W**, **Parisi J**, **Scheithauer B**, **Rodriguez M**, **Lassmann H**. Heterogeneity of multiple sclerosis lesions: implications for the pathogenesis of demyelination. *Ann. Neurol.* 47: 707–717, 2000.

Lucchinetti CF, **Popescu BFG**, **Bunyan RF**, **Moll NM**, **Roemer SF**, **Lassmann H**, **Brück W**, **Parisi JE**, **Scheithauer BW**, **Giannini C**, **Weigand SD**, **Mandrekar J**, **Ransohoff RM**. Inflammatory cortical demyelination in early multiple sclerosis. *N. Engl. J. Med.* 365: 2188–2197, 2011.

Macian F. NFAT proteins: key regulators of T-cell development and function. *Nat. Rev. Immunol.* 5: 472–484, 2005.

Madsen LS, **Andersson EC**, **Jansson L**, **krogsgaard M**, **Andersen CB**, **Engberg J**, **Strominger JL**, **Svejgaard A**, **Hjorth JP**, **Holmdahl R**, **Wucherpfennig KW**, **Fugger L**. A humanized model for multiple sclerosis using HLA-DR2 and a human T-cell receptor. *Nat. Genet.* 23: 343–347, 1999.

Magliozzi R, **Howell O**, **Vora A**, **Serafini B**, **Nicholas R**, **Puopolo M**, **Reynolds R**, **Aloisi F**. Meningeal B-cell follicles in secondary progressive multiple sclerosis associate with early onset of disease and severe cortical pathology. *Brain* 130: 1089–1104, 2007.

Maroteaux L, **Campanelli JT**, **Scheller RH**. Synuclein: a neuron-specific protein localized to the nucleus and presynaptic nerve terminal. *J. Neurosci.* 8: 2804–2815, 1988.

Maroteaux L, **Scheller RH**. The rat brain synucleins; family of proteins transiently associated with neuronal membrane. *Brain Res. Mol. Brain Res.* 11: 335–343, 1991.

Martin R, **McFarland HF**, **McFarlin DE**. Immunological aspects of demyelinating diseases. *Annu. Rev. Immunol.* 10: 153–187, 1992.

McCandless EE, **Piccio L**, **Woerner BM**, **Schmidt RE**, **Rubin JB**, **Cross AH**, **Klein RS**. Pathological expression of CXCL12 at the blood-brain barrier correlates with severity of multiple sclerosis. *Am. J. Pathol.*

172: 799–808, 2008a.

McCandless EE, **Wang Q**, **Woerner BM**, **Harper JM**, **Klein RS**. CXCL12 limits inflammation by localizing mononuclear infiltrates to the perivascular space during experimental autoimmune encephalomyelitis. *J. Immunol.* 177: 8053–8064, 2006.

McCandless EE, **Zhang B**, **Diamond MS**, **Klein RS**. CXCR4 antagonism increases T cell trafficking in the central nervous system and improves survival from West Nile virus encephalitis. *Proc. Natl. Acad. Sci. U.S.A.* 105: 11270–11275, 2008b.

Meinl E, **Hoch RM**, **Dornmair K**, **de Waal Malefyt R**, **Bontrop RE**, **Jonker M**, **Lassmann H**, **Hohlfeld R**, **Wekerle H**, **'t Hart BA**. Encephalitogenic potential of myelin basic protein-specific T cells isolated from normal rhesus macaques. *Am. J. Pathol.* 150: 445–453, 1997.

Merkler D, **Böscke R**, **Schmelting B**, **Czéh B**, **Fuchs E**, **Brück W**, **Stadelmann C**. Differential macrophage/microglia activation in neocortical EAE lesions in the marmoset monkey. *Brain Pathol.* 16: 117–123, 2006a.

Merkler D, **Ernsting T**, **Kerschensteiner M**, **Brück W**, **Stadelmann C**. A new focal EAE model of cortical demyelination: multiple sclerosis-like lesions with rapid resolution of inflammation and extensive remyelination. *Brain* 129: 1972–1983, 2006b.

Miller DH, **Grossman RI**, **Reingold SC**, **McFarland HF**. The role of magnetic resonance techniques in understanding and managing multiple sclerosis. *Brain* 121 (Pt 1): 3–24, 1998.

Miller DH. Biomarkers and surrogate outcomes in neurodegenerative disease: lessons from multiple sclerosis. *NeuroRx* 1: 284–294, 2004.

Mor F, **Cohen IR**. How special is a pathogenic CNS autoantigen? Immunization to many CNS self-antigens does not induce autoimmune disease. *J. Neuroimmunol.* 174: 3–11, 2006.

Mor F, **Quintana F**, **Mimran A**, **Cohen IR**. Autoimmune encephalomyelitis and uveitis induced by T cell immunity to self beta-synuclein. *J. Immunol.* 170: 628–634, 2003.

Mouradian MM. Recent advances in the genetics and pathogenesis of Parkinson disease. *Neurology* 58: 179–185, 2002.

Murphy DD, **Rueter SM**, **Trojanowski JQ**, **Lee VM**. Synucleins are developmentally expressed, and alpha-synuclein regulates the size of the presynaptic vesicular pool in primary hippocampal neurons. *J. Neurosci.* 20: 3214–3220, 2000.

Nociti V, **Cianfoni A**, **Mirabella M**, **Caggiula M**, **Frisullo G**, **Patanella AK**, **Sancricca C**, **Angelucci F**, **Tonali PA**, **Batocchi AP**. Clinical characteristics, course and prognosis of spinal multiple sclerosis. *Spinal Cord* 43: 731–734, 2005.

O'Connor KC, **Bar-Or A**, **Hafler DA**. The neuroimmunology of multiple sclerosis: possible roles of T and B lymphocytes in immunopathogenesis. *J. Clin. Immunol.* 21: 81–92, 2001.

Odoardi F, **Kawakami N**, **Li Z**, **Cordiglieri C**, **Streyl K**, **Nosov M**, **Klinkert WEF**, **Ellwart JW**, **Bauer J**, **Lassmann H**, **Wekerle H**, **Flügel A**. Instant effect of soluble antigen on effector T cells in peripheral immune organs during immunotherapy of autoimmune encephalomyelitis. *Proc. Natl. Acad. Sci. U.S.A.* 104: 920–925, 2007.

Odoardi F, **Sie C**, **Streyl K**, **Ulaganathan VK**, **Schläger C**, **Lodygin D**, **Heckelsmiller K**, **Nietfeld W**, **Ellwart J**, **Klinkert WEF**, **Lottaz C**, **Nosov M**, **Brinkmann V**, **Spang R**, **Lehrach H**, **Vingron M**, **Wekerle H**, **Flügel-Koch C**, **Flügel A**. T cells become licensed in the lung to enter the central nervous system. *Nature* 488: 675–679, 2012.

Olitsky PK, **Yager RH**. Experimental disseminated encephalomyelitis in white mice. *J. Exp. Med.* 90: 213–224, 1949.

Ousman SS, **Kubes P**. Immune surveillance in the central nervous system. *Nat. Neurosci.* 15: 1096–1101, 2012.

Owens T, **Bechmann I**, **Engelhardt B**. Perivascular spaces and the two steps to neuroinflammation. *J. Neuropathol. Exp. Neurol.* 67: 1113–1121, 2008.

Owens T. Animal models for multiple sclerosis. *Adv Neurol* 98: 77–89, 2006.

Papadopoulos D, **Dukes S**, **Patel R**, **Nicholas R**, **Vora A**, **Reynolds R**. Substantial archaeocortical atrophy and neuronal loss in multiple sclerosis. *Brain Pathol.* 19: 238–253, 2009.

Pardridge WM. Blood-brain barrier drug targeting: the future of brain drug development. *Mol. Interv.* 3: 90–105– 51, 2003.

Paterson PY. Transfer of allergic encephalomyelitis in rats by means of lymph node cells. *J. Exp. Med.* 111: 119–136, 1960.

Paxinos G, **Watson C**. *The Rat Brain in Stereotaxic Coordinates*. Academic Press, 2007.

Pender MP, **Tabi Z**, **Nguyen KB**, **McCombe PA**. The proximal peripheral nervous system is a major site of demyelination in experimental autoimmune encephalomyelitis induced in the Lewis rat by a myelin basic protein-specific T cell clone. *Acta Neuropathol.* 89: 527–531, 1995.

Peterson JW, **Bø L**, **Mörk S**, **Chang A**, **Trapp BD**. Transected neurites, apoptotic neurons, and reduced inflammation in cortical multiple sclerosis lesions. *Ann. Neurol.* 50: 389–400, 2001.

Piddlesden SJ, **Lassmann H**, **Zimprich F**, **Morgan BP**, **Linington C**. The demyelinating potential of antibodies to myelin oligodendrocyte glycoprotein is related to their ability to fix complement. *Am. J. Pathol.* 143: 555–564, 1993.

Pierson E, **Simmons SB**, **Castelli L**, **Goverman JM**. Mechanisms regulating regional localization of inflammation during CNS autoimmunity. *Immunol. Rev.* 248: 205–215, 2012.

Pomeroy IM, **Matthews PM**, **Frank JA**, **Jordan EK**, **Esiri MM**. Demyelinated neocortical lesions in marmoset autoimmune encephalomyelitis mimic those in multiple sclerosis. *Brain* 128: 2713–2721, 2005.

Popescu BFG, **Bunyan RF**, **Parisi JE**, **Ransohoff RM**, **Lucchinetti CF**. A case of multiple sclerosis presenting with inflammatory cortical demyelination. *Neurology* 76: 1705–1710, 2011.

Popescu BFG, **Lucchinetti CF**. Meningeal and cortical grey matter pathology in multiple sclerosis. *BMC Neurol* 12: 11, 2012.

Pugliatti M, **Sotgiu S**, **Rosati G**. The worldwide prevalence of multiple sclerosis. *Clin Neurol Neurosurg* 104: 182–191, 2002.

Ransohoff RM, **Engelhardt B**. The anatomical and cellular basis of immune surveillance in the central nervous system. *Nat. Rev. Immunol.* 12: 623–635, 2012.

Ransohoff RM, **Kivisäkk P**, **Kidd G**. Three or more routes for leukocyte migration into the central nervous system. *Nat. Rev. Immunol.* 3: 569–581, 2003.

Reboldi A, **Coisne C**, **Baumjohann D**, **Benvenuto F**, **Bottinelli D**, **Lira S**, **Uccelli A**, **Lanzavecchia A**, **Engelhardt B**, **Sallusto F**. C-C chemokine receptor 6-regulated entry of TH-17 cells into the CNS through the choroid plexus is required for the initiation of EAE. *Nat. Immunol.* 10: 514–523, 2009.

Remlinger P. Les paralysies du traitement antirabique. *Annales de l'Institut Pasteur* 55: 35–68, 1928.

Rivers TM, **Schwentker FF**. Encephalomyelitis accompanied by myelin destruction experimentally produced in monkeys. *J. Exp. Med.* 61: 689–702, 1935.

Roach A, **Takahashi N**, **Pravtcheva D**, **Ruddle F**, **Hood L**. Chromosomal mapping of mouse myelin basic protein gene and structure and transcription of the partially deleted gene in shiverer mutant mice. *Cell* 42: 149–

155, 1985.

Rothhammer V, **Heink S**, **Petermann F**, **Srivastava R**, **Claussen MC**, **Hemmer B**, **Korn T**. Th17 lymphocytes traffic to the central nervous system independently of α4 integrin expression during EAE. *J. Exp. Med.* 208: 2465–2476, 2011.

Rovaris M, **Judica E**, **Gallo A**, **Benedetti B**, **Sormani MP**, **Caputo D**, **Ghezzi A**, **Montanari E**, **Bertolotto A**, **Mancardi G**, **Bergamaschi R**, **Martinelli V**, **Comi G**, **Filippi M**. Grey matter damage predicts the evolution of primary progressive multiple sclerosis at 5 years. *Brain* 129: 2628–2634, 2006.

Schwentker FF, **Rivers TM**. The antibody response of rabbits to injections of emulsions and extracts of homologues brain. *J. Exp. Med.* 60: 559–574, 1934.

Segal BM, **Shevach EM**. IL-12 unmasks latent autoimmune disease in resistant mice. *J. Exp. Med.* 184: 771–775, 1996.

Serafini B, **Rosicarelli B**, **Magliozzi R**, **Stigliano E**, **Aloisi F**. Detection of ectopic B-cell follicles with germinal centers in the meninges of patients with secondary progressive multiple sclerosis. *Brain Pathol.* 14: 164–174, 2004.

Sharpe AH, **Freeman GJ**. The B7-CD28 superfamily. *Nat. Rev. Immunol.* 2: 116–126, 2002.

Simon JH, **Kinkel RP**, **Jacobs L**, **Bub L**, **Simonian N**. A Wallerian degeneration pattern in patients at risk for MS. *Neurology* 54: 1155–1160, 2000.

Sporici R, **Issekutz TB**. CXCR3 blockade inhibits T-cell migration into the CNS during EAE and prevents development of adoptively transferred, but not actively induced, disease. *Eur. J. Immunol.* 40: 2751–2761, 2010.

Storch MK, **Bauer J**, **Linington C**, **Olsson T**, **Weissert R**, **Lassmann H**. Cortical demyelination can be modeled in specific rat models of autoimmune encephalomyelitis and is major histocompatibility complex (MHC) haplotype-related. *J. Neuropathol. Exp. Neurol.* 65: 1137–1142, 2006.

Stromnes IM, **Cerretti LM**, **Liggitt D**, **Harris RA**, **Goverman JM**. Differential regulation of central nervous system autoimmunity by T(H)1 and T(H)17 cells. *Nat. Med.* 14: 337–342, 2008.

Stumm RK, **Rummel J**, **Junker V**, **Culmsee C**, **Pfeiffer M**, **Krieglstein J**, **Höllt V**, **Schulz S**. A dual role for the SDF-1/CXCR4 chemokine receptor system in adult brain: isoform-selective regulation of SDF-1 expression modulates CXCR4-dependent neuronal plasticity and cerebral leukocyte recruitment after focal ischemia. *J. Neurosci.* 22: 5865–5878, 2002.

Thorpe JW, **Kidd D**, **Moseley IF**, **Thompson AJ**, **MacManus DG**, **Compston DA**, **McDonald WI**, **Miller DH**. Spinal MRI in patients with suspected multiple sclerosis and negative brain MRI. *Brain* 119 (Pt 3): 709–714, 1996.

Vajkoczy P, **Laschinger M**, **Engelhardt B**. Alpha4-integrin-VCAM-1 binding mediates G protein-independent capture of encephalitogenic T cell blasts to CNS white matter microvessels. *J. Clin. Invest.* 108: 557–565, 2001.

Wang H, **Wang K**, **Xu W**, **Wang C**, **Qiu W**, **Zhong X**, **Dai Y**, **Wu A**, **Hu X**. Cerebrospinal fluid α-synuclein levels are elevated in multiple sclerosis and neuromyelitis optica patients during replase. *J. Neurochem.* 122: 19–23, 2012.

Wegner C, **Esiri MM**, **Chance SA**, **Palace J**, **Matthews PM**. Neocortical neuronal, synaptic, and glial loss in multiple sclerosis. *Neurology* 67: 960–967, 2006.

Wekerle H. Lessons from multiple sclerosis: models, concepts, observations. *Ann. Rheum. Dis.* 67 Suppl 3: iii56–60, 2008.

Wensky AK, **Furtado GC**, **Marcondes MCG**, **Chen S**, **Manfra D**, **Lira SA**, **Zagzag D**, **Lafaille JJ**. IFN-gamma determines distinct clinical outcomes in autoimmune encephalomyelitis. *J. Immunol.* 174: 1416–1423, 2005.

Withers GS, **George JM**, **Banker GA**, **Clayton DF**. Delayed localization of synelfin (synuclein, NACP) to presynaptic terminals in cultured rat hippocampal neurons. *Brain Res. Dev. Brain Res.* 99: 87–94, 1997.

Xu H-T, **Pan F**, **Yang G**, **Gan W-B**. Choice of cranial window type for in vivo imaging affects dendritic spine turnover in the cortex. *Nat. Neurosci.* 10: 549–551, 2007.

Zepp J, **Wu L**, **Li X**. IL-17 receptor signaling and T helper 17-mediated autoimmune demyelinating disease. *Trends Immunol.* 32: 232–239, 2011.

6. Acknowledgments

First of all, I would like to thank Prof. Dr. Alexander Flügel for giving me the opportunity to write my PhD thesis in the Institute for Multiple Sclerosis Research (IMSF) under his direction as well as his great support and advice. My utmost gratitude goes to my supervisor Dr. Francesca Odoardi for her commitment and encouragement as well as her constant support during my work.

I want to thank the members of my thesis committee Prof. Dr. Wolfgang Brück, Dr. Till Marquardt and Prof. Dr. Fred Wouters for their support and discussion of my thesis project. Moreover, I would like to thank Prof. Dr. Hannelore Ehrenreich and Prof. Dr. Mika Simons for agreeing to be part of my examination board.

Special thanks to Christian Schläger for his outstanding support and advice during this project, especially for his help with the two-photon microscope and the corresponding data analysis.

I am grateful to Dr. Dimitry Lodygin for the productive and pleasant collaboration, for the NFAT sensor that he kindly provided as well as his help and support. Furthermore, I would like to thank Dr. Fred Lühder for his help and general support. In addition, I would like to express my gratitude to Prof. Dr. Christine Stadelmann-Nessler for sharing her knowledge of β-synuclein and the on-going pleasant collaboration.

I want to thank Adriane Stas, Simone Hamann, Nancy Meyer and Simon Mole for their help and technical advice and Cathy Ludwig for her organisational help and constant support.

Many thanks to Alexandra Kitz, Anne Flach, Michael Haberl, Claudia Fokken, Manuel von Osten, Tanja Litke, Christopher Sie, and all the others that supported me with academic and technical advice as well as encouragement and companionship during my PhD project.

I am very grateful to all the people in the IMSF for welcoming me in their midst and the great working as well as interpersonal atmosphere.

Finally, I want to thank my whole family, especially my father and my mother, my brother, Gabi, Marlene, Bernd, Ömi, my godmother Erna and my close friends Valeska Fella, Antje Volkmar and Pia Glorius for their caring support and for being patient with me.

I want to express my gratitude to Jan Winchenbach for his support and advice that helped me to endure the stressful times of this project.

Declaration

Herewith I declare that I prepared the doctoral thesis "Live imaging of autoimmune responses in distinct milieus of the central nervous system" on my own and with no other sources and aids than quoted.

Corinna Schlosser

Göttingen, 22.04.2013